

Stellingen

behorende bij het proefschrift

Compact Integrated Optical Components
for Telecommunication Networks

door

L. H. Spiekman

24 september 1996.

1. Verdere verkleining van bochtstralen in diep-geëtste golfgeleiderbochten zoals beschreven in dit proefschrift wordt meer beperkt door de verandering van het modeprofiel in de bocht dan door afstralingsverliezen. Verder onderzoek naar bochten zonder abrupte overgangen aan de uiteinden verdient daarom aanbeveling.

2. Voor de grootte van 'Phased Array' golflengtedemultiplexers vormt de te gebruiken minimum bochtstraal niet de belangrijkste beperking.

3. De Fabry-Pérot meetmethode voor golfgeleiderverliezen is onnauwkeurig bij zowel zeer hoge als zeer lage golfgeleiderverliezen. Het is daarom aan de huidige stand van de fabricagetechnologie te danken dat zij bruikbaar is voor het meten van de verliezen van golfgeleiders in III/V halfgeleidermateriaal.

4. Het verstrooiingsverlies in dijk golfgeleiders met zwakke optische opsluiting wordt meer bepaald door verstrooiing aan de geëtste oppervlakken naast de dijk dan door verstrooiing aan de dijkwanden.

5. De bewering van Hewson-Browne *et al.* dat het verstrooiingsverlies aan een golfgeleiderwand evenredig is met het kwadraat van de integraal van het E-veld over de wand is niet correct. (R. C. Hewson-Browne *et al.*, *IEE Proc.*, Pt. J, vol. 136, pp. 281-286, Oct. 1989.)

6. Schrödinger's kat is dood.

7. De manier waarop de Amerikaanse telecommunicatiemarkt is ingericht (monopolies voor de lokale telefoonmaatschappijen, concurrentie tussen de 'long distance' operators), biedt geen bewijs voor de stelling dat concurrentie tot lagere prijzen leidt.

8. Het auteursrecht in zijn huidige vorm is te restrictief voor de vormen van informatie-uitwisseling die op netwerken als Internet in opkomst zijn. 'Fair use' zou voorrang moeten krijgen boven formele verveelvuldigings- en openbaarmakingscriteria als leidend stelsel voor dit rechtsgebied.

9. Stellingen over stellingen zouden alleen toegelaten moeten worden in proefschriften over magazijnarchitectuur.

10. De onder taalkundigen vaak gehoorde mening dat wat correct taalgebruik is door de sprekers en schrijvers der taal zelf bepaald wordt, moet niet als leidraad voor correct taalgebruik gehanteerd gaan worden.

11. Wanneer meer mensen zich zouden verdiepen in de speltheorie, zou dit wonderen kunnen doen voor de belastingmoraal.

12. Natuurkundigen die hun wetten normatief, en juristen die hun wetten beschrijvend opvatten, lopen het gevaar zich schuldig te maken aan het bezigen van drogredenen.

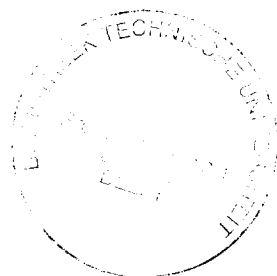
Compact Integrated Optical Components
for Telecommunication Networks

PROEFSCHRIFT

TER VERKRIJGING VAN DE GRAAD VAN DOCTOR
AAN DE TECHNISCHE UNIVERSITEIT DELFT,
OP GEZAG VAN DE RECTOR MAGNIFICUS PROF. IR K. F. WAKKER,
IN HET OPENBAAR TE VERDEDIGEN TEN OVERSTAAN VAN EEN COMMISSIE,
DOOR HET COLLEGE VAN DEKANEN AANGEWEEZEN,
OP DINSDAG 24 SEPTEMBER 1996 TE 16:00 UUR
DOOR

Leonard Henri SPIEKMAN

Doctorandus in de Natuurkunde,
geboren te Utrecht.



Dit proefschrift is goedgekeurd door de promotor:
Prof. dr B. H. Verbeek

Samenstelling promotiecommissie:

Rector Magnificus, voorzitter

Prof. dr B. H. Verbeek, Technische Universiteit Delft, promotor

Dr ir M. K. Smit, Technische Universiteit Delft, toegevoegd promotor

Prof. dr ir R. G. F. Baets, Universiteit Gent

Prof. dr ir H. Blok, Technische Universiteit Delft

Prof. dr ir W. van Etten, Universiteit Twente

Prof. dr ir G. D. Khoe, Technische Universiteit Eindhoven

Prof. dr ir H. J. Frankena, Technische Universiteit Delft

This work was supported by the Dutch Ministry of Economic Affairs (IOP Electro-Optics).

The work described in chapter 6 has been performed in close cooperation with Akzo Nobel Central Research, Arnhem, The Netherlands.

The work described in chapters 7 and 8 has been performed in close cooperation with Philips Optoelectronics Centre, Eindhoven, The Netherlands.

Spiekman, Leonard Henri

Compact Integrated Optical Components for Telecommunication Networks /

Leonard Henri Spiekman. - [S.l. : s.n.] - Ill. -

Ph.D. Thesis Delft University of Technology. - With ref. - With summary in Dutch.

ISBN 90-9009718-X

NUGI 841

Keywords: Integrated optics / Optoelectronics.

Copyright ©1996 Leo Spiekman

Typeset by L^AT_EX 2_ε; printed by Ridderprint, Ridderkerk, The Netherlands

Voor Harry van Lith
(1900–1977)

Contents

1	General introduction	1
1.1	Telecommunication	1
1.2	Optical communication	2
1.3	Integrated optics	3
1.4	About this thesis	4
2	Theory and experimental methods	5
2.1	Introduction	5
2.2	The electromagnetic field	5
2.3	Waveguiding	6
2.3.1	Two-dimensional waveguides	7
2.3.2	Three-dimensional waveguides	8
2.3.3	Curved waveguides	9
2.3.4	End-to-end coupling of two waveguides	10
2.4	Device fabrication	11
2.4.1	Properties of InGaAsP	11
2.4.2	Waveguide processing	12
2.5	Measurement techniques	13
3	Waveguide loss	15
3.1	Introduction	15
3.1.1	Absorption	16
3.1.2	Scattering	16
3.1.3	Leakage	21
3.2	Scattering loss in straight waveguides	22
3.2.1	Calculation of field intensity at an interface	23
3.2.2	Fabrication of low loss waveguides	27
3.2.3	Experimental results	28
3.3	Waveguide bends	33
3.3.1	Corner mirrors	34
3.3.2	Curved waveguides	35

3.3.3	High contrast curved waveguides	36
3.3.4	Experimental results	38
3.4	Conclusion	43
3.A	Derivation of reflection formula	43
3.B	<i>E</i> -dependence of scattering loss	45
4	Miniaturisation of MMI couplers	47
4.1	Introduction	47
4.2	Multi-mode interference and self-imaging	49
4.2.1	Modal propagation analysis	49
4.2.2	Image formation	51
4.2.3	Performance of MMI couplers	52
4.3	Experimental results	53
4.3.1	Miniaturised MMI couplers	54
4.3.2	Tolerance analysis	59
4.4	Discussion	63
4.5	Conclusion	66
4.A	The Dirac notation	67
5	Wavelength demultiplexing on InP	69
5.1	Introduction	69
5.2	Phased array operating principle	70
5.2.1	TE-TM shift	72
5.2.2	Polarisation Independent Design	73
5.3	Fabrication Tolerance Analysis	74
5.4	Experimental results	76
5.4.1	Fabrication	78
5.4.2	Transmission experiments	78
5.5	Conclusion	80
6	Polymeric wavelength demultiplexers	81
6.1	Introduction	81
6.2	Waveguide structure	82
6.2.1	Radiation loss in curved waveguides	84
6.2.2	Coupling between waveguides	85
6.2.3	High contrast waveguide structures	85
6.2.4	Fabrication variations	87
6.3	Phased array design	88
6.3.1	Channel spacing and wavelength response	89
6.3.2	Insertion loss	90
6.3.3	Free propagation sections	91
6.3.4	Waveguide array	92
6.3.5	Crosstalk in the array	94

6.3.6	Input/output waveguide configuration	94
6.3.7	Summary of device parameters	95
6.4	Experimental results	97
6.4.1	Demultiplexers	97
6.4.2	Polarisation dependence	100
6.5	Conclusions	100
7	Switching by exploiting the wavelength domain	101
7.1	Introduction	101
7.2	Experimental	101
7.3	Discussion	106
8	A multi-wavelength laser	107
8.1	Introduction	107
8.2	Design and fabrication	107
8.3	Experimental results	109
8.4	Discussion	111
	References	115
	Summary	123
	Samenvatting	125
	Dankwoord	127
	Curriculum Vitae	129

Cover: James Clerk Maxwell (1831–1879)

Chapter 1

General introduction

1.1 Telecommunication

There are not many things that are as important to man as communication. We communicate all day, while engaged in all sorts of activities, only to stop when we go to sleep. (And even then, some talk in their sleep!)

Communicating is so important to us, that we have developed all kinds of techniques and devices to help us, such as the printing press for disseminating written messages, photography for reproducing pictures, and the phonograph and tape recorder for storing and retrieving sounds. Add to this film and video, and we have the means of conveying messages to others in almost any form we wish.

But our need to socialise is so strong, that we even want to communicate with people who are not in our immediate vicinity. People want to talk to family and friends away from home, companies want to do business with partners far away, and we generally like being amused by stories that reach us from elsewhere. In old times, the only way of doing all these things would be by exchanging letters. The desire to communicate-at-a-distance more quickly led to the development of semaphore systems and later the electrical telegraph (Morse), the first telecommunication systems. They were followed quickly by the telephone (Bell), radio telegraphy (Marconi), radio and television broadcasting, Telex, mobile telephony and data transmission. We now have a worldwide telephone network that allows us to speak to any other telephone subscriber anywhere in the world, anytime, and that can also be used to transmit written information by means of facsimile, and to transmit data with computer modems. More and more people and institutions are connected to the world-wide computer network Internet, over which they send each other email, communicate via bulletin boards called 'newsgroups', work on each other's computers, and exchange data more easily than handing over floppy disks. And almost everyone nowadays possesses a radio and a TV-set, with which one can receive numerous channels, either broadcast or from the cable network.

With this increasing demand for communication comes an ever growing need for communication bandwidth. People want to be able to receive more and more radio and TV channels

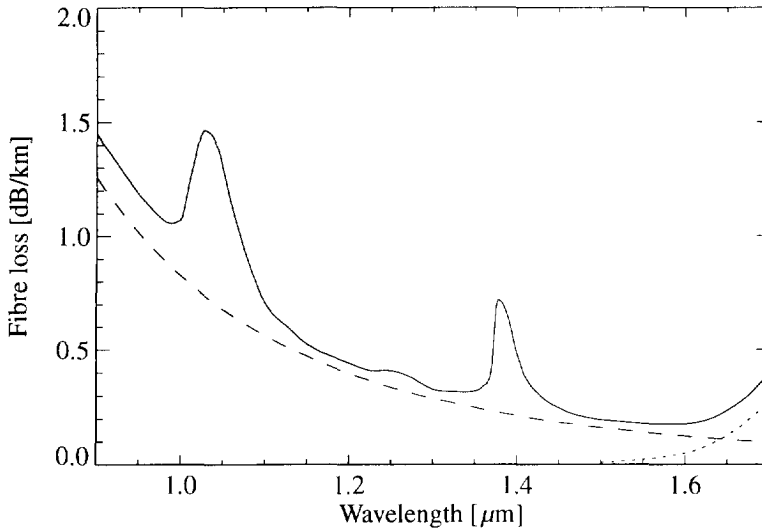


Figure 1.1: Measured loss as a function of wavelength for a high quality fused-silica single mode optical fibre. The dashed line shows the Rayleigh scattering loss, and the dotted line shows the contribution of vibrational absorption.

from their cable network, cable companies think they can make profits with video on demand services, and the Internet is flooded with more and more video and multi-media applications, such as CUSeeMe and WWW. There is a clear and growing need for wider telecommunication channels, which are not in abundant supply with present electrical connections.

1.2 Optical communication

The problem of bandwidth may be solved by turning to optical techniques. When Maiman [1] demonstrated the first laser in 1960, Hayashi and Panish [2] did the same a few years later with the first semiconductor heterostructure laser, and Kao and Hockham [3] proposed using optical fibres as a waveguide, it was realized that frequencies of the order of 200 THz, in combination with the coherence properties of laser light, would result in an enormous bandwidth that could be used for telecommunication purposes. At the time, fibre attenuation of 20 dB/km could be achieved [4]. Since then, technological improvements have steadily reduced fibre loss to a present value of 0.2 dB/km at a wavelength of 1.55 μm (see figure 1.1), close to the theoretical limit. Furthermore, for standard fibre, zero dispersion occurs around 1.3 μm . Therefore, these two wavelength regions or ‘windows’ have become extremely important for optical telecommunication. Optical signals of these wavelengths can be generated by semiconductor lasers made in the InGaAsP semiconductor system, which has attracted much attention for this reason.

The simplest telecommunication system that can be built with lasers, detectors, and op-

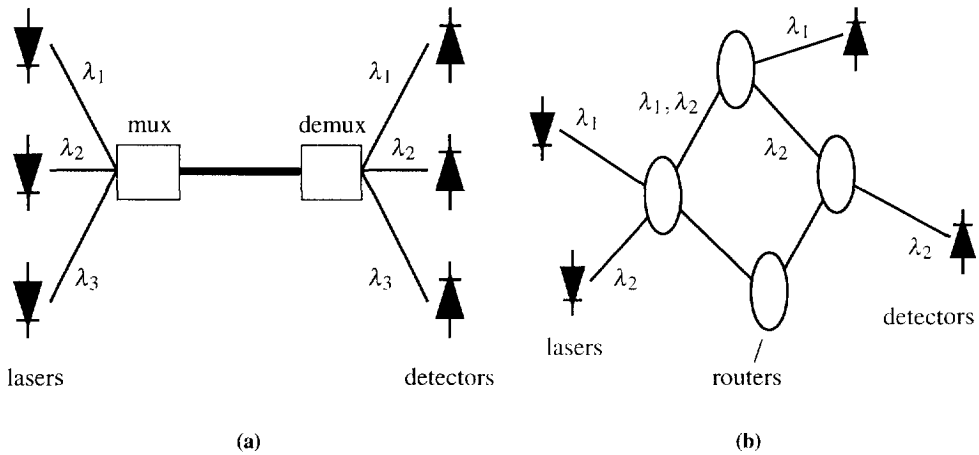


Figure 1.2: Wavelength Division Multiplexing (WDM) increases channel capacity (a) and adds flexibility in networks with passive routers (b), where the transmitter can determine the route taken through the network by choosing what wavelength to transmit on.

tical fibres, is a simple point-to-point link. Thanks to fibre amplifiers (EDFAs) and dispersion compensating techniques, large distances can be spanned; 20Gb/s over 8100km has been demonstrated [5].

Many signals can be transported over the same fibre by using time division multiplexing (TDM). The transmission capacity can be increased even further by exploiting the wavelength domain: multiple signal channels can be transmitted on a single fibre by using wavelength division multiplexing (WDM), as shown in figure 1.2(a). Theoretically, both windows at 1.3 and 1.55 μm can be completely filled up, giving 10 to 20THz of bandwidth. At the moment of writing, the 1THz barrier has been broken, with transmission of 55 channels of 20Gb/s each [6]. In addition, WDM can significantly enhance network flexibility by using wavelength for functions such as routing and switching [7]. As the example in figure 1.2(b) shows, in a network consisting of nodes containing passive wavelength routers, the transmitter could determine the route taken through the network by its wavelength.

1.3 Integrated optics

The electronic Integrated Circuit (IC) is the main reason that electronic equipment is available for very low prices these days. Lithographic definition of large quantities of components in only a few fabrication steps, with the added benefit of stable connections between them, has made low cost mass production possible. Integrated optics (a term coined by Miller [8] in 1969), is intended to do the same for optical devices, because the same advantages could also

apply to photonic ICs (PICs) [9]. Lithographic definition will lead to rigid interconnections between components, and allows mass production of devices that would otherwise have to be machined individually and aligned by hand. Thus, integrated optics can reduce the number of expensive couplings necessary between components and fibres. Especially for optical circuits with a high degree of functionality, which require a large number of components, the integrated optical approach will provide an advantage in cost and performance over hybrid or micro-optical solutions [10].

1.4 About this thesis

Multiplexers and power couplers are elementary components in WDM systems. Because integration of complicated devices with large functionality requires compact components, miniaturisation of these components is an important issue. This thesis deals with miniaturisation of planar multiplexers and couplers suitable for further opto-electronic integration. Besides reduction of the size, another leading theme is the effect this has on fabrication tolerances.

Chapter 2 provides some theoretical background on the subject of waveguiding as well as a brief overview of waveguide fabrication technology and used measurement techniques.

Because waveguiding is of cardinal importance for PICs, chapter 3 deals with the fabrication of low loss waveguides and waveguide bends in the InGaAsP/InP material system, in which most of the components in this thesis are made.

Chapter 4 deals with optical power splitting and combining with multi-mode interference (MMI) couplers, with the emphasis on the effects of miniaturisation on fabrication tolerance.

The birefringence of waveguides in the InGaAsP/InP material system sometimes forms a problem when polarisation-independent devices are desired. In chapter 5, a method for making polarisation-independent wavelength demultiplexers of the 'phased array' type is described.

Other material systems, such as polymers, enable fabrication of square waveguides, so that birefringence is less of a problem. In addition, polymers allow waveguides to be made that couple much more easily to fibres, due to their low index contrast. Chapter 6 presents phased array demultiplexers made in this material system. Here, the main problem is their size, because a low index contrast does not allow very tight waveguide bends.

Chapters 7 and 8 present applications of the phased array multiplexer in more complicated devices. In chapter 7, an experiment is described in which a multiplexer is coupled to wavelength converters to make a switch, and in chapter 8 a multi-wavelength laser is described, built from a multiplexer integrated with gain sections.

Chapter 2

Theory and experimental methods

2.1 Introduction

All integrated optical devices described in this thesis are based on (usually single mode) optical waveguides. In this chapter, the non-expert reader will be provided with some theoretical background on the subject of waveguiding, and a brief overview of waveguide fabrication technology and used measurement techniques will be given. More detailed accounts of waveguiding theory and technology have been given by Tamir (ed.) [11] and Hunsperger [12].

Propagation of light through a waveguide is an electromagnetic phenomenon, and as such can be described by Maxwell's equations. These will be reviewed in section 2.2. Waveguiding and the concept of modes will be briefly dealt with in section 2.3. Most devices in this thesis have been fabricated in InGaAsP/InP. The most important properties of this material system, as well as the waveguide fabrication method, are outlined in section 2.4. Finally, the methods used to measure most of the devices presented in this thesis are described in section 2.5.

2.2 The electromagnetic field

In 1865, James Clerk Maxwell published his famous paper "A Dynamical Theory of the Electromagnetic Field" [13], in which he laid down the equations which, in modified form, are still known as "Maxwell's equations". Maxwell did not use vector notation, and his equations number a total of twenty. Today, in vector notation, Maxwell's equations are denoted [14]:

$$\nabla \cdot \mathbf{D} = \rho \quad (2.1)$$

$$\nabla \times \mathbf{E} = -\frac{\partial \mathbf{B}}{\partial t} \quad (2.2)$$

$$\nabla \cdot \mathbf{B} = 0 \quad (2.3)$$

$$\nabla \times \mathbf{H} = \frac{\partial \mathbf{D}}{\partial t} + \mathbf{j}. \quad (2.4)$$

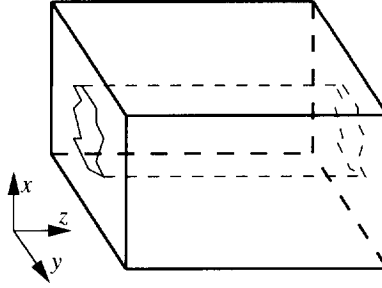


Figure 2.1: Straight waveguide consisting of material with a z -invariant refractive index distribution. In this structure, modes can propagate in the z direction.

Besides these, Maxwell's original equations also include Ohm's law, the equation of conservation of charge, and the relations $\mathbf{E} = \epsilon \mathbf{D}$ and $\mathbf{B} = \mu \mathbf{H}$.

For most optical materials (such as dielectrics and semiconductors), μ is a constant equal to the permeability of vacuum $\mu_0 \equiv 4\pi \cdot 10^{-7} \text{ N} \cdot \text{A}^{-2}$, so (2.3) implies $\nabla \cdot \mathbf{H} = 0$. Likewise, when a source-free ($\rho = 0$), homogeneous ($\nabla \epsilon = 0$) medium is assumed, (2.1) implies $\nabla \cdot \mathbf{E} = 0$. In the absence of currents, (2.2) and (2.4) can be combined to form

$$\nabla^2 \mathbf{E} + \epsilon \mu_0 \frac{\partial^2 \mathbf{E}}{\partial t^2} = 0 \quad (2.5)$$

and an identical equation for \mathbf{H} . By substitution, it is seen that the plane waves

$$\mathbf{E}(\mathbf{r}, t) = \mathbf{E}_0 e^{i(\omega t - \mathbf{k} \cdot \mathbf{r})} \quad \mathbf{H}(\mathbf{r}, t) = \mathbf{H}_0 e^{i(\omega t - \mathbf{k} \cdot \mathbf{r})} \quad (2.6)$$

are solutions to the wave equations (2.5) when $|\mathbf{k}|/\omega = \sqrt{\epsilon \mu_0} = n/c$, with $n = \sqrt{\epsilon/\epsilon_0}$ the refractive index of the medium; ϵ_0 is the permittivity of the vacuum. A lossy (e.g., absorbing) medium is described with a complex refractive index. \mathbf{E} and \mathbf{H} are perpendicular to each other and to \mathbf{k} . The wavelength of the plane waves described by (2.6) is $\lambda = 2\pi/k$ ($= \lambda_0/n$, $\lambda_0 = 2\pi/k_0$ the wavelength in vacuum).

In non-homogeneous media consisting of regions with piecewise constant $n(\mathbf{r})$, the plane wave solutions (2.6) can still be used within each of the regions. At the discontinuities, the solutions can be matched by demanding the continuity of \mathbf{H} , \mathbf{E}_{\parallel} (the part of \mathbf{E} parallel to the boundary), and $\epsilon \mathbf{E}_{\perp}$ (the part of $\epsilon \mathbf{E}$ perpendicular to the boundary).

2.3 Waveguiding

In a z -invariant structure, i.e., one with a refractive index distribution $n = n(x, y)$ (see figure 2.1), solutions of the wave equation can be found of the form

$$\mathbf{E}(\mathbf{r}) = \mathbf{E}_m(x, y) e^{-i\beta_m z} \quad \mathbf{H}(\mathbf{r}) = \mathbf{H}_m(x, y) e^{-i\beta_m z} \quad (2.7)$$

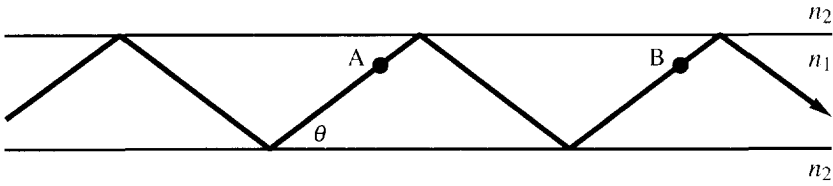


Figure 2.2: Two-dimensional structure comprising a stack of layers with different refractive indices n_1, n_2 . When $n_2 < n_1$, light can be confined to the central, or *guiding* layer because of total internal reflection. It is reflected back and forth between the two interfaces.

(the harmonic time dependence $e^{i\omega t}$ is assumed implicit from now on). These equations describe a two-dimensional field distribution in the x, y -plane, propagating in the z (or longitudinal) direction unmodified, with a longitudinal wavenumber β_m . Such a field is called a *mode*. The field distribution is called the *mode profile*, and the wavenumber β_m is called the *propagation constant* of the mode. The subscript m is used to distinguish different solutions. An “effective refractive index” can be associated with the structure for each mode m , by writing $\beta_m = n_{\text{eff},m}k_0$

2.3.1 Two-dimensional waveguides

The occurrence of discrete modes can be understood by studying a simplified waveguiding problem. Consider the two-dimensional structure given in figure 2.2. A ray of light in the central layer (with refractive index n_1), incident on the interface with one of the outer layers (having refractive index n_2), will be partially reflected. If $n_2 < n_1$ and the angle of incidence θ is smaller than the critical angle for total internal reflection given by

$$\theta_c = \arccos \frac{n_2}{n_1}, \quad (2.8)$$

the reflection coefficient will be 1, and the light will be confined to the central layer, bouncing back and forth between the two interfaces. A ray of light confined in such a structure will only interfere constructively with itself when the total phase change in one round trip, e.g., from A to B in figure 2.2, is an integer multiple of 2π . Under this condition the light distribution is self-maintaining.

The actual light distribution of a mode can be found by viewing it as a superposition of an upward and a downward travelling plane wave:

$$\mathbf{E}(x, z) = \mathbf{E}_0(c_u e^{-ik_x x} + c_d e^{+ik_x x})e^{-i\beta z}, \quad (2.9)$$

where $k_x^2 + \beta^2 = k_x^2 + k_z^2 = k^2 = (n_1 k_0)^2$. The coefficients c_u and c_d are equal for a symmetric structure. Because $e^{-ik_x x} + e^{+ik_x x} = 2\cos k_x x$, the field in the central (guiding) layer has a cosine-like shape. In the outer (cladding) layers, we must have $k_x^2 + \beta^2 = (n_2 k_0)^2$, and from (2.8) and the condition that the propagation angle $\theta = \arccos(\beta/n_1 k_0) < \theta_c$, it follows that in

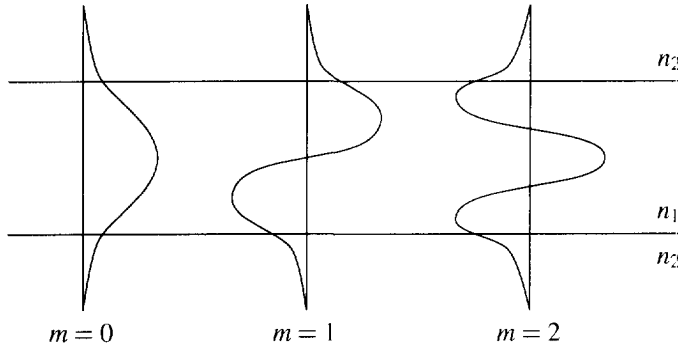


Figure 2.3: Mode profiles in a two dimensional structure of modes with round-trip phase changes $(m + 1)2\pi$. The mode with $m = 0$ is called the fundamental mode.

the cladding layers k_x is imaginary: $k_x = i\gamma$. So there (2.9) turns into

$$\mathbf{E}(x, z) = \mathbf{E}_0(c_u e^{\gamma x} + c_d e^{-\gamma x})e^{-i\beta z}. \quad (2.10)$$

In the top cladding $c_u = 0$, because otherwise far from the waveguide the field would become infinitely large. Likewise, $c_d = 0$ in the bottom cladding. The remaining coefficient can be found by the continuity requirements at the interfaces. By a similar matching of fields at the interfaces, the modes of layer stacks consisting of more than three layers can be found [15].

The spatial profiles thus obtained consist of a cosine-like part in the guiding layer, and exponentially evanescent tails in the cladding layers (see figure 2.3). Note that m , the mode order, is equal to the number of zeros of the cosine profile. The mode with $m = 0$ is called the fundamental mode.

It turns out that in a two-dimensional waveguide there are two classes of field profiles that can propagate as modes in the way described above: one in which the E_x , E_z , and H_y components of the field are all zero, and another in which the E_y , H_x , and H_z components are zero. The first class is said to be TE (transverse electric) polarised, the other to be TM (transverse magnetic) polarised, because for these classes the E- and the H-fields are perpendicular to the plane of propagation, respectively.

TE and TM polarised fields behave differently at interfaces of regions with different refractive indices, because the boundary conditions are different. Therefore, the propagation constant (or the effective index) of an m th order TE mode will generally not be equal to that of the m th order TM mode. Also, the field profiles will usually be slightly different.

2.3.2 Three-dimensional waveguides

In three-dimensional waveguides, i.e., waveguides that provide confinement of the electromagnetic field in two directions, the theoretical description of modal propagation is more complicated. To begin with, the distinction between TE and TM modes becomes less absolute,

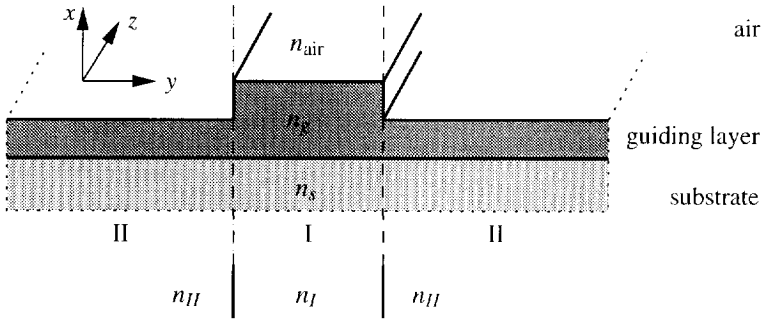


Figure 2.4: Illustration of the Effective Index Method. The effective index n_{eff} that each region (I, II) in the top waveguide would have if it would have been infinitely wide, is taken to construct a two-dimensional waveguide (bottom), the field profile and propagation constant of which approximate that of the original three-dimensional waveguide.

because the field components mentioned above do not become zero completely. When they are small enough, the corresponding mode is usually called “quasi-TE” or “quasi-TM”. But more importantly, for most practical waveguide geometries, an analytical expression for the field profiles can no longer be given. Therefore, the profile and the accompanying propagation constant have to be calculated with numerical means, for example the Finite Element Method [16] or the Method of Lines [17].

A simple, approximative alternative is the Effective Index Method (EIM) [18]. This method transforms the 3D problem into a 2D problem by first considering each of the regions (indicated by I and II in figure 2.4) in the original waveguide as a 2D waveguide that confines the light only in the x -direction. The effective indices of the modes in these regions (n_I , n_{II}) that are obtained by considering these waveguides to be infinitely extended in the y -direction are used as refractive indices in a hypothetical 2D waveguide that confines the light in the y -direction (see the bottom part of figure 2.4). The field profile and propagation constant found are good approximations of the field profile in the y -direction and the propagation constant of the original problem.

The EIM only provides approximate field profiles and propagation constants, because it does not fulfil the boundary conditions at the interfaces between the regions I and II exactly. However, for many practical waveguide structures, it yields results comparable to those of many mathematically more complex methods [19], and sufficiently accurate for design purposes.

2.3.3 Curved waveguides

By using a cylindrical coordinate system (x, ρ, ϕ) (see figure 2.5(a)), propagation of light in circularly curved waveguides can be described in terms of modal propagation. A mode in such a structure is given by

$$\mathbf{E}(\mathbf{r}) = \mathbf{E}_m(x, \rho) e^{-i\beta_m \phi}. \quad (2.11)$$

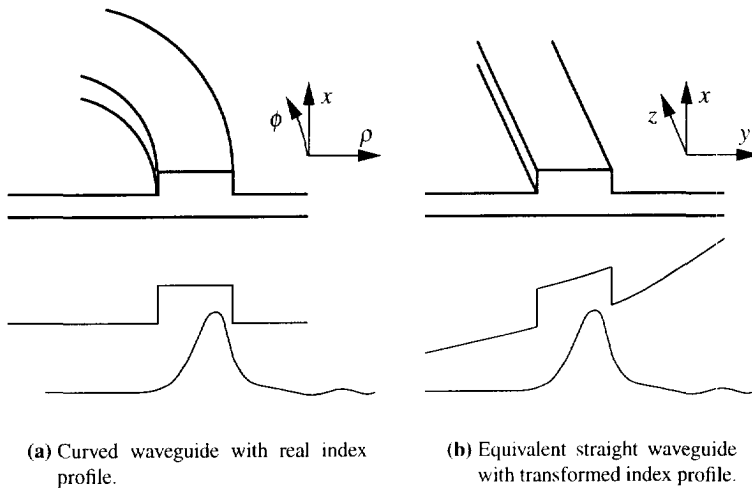


Figure 2.5: In a curved waveguide, the mode profile shifts outward and becomes asymmetric.

This mode has an equi-phase front which propagates in the angular direction ϕ . This implies that, for large ρ , modal power would propagate at a linear speed larger than c , which is, of course, physically not possible. Therefore this part of the power will radiate away and be lost; waveguide bends are inherently lossy, and sharper bends or weaker confinement will increase the loss. By good design, the loss can be kept small enough for practical applications.

It has been shown by Heiblum [20] that, using a conformal mapping technique, the problem of solving the wave equation in cylindrical coordinates can be transformed to rectangular coordinates when the refractive index profile $n(\rho)$ of the waveguide in the wave equation is replaced by $n(\rho)e^{\rho/r_t}$ (with r_t a freely selectable reference radius). With this transformation an ordinary straight waveguide problem is obtained, which can be solved with the EIM by using a staircase approximation for the transformed index profile in the ρ -direction. The shape of the transformed profile can be qualitatively understood by considering that the longer path length of the light travelling in the outside bend has to turn up in the straight waveguide problem as a slower phase velocity, hence the higher index there. Figure 2.5 shows a typical solution in which it can be seen that the centre of gravity of the mode profile in a curved waveguide moves outward, an effect that becomes larger the sharper the bend.

2.3.4 End-to-end coupling of two waveguides

When a waveguide is connected end-to-end with a different waveguide, the modal fields E_m in the second waveguide that are excited by the field E' emerging from the first waveguide can be

denoted

$$E' = \sum_m c_m E_m, \quad (2.12)$$

in which c_m is called the *excitation coefficient* for mode m . Because of the orthogonality of the modes [21] (i.e., $\int E_m E_n^* dy = 0$ for $m \neq n$), it can be shown that

$$c_m = \frac{\int E' E_m^* dy}{\int E_m E_m^* dy}. \quad (2.13)$$

The numerator of the right hand side of (2.13) is called the *overlap integral* of fields E' and E_m . It can be used to calculate the coupling loss occurring at the end-to-end coupling between, for example, a straight and a curved waveguide, as well as the optimal lateral offset needed to compensate for the outward shift of the mode profile in the curved waveguide.

2.4 Device fabrication

Most of the devices described in this thesis are made in the InGaAsP/InP material system. This is a compound III/V semiconductor system with a direct band gap. The binary compound InP is transparent at $\lambda = 1.3$ or $1.55 \mu\text{m}$, the wavelengths important for optical telecommunications. The band gap can be tuned by adding Ga and As, forming quaternary compounds that can emit or absorb light at these wavelengths for the fabrication of lasers and detectors. Waveguides can be produced by epitaxially growing stacks of layers with different refractive indices. Horizontal guiding is accomplished by etching ridges. The material can be p or n doped by adding group II or VI elements, so that electronic devices can also be produced.

2.4.1 Properties of InGaAsP

By assuming Vegard's law, one can easily derive [22] that $\text{In}_{1-x}\text{Ga}_x\text{As}_y\text{P}_{1-y}$ has a lattice constant equal to that of InP when

$$x = \frac{0.1894y}{0.4184 - 0.0130y}. \quad (2.14)$$

Under this condition, the InGaAsP compound can be grown epitaxially on InP. The remaining free parameter can be used to control the band gap according to [22]

$$E_g = (1.35 - 0.72y + 0.12y^2) \text{ eV}. \quad (2.15)$$

The band gap wavelength of InGaAsP can thus be tuned between $0.92 \mu\text{m}$ (InP) and $1.65 \mu\text{m}$ (InGaAs). The refractive index will change as well, enabling the fabrication of waveguides by stacking layers of InGaAsP of different composition.

InGaAsP is usually written without the subscripts; it is then assumed lattice matched with InP, and the band gap wavelength should be specified. Most devices in this thesis have been

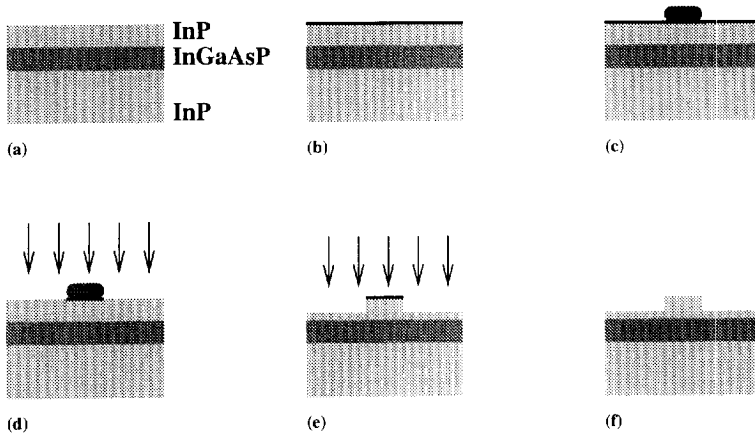


Figure 2.6: Typical fabrication procedure of InGaAsP/InP waveguides. (a) Epitaxial layers are grown on an InP substrate with MOVPE. (b) RF sputtering or PECVD growth of SiO_x or SiN_x mask layer. (c) Spinning on of photo-resist, exposure and developing of mask pattern. (d) Reactive Ion Etching of mask layer with CHF_3 . (e) Removal of photo-resist; RIE of waveguide layers with CH_4/He or CH_4/H_2 . (f) Optional: removal of mask layer; AR coating of end facets after cleaving.

made with a waveguiding layer of InGaAsP with $\lambda_g = 1.3\ \mu\text{m}$, which is transparent for $\lambda = 1.55\ \mu\text{m}$.

Tuning the material composition results in a change of refractive index. Throughout this thesis, to obtain the refractive index of different InGaAsP compounds, the model of Fiedler and Schlachetzki [23] has been used, which is based on interpolation of the experimentally known properties of the binary constituents. The model uses the Sellmeier formula to cater for the wavelength dependence of the refractive index. For $\lambda = 1.55\ \mu\text{m}$, $n = 3.169$ is found for InP, and $n = 3.390$ is found for InGaAsP ($\lambda_g = 1.3\ \mu\text{m}$).

2.4.2 Waveguide processing

Most of the devices described in this thesis have been fabricated with a standard waveguide fabrication process. Specifications of dimensions and deviations from the procedure outlined below are given with the description of each device.

The fabrication process starts with a clean 2" InP wafer, cut and polished along the {001} surface (see figure 2.6). The waveguide layers are grown lattice-matched to the substrate using low pressure metal-organic vapour-phase epitaxy (MOVPE) [24]. Subsequently, a mask layer is deposited on the wafer. Either RF-sputtered SiO_2 or PECVD-grown SiO_x or SiN_x is used for this. The wafer is then diced into slices of approximately $1.5 \times 1.5\ \text{cm}^2$.

A slice is spin-coated with photo-resist and exposed to the circuit layout through a dark field chromium mask that was produced by an electron beam pattern generator (EBPG). Care has to be taken that the input/output waveguides of the circuit are aligned with the [110] crys-

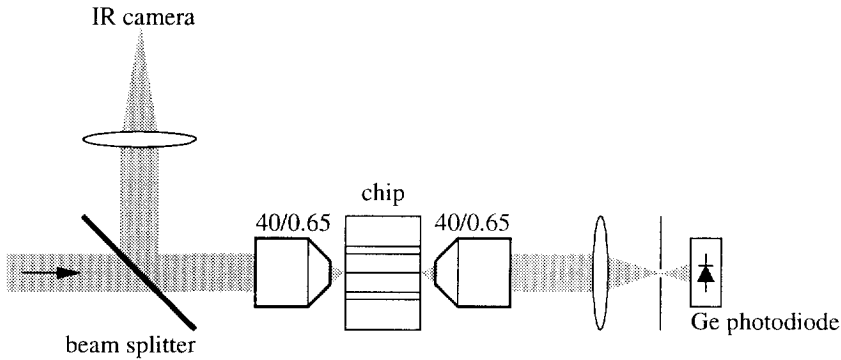


Figure 2.7: Schematic representation of the measurement setup used to perform most measurements presented in this thesis.

tallographic direction for later cleaving. The resist is image-reversal baked and developed, after which the pattern is transferred to the mask layer by CHF_3 reactive ion etching (RIE). Subsequently the photo-resist is removed.

The waveguide ridges are now formed by etching with a CH_4/He or a CH_4/H_2 RIE process. When the desired etch depth has been reached the mask layer can be removed or left in place. (Its influence on the operation of the devices is negligible.) Then, the slice is cleaved perpendicularly to the input/output waveguides to provide in- and outcoupling facets, and, if desired, the cleaving faces are anti-reflection coated by the application of a suitable quarter-wave SiO_x layer.

2.5 Measurement techniques

Measuring the performance of passive photonic integrated circuits often amounts to measuring the power transmission of the devices. The transmission measurements in this thesis have been done with a setup as shown in figure 2.7.

A collimated beam of infrared laser light enters from the left. The beam is chopped with a frequency of around 1 kHz in order to filter the influence of ambient light out of the measurement by means of a lock-in amplifier. The light is projected onto the left cleaved facet of the chip by an anti-reflection coated microscope objective with a numerical aperture of 0.65. In the focal plane of the objective, a spot with a diameter of approximately $4\mu\text{m}$ is formed, that can be focused on the facet and aligned with a waveguide by moving the objective with a piezo-controlled xyz -translator. Part of the incident light will be reflected on the air-semiconductor interface and reaches the IR-camera via the beam splitter. The camera image can be used to focus the spot.

The remaining light will be transmitted into the chip. It will couple into the waveguide with a coupling efficiency determined by the overlap integral of the spot and the waveguide modes. After traversing the integrated optical device, the light will cross the semiconductor-air

interface at the output facet, and be picked up by an identical microscope objective that has its focal plane aligned with the facet. With an additional lens, the light is focused onto a pinhole so that the light emerging from only a single waveguide is detected by the Ge-detector.

Under the assumption that the coupling efficiency to nominally equal waveguides is equal, and that the transmission coefficient of the air-semiconductor interface is equal everywhere along the facet, relative loss measurements can be performed with this method, comparing different devices to each other. Often, the loss of devices is measured relative to that of a straight waveguide.

It is possible to eliminate the coupling efficiency and transmission coefficient contributions with a method known as “transmission measurement with cut-back”. After a series of measurements, the chip is cleaved in two pieces, one of which is used to repeat the measurements. The difference between the two measurements gives the loss in the remaining piece. It is obvious that this method only works when the contributions to be eliminated are equal for the two measurements, i.e., when the cleaving operation yields facets of equal quality to those of the original chip. This method is often used to determine the propagation loss of waveguides.

For optimum accuracy in measuring losses with these methods, coherent effects in the chip should be avoided, e.g., by using a laser with small coherence length, such as a Fabry-Pérot laser, or by minimising the reflectivity of the chip facets by means of an anti-reflection coating.

These coherent effects can also be used on purpose, by what is called the Fabry-Pérot measurement method [25]. Multiple reflections between the facets at both ends of a waveguide cause transmission maxima and minima to occur when an even or an odd number of half wavelengths fits in one round-trip in the cavity, respectively. A number of these maxima and minima can be recorded by tuning the optical length of the chip (e.g., by heating it), or, as in our setup, by tuning the wavelength of the laser. Obviously, for Fabry-Pérot measurements, the laser should have a long coherence length [26]. We use a thermally tuned DFB laser with a linewidth smaller than 100MHz.

The waveguide loss is related to the ratio S between transmission maximum and minimum by

$$L_{\text{wg}} = 10 \log \left(R \frac{\sqrt{S} + 1}{\sqrt{S} - 1} \right), \quad (2.16)$$

in which L_{wg} is in dB, and R is the reflectivity of the chip facets. This is not the plane wave reflectivity of the semiconductor-air interface, but a modal reflection coefficient that can be calculated numerically, and for which Buus [27] has given an analytical approximation. For the waveguides used in this thesis, $R \approx 0.36$ for TE modes, and $R \approx 0.24$ for TM modes. These figures agree with results obtained from Fabry-Pérot measurements of waveguides of which the losses were known from other methods: $R = 0.38 \pm 0.07$ for TE and $R = 0.21 \pm 0.04$ for TM [28].

Both the cut-back method and the Fabry-Pérot method, performed on the reference waveguides relative to which other devices have been measured, can be used to make those measurements absolute.

Chapter 3

Waveguide loss

In this chapter, the most important waveguide loss mechanisms are briefly reviewed. As surface scattering loss is the most important one for state-of-the-art III/V waveguides, two theoretical descriptions of this mechanism in planar waveguides will be discussed. The extension of the resulting model to three dimensions will be used to study scattering loss in ridge waveguides. Variation of waveguide width and etching depth is used to distinguish between surface and sidewall scattering loss.

With a new etching/descumming fabrication process, ridge waveguides have been fabricated on InP with losses below 1 dB/cm for TE polarisation, for effective index contrasts up to 0.03. The loss is composed of a slab waveguide contribution of 0.60 ± 0.05 dB/cm and a varying contribution from scattering at the etched surface beside the waveguide ridge. The ridge sidewall plays a negligible part as scattering loss is concerned. High losses for TM were found (10–20 dB/cm), the explanation for which may lie in the large and laterally extended non-dominant field component of the TM mode of these waveguides.

Deep-etched waveguides fabricated with the same process yielded losses below 1 dB/cm at a width of $2.7 \mu\text{m}$ for both polarisations. The same deep-etching process has been used to fabricate curved waveguides. The strong lateral modal confinement made record sharp bends possible. Curves with radii as small as $30 \mu\text{m}$ exhibited negligible bend loss. This enables changing direction by 90° with low loss on a chip area that can compete with that of a corner mirror. It has to be noted, however, that these bends do not conserve the polarisation.

3.1 Introduction

In an optical waveguide, a number of mechanisms contribute to the loss of part of the guided light. Interaction of light and matter may cause *absorption* or *scattering*, and imperfect guiding can give rise to *leakage* [29]. Absorption results from imperfect material transparency, and is a process in which optical power is converted into other forms of energy. Scattering and leakage remove optical power from guided modes, converting it into radiation.

If the sources of these loss mechanisms are distributed evenly along the waveguide, the guided optical power P decreases exponentially with propagation distance,

$$P(z) = P_0 e^{-\alpha z}, \quad (3.1)$$

in which α is the power attenuation coefficient. When waveguide loss is to be quoted in dB/cm, α can simply be multiplied by $10 \cdot \log e \cdot 10^{-2} \approx 4.34 \cdot 10^{-2}$.

The α in (3.1) should not be confused with the α in the complex wave number $k = \beta - i\alpha$, as in

$$\mathbf{E}(z, t) = \mathbf{E}_0 e^{i(\omega t - kz)} = \mathbf{E}_0 e^{i(\omega t - \beta z)} e^{-\alpha z}. \quad (3.2)$$

In this expression, α is the amplitude attenuation coefficient, directly connected to the complex refractive index according to

$$k = \beta - i\alpha = (n + in'')k_0, \quad \text{so} \quad \alpha = -n''k_0. \quad (3.3)$$

Because the power is the amplitude squared, this α is half of the α in (3.1). Below, the definition of α according to (3.1) will be used.

3.1.1 Absorption

In semiconductor material with a direct band gap, the most obvious absorption mechanism is electron-hole pair creation by a photon whose energy $h\nu$ is larger than the band gap energy E_g . This kind of absorption is often desired, e.g., in detectors, and easily avoided when a transparent waveguide is wanted, by choosing a material composition with a band gap wavelength λ_g far below the operating wavelength. The guiding layer of most of the passive devices described in this thesis is composed of InGaAsP with a λ_g of $1.3 \mu\text{m}$, well below the $1.50\text{--}1.56 \mu\text{m}$ at which the devices operate.

Through intra- and inter-band transitions, free carriers also contribute to absorption. For not-intentionally doped material, with a carrier concentration below 10^{16}cm^{-3} , free carrier absorption loss is typically smaller than 0.1dB/cm , although it can be higher for p-type material due to the greater valence band complexity, which leads to inter-valence band transitions [30].

Impurities, such as Fe doping for obtaining semi-insulating behaviour, can cause near mid-gap energy levels which can lead to losses of 1dB/cm at $\lambda = 1.5 \mu\text{m}$ for a Fe concentration in InP of $5 \cdot 10^{16} \text{cm}^{-3}$ [31]. Similar deep levels can occur in the case of dislocations or other crystal damage.

It is concluded that absorption losses usually can be kept sufficiently small to be neglected.

3.1.2 Scattering

When electromagnetic radiation in a vacuum encounters an object, part of the radiation is scattered depending on the shape and nature of the object. Similarly, when a guided mode experiences irregularities that perturb the ideally smooth waveguide shape, part of its power can be converted to non-guided radiation. These irregularities manifest themselves as variations in the refractive index distribution that constitutes the waveguide. When these variations are

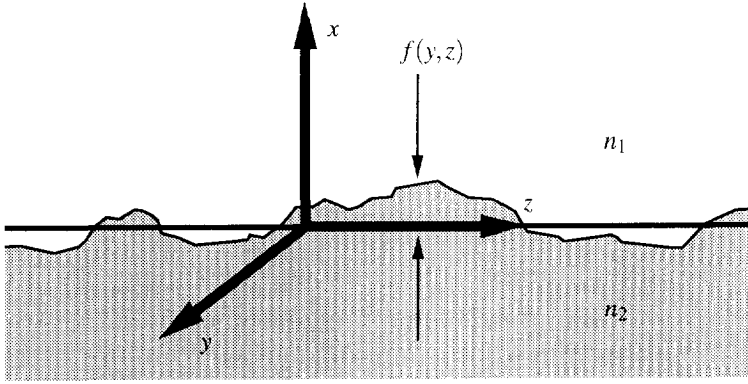


Figure 3.1: Surface roughness perturbing ideally smooth interface.

present as volume inhomogeneities in the material, *volume scattering* occurs. Variations due to an irregular (rough) interface between two regions gives rise to *surface scattering*.

Although the occurrence of volume inhomogeneities in mono-crystalline composite semiconductors is conceivable in the form of local compositional variations, this is an insignificant scattering source in current III-V waveguide technology [29]. Much more important is scattering loss from roughness at epilayer interfaces and etched ridge surfaces.

It is difficult to match theory and experiments concerning scattering loss, because the effect of the roughness depends on a large number of factors, such as the magnitude of the refractive index perturbation (i.e., the refractive index contrast at the interface), the magnitude of the roughness, and its spatial spectrum in the plane of the interface. A single disturbance in a waveguide, even the interruption of the ridge over a few μm in a ridge loaded structure, has negligible influence on the waveguide loss [32], but a perturbation distributed along the waveguide leads to a scattering loss that is largest when the spatial periodicity of the perturbation is of the order of the wavelength of the guided light (cf. the operation of a Bragg grating).

Several theoretical treatments are available for describing scattering in planar waveguides, i.e., waveguides with optical confinement in one dimension only. Unger [33] views the roughness on an interface between two regions of refractive indices n_1 and n_2 (see figure 3.1) as a perturbation of amplitude $f(y,z)$ of an ideally smooth interface lying in the y,z -plane. A volume element $f(y,z) dydz$ of refractive index n_2 can then be described as a region of index n_1 perturbed by the permittivity difference $\Delta n^2 = n_2^2 - n_1^2 (= \epsilon_2 - \epsilon_1)$, and *vice versa*. With this perturbation, Maxwell's equation (2.4) becomes

$$\nabla \times \mathbf{H} = \epsilon_0(n^2 + \Delta n^2) \frac{\partial \mathbf{E}}{\partial t} + \mathbf{j} = \epsilon_0 n^2 \frac{\partial \mathbf{E}}{\partial t} + \mathbf{j}_{\Delta n} + \mathbf{j}, \quad (3.4)$$

i.e., the perturbation has been written as a current. With a harmonic \mathbf{E} -field, this perturbation

$$\mathbf{j}_{\Delta n} = i\omega\epsilon_0\Delta n^2\mathbf{E}_0e^{i\omega t} \quad (3.5)$$

becomes a dipole radiator in the volume element mentioned earlier, with a dipole moment $|\mathbf{j}_{\Delta n}| \cdot f(y, z) dy dz$. When the contributions of dipoles in the y, z -plane are averaged (in which we assume a random distribution for $f(y, z)$), and the far-field Poynting vector S of this ensemble (which describes the radiated energy, and is proportional to $|\mathbf{j}_{\Delta n}|^2$) is integrated over all directions in space, an average radiated power is obtained:

$$\langle P_{\text{rad}} \rangle = \int \int_{\Omega} r^2 \langle S(\Omega) \rangle d\Omega, \quad (3.6)$$

which subtracts from the modal power P :

$$\frac{dP}{dz} = -\langle P_{\text{rad}} \rangle = -(\omega \epsilon_0 \Delta n^2 |\mathbf{E}|)^2 \cdot C. \quad (3.7)$$

Here, the factor $|\mathbf{j}_{\Delta n}|^2$ has been taken out of S and outside the integration, the remainder of which is represented by a certain 'constant' C . If further information is available about the distribution of $f(y, z)$, C can be replaced by an explicit expression containing, e.g., the amplitude and spatial autocorrelation of the roughness [33].

Here we will not go to that length, but combine (3.7) and (3.1), so with $(\Delta n^2)^2 \approx 2n^2(\Delta n)^2$ we find

$$\alpha = 2n^2 C \omega^2 \epsilon_0^2 \cdot (\Delta n)^2 \frac{|\mathbf{E}|^2}{P}. \quad (3.8)$$

The scattering loss turns out to be proportional to the square of the refractive index contrast and the normalised field intensity at the interface. When the approximation $P \approx \int |\mathbf{E}|^2 dx$ is made, the rightmost factor of (3.8), i.e., $|\mathbf{E}|^2 / \int |\mathbf{E}|^2 dx$, is readily calculated with any mode solver.

Tien [34], on the other hand, approaches the problem from a ray-optical perspective. In figure 3.2, a plane wave is shown, incident on the upper waveguide/cladding interface. To cover a unit length on this interface in the z -direction, its width must be $\cos \theta$ in the same units in the direction parallel to the wave front. For a TE wave, the power carried by such a beam is $\frac{1}{2} n_1 E_y^2 \cos \theta$ (per unit length in the y -direction).

With a criterion due to Rayleigh, the fraction of power reflected in the direction of specular reflection is found to be [35]:

$$\mathcal{R} = e^{-\left(\frac{4\pi\sigma_r}{\lambda} \cos \theta\right)^2} = e^{-(2k_x \sigma_r)^2}, \quad (3.9)$$

(see appendix 3.A) with σ_r the statistical standard deviation in the position of the interface and λ the wavelength in the material. This means that the fraction of power lost is $1 - \mathcal{R}$, or $(2k_x \sigma_r)^2$ for small σ_r .

For any mode, the total power flow in the waveguide is $n_1 E_y^2 t_e \sin \theta$, in which t_e is the effective film thickness. The loss per unit length is obtained as the power lost in reflection divided by the total power:

$$\alpha = \frac{\frac{1}{2} n_1 E_y^2 \cos \theta (2k_x \sigma_r)^2}{n_1 E_y^2 t_e \sin \theta} = \frac{2\sigma_r^2 k_x^3}{t_e \beta}. \quad (3.10)$$

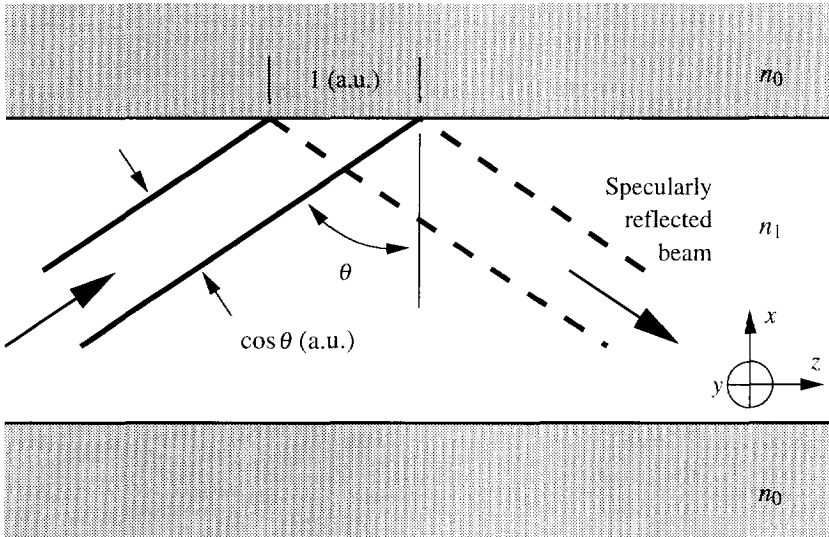


Figure 3.2: Plane wave reflected from top interface.

For a TE mode in a symmetric slab, t_e can be expressed in the field strength at the interface E_s as

$$t_e = 2 \frac{\int E^2 dx}{E_s^2} \frac{k_x^2}{k_0^2 \Delta n^2}. \quad (3.11)$$

Combining this with (3.10), we obtain

$$\alpha = \frac{\sigma_r^2 k_0^2 k_x}{\beta} \frac{E_s^2 \Delta n^2}{\int E^2 dx}. \quad (3.12)$$

With this formula, when the roughness amplitude is known, an estimate for the scattering loss can be calculated. However, this amplitude is a quantity that is generally difficult to measure, although it has been successfully attempted with an Atomic Force Microscope [36]. Usually, the parameter is left as a fittable variable in a series of measurements.

For a ‘typical’ MOVPE grown layer stack shown in figure 3.3, the slab loss was measured in our laboratory by determining the Fabry-Pérot contrast ratio of a very wide ($w \approx 20 \mu\text{m}$) ridge which is so shallow the waveguide only carries a single mode. A loss of $\alpha = 0.5 \text{ dB/cm}$ was found. When it is assumed that the roughness amplitudes of all three interfaces between layers are equal, and the contributions are summed, $\sigma_r \approx 1.0 \text{ nm}$ is found from (3.12). This amounts to about 7 atomic layers.

Unger and Tien have taken fundamentally different approaches to the problem of waveguide scattering loss, and they arrive at different results. It is interesting to note, however, that

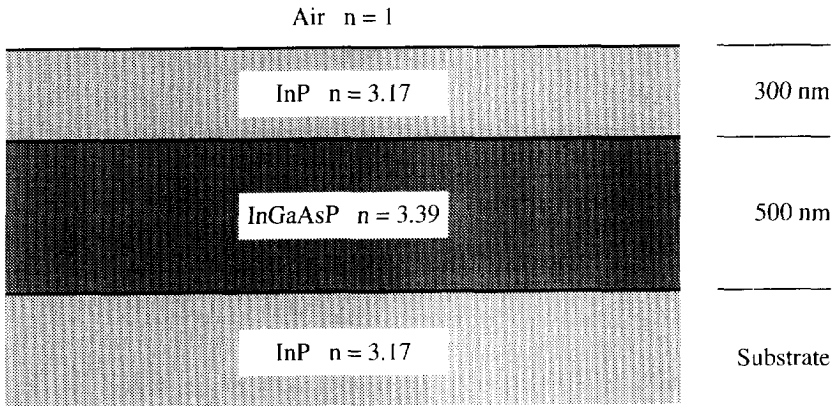


Figure 3.3: Typical layer stack with a measured slab loss of $\alpha = 0.5\text{dB/cm}$.

both (3.8) and (3.12) predict an explicit proportionality of the scattering loss with the (normalised) local field intensity at the interface. The same result is expected when the problem is considered from a particle perspective. The amplitude of the electromagnetic field plays the role of the photon wave function, and the scattering loss can be described as the probability of finding a photon at a scattering centre, which is the normalised wave function squared, times the scattering cross section of this disturbance, which, apparently, increases with increasing refractive index difference, as both theories predict.

The same argument holds for absorption loss. This, too, is equal to the probability of finding a photon inside a certain region, times the absorption cross section of that region. Therefore, absorption loss is also expected to vary linearly with the local field intensity, and experiments in which the distribution of modal power is varied (by varying the waveguide geometry), cannot be used to discriminate between these two loss mechanisms [29]. Other methods, such as determining the wavelength dependence, should be used instead.

On the other hand, varying the distribution of modal power is an excellent method for determining the *location* of sources of scattering and/or absorption loss. The main source of loss in typical ridge and ridge loaded waveguides is not the extremely small roughness at epilayer interfaces, but the waveguide sidewall and surface roughness caused by lithography and etching. By varying the waveguide geometry, it is possible to distinguish between loss occurring at waveguide sidewalls and loss occurring at the etched surface, as will become clear in section 3.2.

It is tempting to extend the methods of Unger and Tien to three dimensions by using the effective index method. This way, slab-like regions are replaced by uniform regions, and the ridge sidewall roughness is transferred to the interfaces between these regions. When this procedure is used, it is implicitly assumed that the main loss mechanism is scattering into slab modes, i.e., into vertically guided surface waves in the original three-dimensional problem. According to a calculation of Hewson-Browne *et al.* [37], this is generally not true: for most

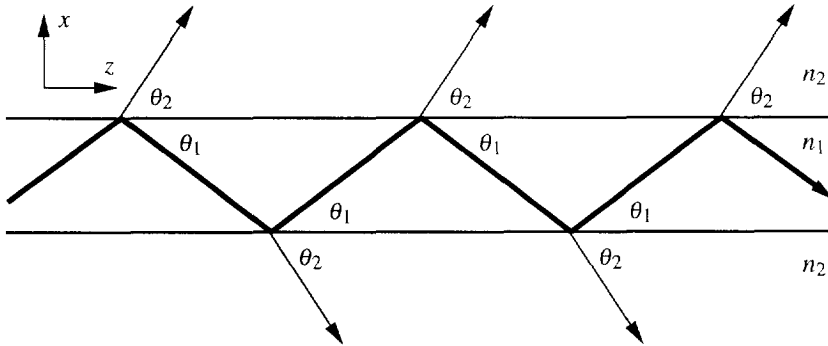


Figure 3.4: A leaky waveguide due to absence of total internal reflection at the waveguide interfaces; $n_1 < n_2$.

practical waveguide geometries, when substrate radiation mode losses are present, they will dominate the slab mode losses.

For that reason, the full two-dimensional waveguide cross-section should be taken into account. From a perturbation approach [38], Deri *et al.* find [39]:

$$\alpha \propto \int_A \Delta n^2 E^2 dA, \quad (3.13)$$

i.e., the loss is proportional to the normalised field intensity times the perturbation, integrated over the entire cross-section. $\Delta n^2 dA$ in (3.13) is comparable to $\Delta n^2 \cdot f(y, z) dy$ in figure 3.1. (Other authors find proportionality with $(\int E dx)^2$ instead of with $\int E^2 dx$. This will be discussed in appendix 3.B.)

A modified form of (3.13) will be used in section 3.2 to determine the location of the main sources of surface scattering loss in InP based ridge loaded waveguides.

3.1.3 Leakage

The final loss mechanism in optical waveguides that will be discussed is that of *leakage*. This is a result of imperfect guiding due to the design of the waveguide geometry. The most obvious case of leakage occurs when the waveguide core is not enclosed between two layers of lower, but of higher index. In that case, total internal reflection at the two interfaces will not occur, and power will leak out of the waveguide; see figure 3.4.

Another possibility is that the waveguide core is enclosed between two lower index layers, but that there is a region of higher index nearby to which optical power can leak, a process not unlike the quantum-mechanical tunnelling of particles through a potential barrier. This situation is very common in GaAs-AlGaAs waveguides, which consist of a GaAs core enclosed by AlGaAs cladding layers, because the $\text{Al}_{1-x}\text{Ga}_x\text{As}$ compounds that can be grown lattice matched on a GaAs substrate have a refractive index lower than that of GaAs. It is necessary to make the lower AlGaAs buffer layer very thick to minimise leakage to the substrate.

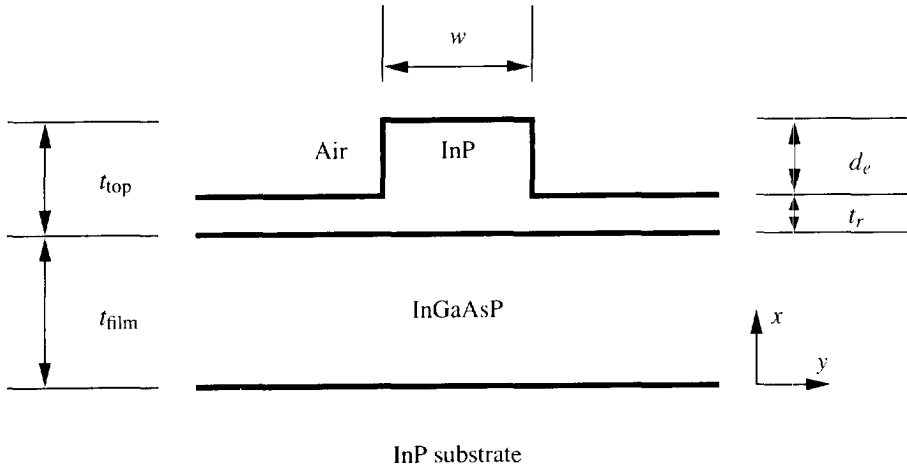


Figure 3.5: Geometry of low index contrast waveguides studied in this section.

In the InP material system, this problem usually does not occur, because the InGaAsP compounds that can be grown lattice matched on InP have higher refractive indices. However, a similar mechanism appears when *waveguide bends* are being used. As has been discussed in section 2.3.3, as far as modal propagation is concerned, a circularly curved waveguide can be described as a straight waveguide with a transformed index profile. In this fashion, bending loss can be qualitatively understood, because the transformation yields a leaky waveguide.

The most important loss mechanism in straight waveguides in the InP material system is roughness arising during reactive ion etching. In the next section, experiments are described that reveal which are the dominant regions of the waveguide cross section contributing to scattering loss, and a new reactive ion etching process is reported that significantly reduces this loss.

The bending loss of curved waveguides can be reduced by increasing the lateral index contrast, thereby effectively increasing the leakage barrier. In section 3.3.4 of this chapter, deep-etched ultra-sharp bends are reported that exhibit low bending loss.

3.2 Scattering loss in straight waveguides

It has been established in section 3.1 that scattering from etched rough interfaces is the main cause of straight waveguide propagation loss. It has been argued that a viable way of finding the locations of the scattering sources is to measure the loss as a function of modal field distribution. The only practical way to vary this distribution is to vary the waveguide geometry (figure 3.5). Usually, just the ridge width w is varied, because this can be done lithographically on a single chip. However, varying the etching depth d_e as well yields much more information.

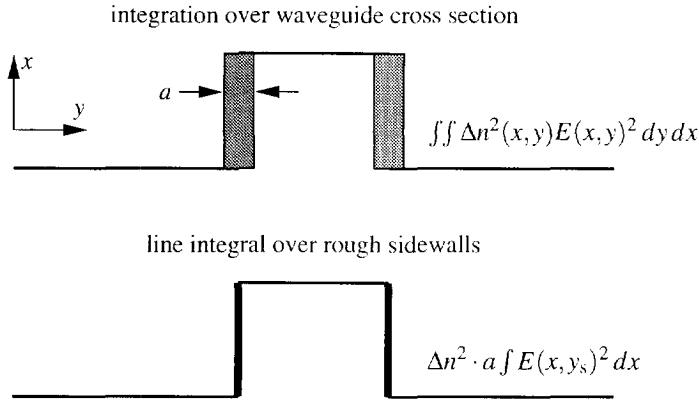


Figure 3.6: The double integral over the waveguide cross-section is replaced by a line integral over the rough interface times the roughness amplitude.

In particular, this can be used to distinguish between scattering from the ridge sidewall and scattering from the etched surface beside the ridge [39]. For the experiments described in this section, ridges with $w = 0.6 \dots 1.6 \mu\text{m}$ and varying heights have been etched in layer stacks as depicted in figure 3.3.

3.2.1 Calculation of field intensity at an interface

In the scattering loss calculations in this section, the field intensity at the rough surface is assumed to vary in an approximately linear fashion in the direction normal to the surface, which is a valid assumption when the region a , in which the waveguide is perturbed, is small (see figure 3.6). Integration of $E(x,y)^2$ over y in this region can therefore be replaced by a multiplication of the average field intensity $E(x,y_s)^2$ by the width of the integration region a (where y_s is the average position of the interface, and a can be identified with the average roughness amplitude). Since the perturbation $\Delta n^2(x,y)$ is zero everywhere except near the interface, the original integral over the entire waveguide cross section reduces to a line integral over the interface under consideration, and (3.13) changes into

$$\alpha = c \cdot \frac{\Delta n^2 \int E(x,y_s)^2 dx}{\int_A E(x,y)^2 dA} = c \cdot I, \tag{3.14}$$

where Δn^2 now is a constant that describes the squared index step at the interface. The roughness amplitude has been worked into the proportionality constant c . In this expression, I is the field intensity integral, weighted by Δn^2 . I will be used below to relate contributions from different interfaces and results from different calculation methods, and c will be used as a fit parameter.

Figure 3.7 presents a comparison of results obtained with (3.14) and with (3.12). The two-dimensional fields for (3.14) have been calculated with a scalar finite element method (FEM)

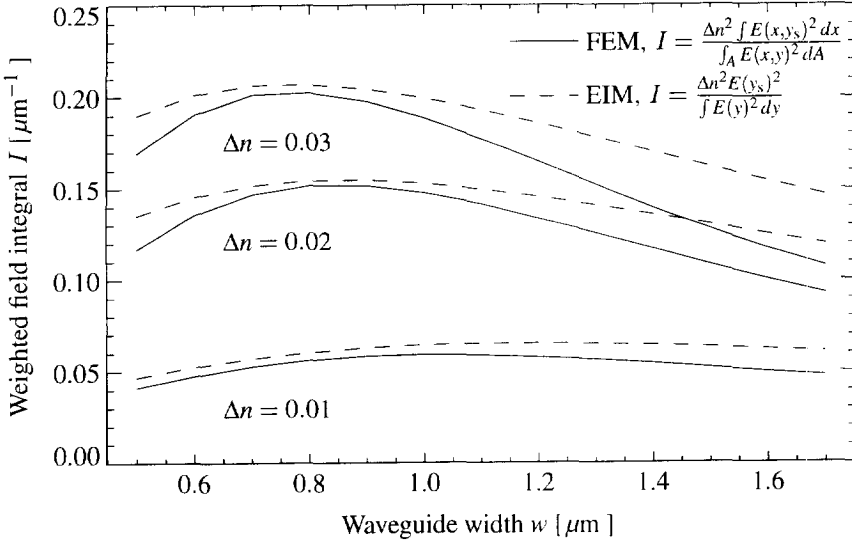


Figure 3.7: The normalised field intensity through the waveguide sidewall, weighted by Δn^2 . Results are plotted for the waveguide geometries listed in table 3.1.

Index contrast (Δn)	0.01	0.02	0.03
t_{top}	300 nm	400 nm	300 nm
d_e	195 nm	350 nm	285 nm
t_r	105 nm	50 nm	15 nm
N_{ridge}	3.291	3.293	3.291
N_{slab}	3.278	3.270	3.262
Δn^2	0.08	0.15	0.19

Table 3.1: Index contrasts of three samples available for experiment. All samples contain ridge waveguides as drawn in figure 3.5, with a film thickness of 500 nm, and widths ranging from 0.6 to 1.6 μm .

mode solver developed at the ETH Zürich [19], and the fields for (3.12) have been obtained with the effective index method (EIM). All calculations in this section are for TE polarisation at a wavelength of 1535 nm.

Three different values of the index contrast have been used in the calculations, in accordance with the samples available for experiments as listed in table 3.1. The samples have different top layer thicknesses, but this makes almost no difference for the effective index of the region under the ridge, as is shown in figure 3.8. The important parameter is the thickness of the part of the top layer that remains on the slab after etching, t_r , as depicted in figure 3.5. The effective index contrast varies almost linearly with this parameter for $t_r \leq 100$ nm. The set of samples can therefore be considered as a series in which only the etching depth has been

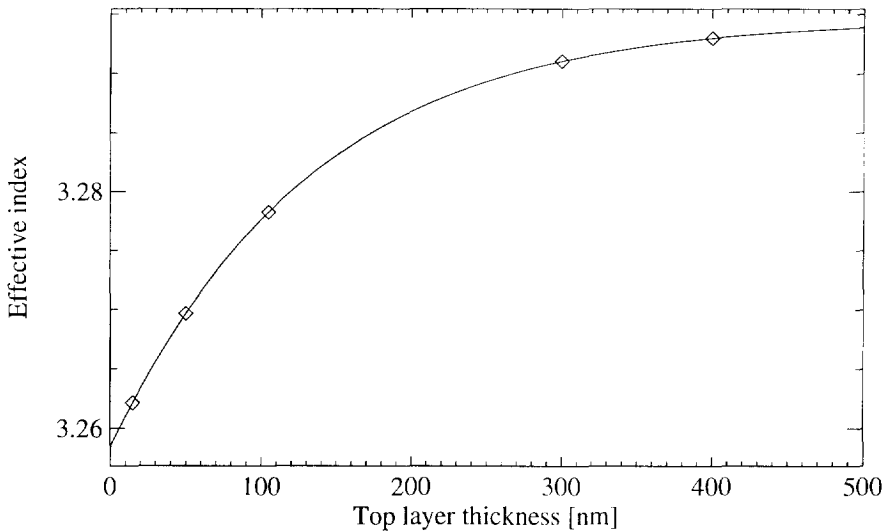


Figure 3.8: The effective index of a slab waveguide (figure 3.3) as a function of the top layer thickness. The parameters for the available samples of table 3.1 are indicated with \diamond . The remaining thickness after etching (in the range 0... 100 nm) has a large influence, while different top layers above the ridge ($t_{\text{top}} \geq 300$ nm) make almost no difference.

varied.

It is noticeable in figure 3.7 that the qualitative behaviour of the two methods is very similar. In the maxima of the curves, the two methods come very close indeed, and remain almost equal under variation of the index contrast. Furthermore, the shape of the curves is comparable, although the FEM calculations exhibit larger w -dependence. The figure suggests that, if scattering mainly occurs at the waveguide sidewall, a calculation on the basis of the EIM will give reasonably accurate insight into the trends of waveguide loss when w and Δn^2 are varied (for small w), obviating the need to do a (relatively lengthy) two-dimensional modal field pattern calculation.

However, inspection of the two-dimensional mode profiles (figure 3.9) suggests that if scattering occurs at the waveguide sidewalls, it might occur at the etched surface next to the ridge as well. Of course the distribution of roughness on this surface will differ from that on the sidewall, because the mechanisms contributing to it are different, but due to the relatively large field intensity at this surface, some scattering is bound to take place here.

In figure 3.10, the FEM results for the field intensity integrated along the waveguide sidewall from figure 3.7 are plotted together with the field integral along the etched surface. It is apparent that the dependence on the waveguide width is much larger for the surface than it is for the sidewall. On the other hand, the index contrast dependence is much smaller: the integral along the etched surface (dotted) changes only 35% for waveguide widths around $0.6 \mu\text{m}$ when the index contrast changes from 0.01 to 0.02, while the integral along the sidewall (solid)

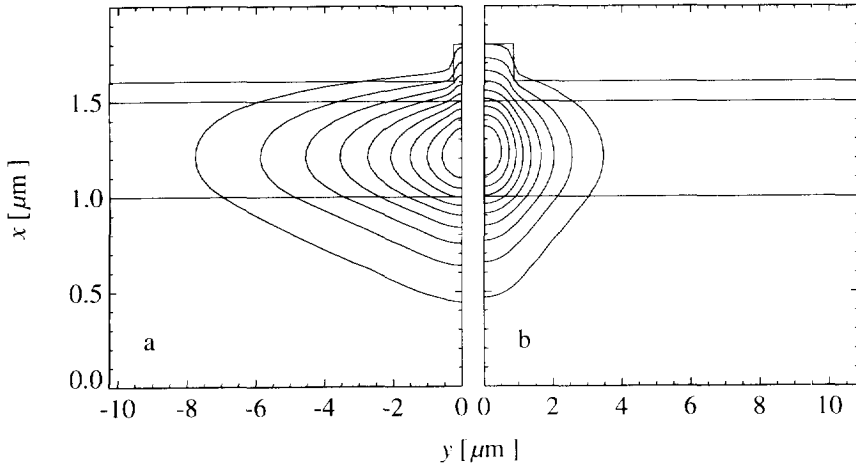


Figure 3.9: Field profiles (symmetric about the axis $y = 0$). a: ridge width $0.5\mu\text{m}$; b: ridge width $1.7\mu\text{m}$. The index contrast is 0.01.

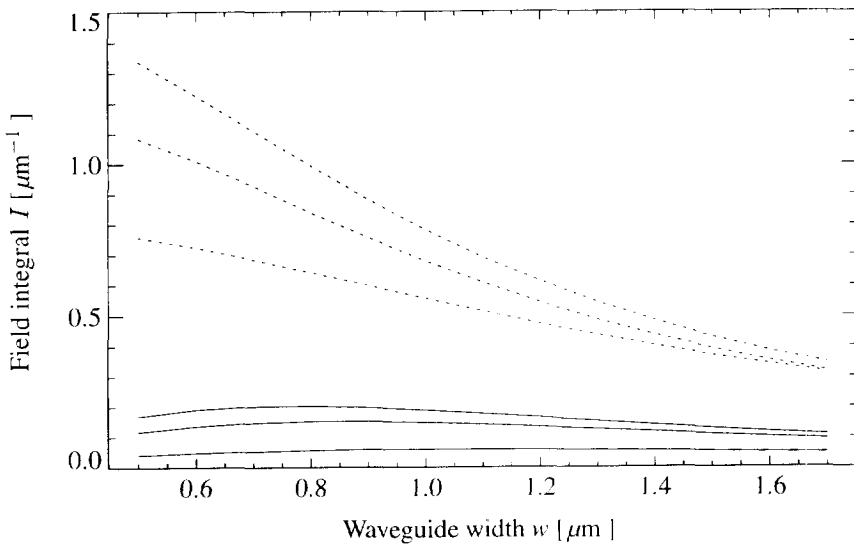


Figure 3.10: The normalised field intensities through the waveguide sidewall (solid) and the surface beside the waveguide (dotted), times Δn^2 , calculated from (3.14). Top to bottom: index contrast 0.03, 0.02, 0.01.

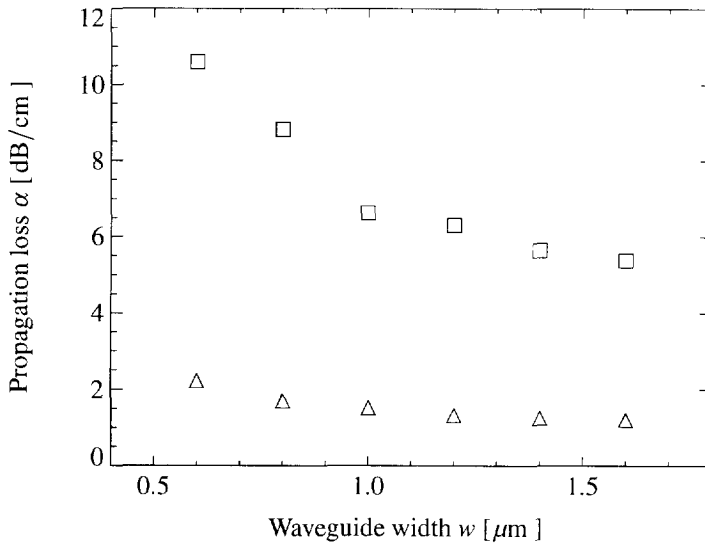


Figure 3.11: The propagation loss of waveguides etched with a standard CH_4/He process (\square), and with etching/descumming (\triangle).

changes by almost a factor of three. Therefore, varying the width and the index contrast can be used to distinguish between surface scattering and ridge sidewall scattering.

3.2.2 Fabrication of low loss waveguides

A loss $\alpha = 0.5 \text{ dB/cm}$ has been found for slab waveguides as depicted in figure 3.3. When a ridge of around $1 \mu\text{m}$ width is etched in such a slab, the loss is raised to a few dB/cm (see the \square symbols in figure 3.11). The mask consists of 70 nm of RF-sputtered SiO_2 . The etching is done with a dry reactive ion etching (RIE) process using a CH_4/He mixture. The etch rate of a process with gas flows $\text{CH}_4 : \text{He} = 4 : 50 \text{ SCCM}$ at a pressure of 60 mTorr and an RF power of 0.4 W cm^{-2} is 18 nm min^{-1} [40]. Processes like this one, with CH_4/He or CH_4/H_2 chemistries, are known to cause deposition of hydrocarbon polymer on inert masks [40, 41]. The deposition rate for the above process is 6 nm min^{-1} . Deposition on the mask edge increasingly shields the sidewall from the etchants, which results in a sloping wall. Because the deposition on the edge is not homogeneous, sidewall roughness occurs due to the formation of vertical striations.

With the cleaning properties of an O_2 plasma in mind, one would presume that deposition of polymer could be avoided by adding O_2 to the etching mixture. This has indeed been found: small amounts reduce sidewall roughness and improve its verticality [42]. However, experiments with O_2 flows above 2 SCCM , the minimum possible on the etching system used [43], showed that etch rates drop dramatically and the etched surface becomes very rough. Apparently, only very small O_2 flows give good results.

Another possibility is taking multiple sequential steps of etching with CH_4/H_2 or CH_4/He

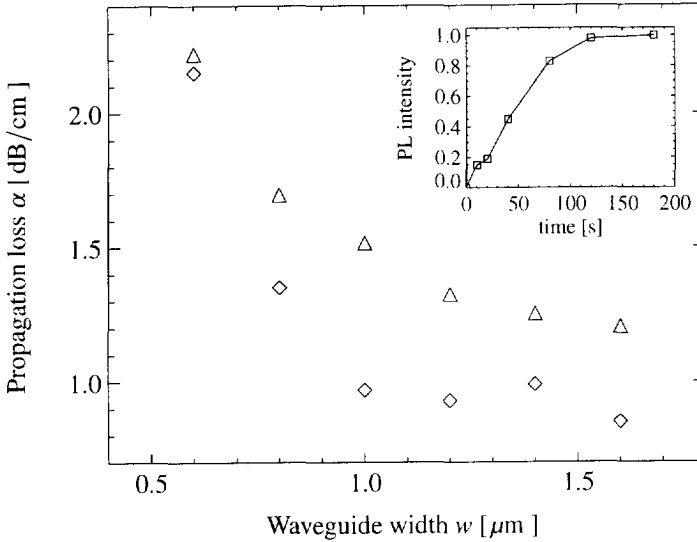


Figure 3.12: The propagation loss of waveguides before (\triangle) and after (\diamond) a 3 min isotropic polishing etch with H_2SO_4 . The inset shows the recovery of the photoluminescence intensity relative to an unetched InP substrate, as a function of etching time.

and cleaning with O_2 in the same etching run [41, 43]. Thus, each oxygen cleaning step removes the polymer film deposited by a short etching run. Extremely vertical (1.6°) and smooth sidewalls have been obtained with this method. An important advantage is that the etching and the cleaning (*'descumming'*) steps can be optimised separately.

A process has been developed in which ridges are made by alternately etching for 5 min with CH_4/He with the parameters detailed above, and descumming for 30s with 50SCCM O_2 under the same process conditions. With longer etching times, horizontal steps were observed along the ridge, which correspond to the switching of etching to descumming. Longer descumming affects the mask, while shorter descumming does not completely remove all deposited polymer. This etching/descumming process significantly reduces the waveguide loss, as determined from Fabry-Pérot contrast measurements (figure 3.11).

The loss can be reduced even more by applying an isotropic polishing etch with concentrated H_2SO_4 after RIE in order to remove the damaged InP-surface; see figure 3.12. The inset in the figure shows that the photoluminescence intensity, which is very sensitive for surface damage, is entirely recovered after 3 min of etching with H_2SO_4 [40].

3.2.3 Experimental results

Medium contrast

Figure 3.13 shows the losses of waveguides with three different effective index contrasts, fabricated by etching/descumming and polishing with H_2SO_4 . The data have been meas-

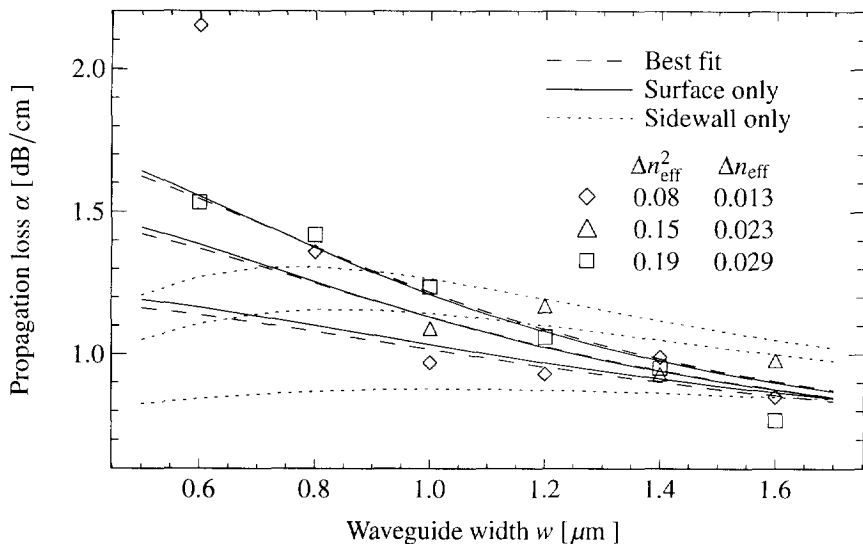


Figure 3.13: The propagation loss of waveguides with varying effective index contrast for TE polarisation, and least-squares fits to the field contributions I . Evidently, the surface scattering contribution is the most important one.

ured by determining the Fabry-Pérot contrast of the waveguides for TE polarised light at the wavelength $\lambda = 1535 \text{ nm}$ [44]. The points are averages of the losses of one to eight nominally equal waveguides, depending on the number of defect ones. The standard deviation of separate measurements of nominally equal waveguides is about 0.2 dB/cm , which is more than the reproducibility of about $0.05\text{--}0.1 \text{ dB/cm}$ for measuring the same waveguide over and over. This is probably due to randomly distributed discrete defects [29]. Defects also cause some waveguides, especially the smallest ones, to have anomalously high loss. The total standard error for the points in figure 3.13 is about 0.1 dB/cm .

As seen, losses as low as 1 dB/cm (including a slab waveguide loss of 0.5 dB/cm) can be obtained for waveguides as small as $1.4 \mu\text{m}$ with index contrasts as high as 0.03 . For wider waveguides, the waveguide loss approaches the slab loss. The data have been fitted to the expression

$$\alpha = \alpha_{\text{slab}} + c_{\text{su}} I_{\text{su}} + c_{\text{si}} I_{\text{si}}, \tag{3.15}$$

where I_{su} and I_{si} are the weighted field intensity integrals along the surface next to the waveguide ridge and the ridge sidewall, respectively, calculated according to (3.14), and α_{slab} , c_{su} and c_{si} are fit parameters. α_{slab} plays the part of the constant contribution of the slab waveguide loss. The points for the lowest contrast waveguides of widths 0.6 and $0.8 \mu\text{m}$ have been ignored in the fitting procedure, because they clearly deviate.

The solid lines in figure 3.13 represent a fit where only the contribution of the etched surface has been taken into account, i.e., c_{si} has been forced to zero. This results in $c_{\text{su}} = 0.78 \pm 0.08 \text{ dB/cm} \cdot \mu\text{m}$ and $\alpha_{\text{slab}} = 0.60 \pm 0.05 \text{ dB/cm}$. The root-mean-square deviation of

Fit (fig. 3.13)	Surface (solid)	Sidewall (dotted)	Both (dashed)
α_{slab}	$0.60 \pm 0.05 \text{ dB/cm}$	$0.69 \pm 0.10 \text{ dB/cm}$	0.59 dB/cm
c_{su}	$0.78 \pm 0.08 \text{ dB/cm} \cdot \mu\text{m}$	0	$0.74 \text{ dB/cm} \cdot \mu\text{m}$
c_{si}	0	$3.0 \pm 0.8 \text{ dB/cm} \cdot \mu\text{m}$	$0.26 \text{ dB/cm} \cdot \mu\text{m}$
$\sigma_{\text{su,si,both}}$	0.07 dB/cm	0.14 dB/cm	0.07 dB/cm

Table 3.2: Parameters deduced from fitting (3.15) to the measured data in figure 3.13.

the fit from the measurements is $\sigma_{\text{su}} = 0.07 \text{ dB/cm}$.

The dotted lines in figure 3.13 represent a fit where only the contribution of the waveguide sidewall has been taken into account, i.e., this time c_{su} has been forced to zero. This results in $c_{\text{si}} = 3.0 \pm 0.8 \text{ dB/cm} \cdot \mu\text{m}$ and $\alpha_{\text{slab}} = 0.69 \pm 0.10 \text{ dB/cm}$. The root-mean-square deviation of the fit from the measurements is $\sigma_{\text{si}} = 0.14 \text{ dB/cm}$. Evidently, this fit is much worse than the previous one.

The dashed lines in figure 3.13 represent a fit that involves all three parameters. The results now are $c_{\text{su}} = 0.74 \text{ dB/cm} \cdot \mu\text{m}$, $c_{\text{si}} = 0.26 \text{ dB/cm} \cdot \mu\text{m}$ and $\alpha_{\text{slab}} = 0.59 \text{ dB/cm}$. The RMS deviation is $\sigma_{\text{both}} = 0.07 \text{ dB/cm}$. (σ_{both} has improved in the fourth decimal with respect to σ_{su} .)

It can be concluded that waveguide loss for the geometries studied can be adequately described by $\alpha = (0.59 + 0.74 I_{\text{su}} + 0.26 I_{\text{si}}) \text{ dB/cm}$, where the constant slab loss contribution is in good agreement with what has been found earlier, and the sidewall contribution is 10 to 20 times smaller than the etched surface contribution for all the points measured. The results are summarised in table 3.2.

For TM polarisation, some measurements have been plotted in figure 3.14. These measurements have been done in transmission with the cut-back method, because the losses were too high to obtain appreciable Fabry-Pérot fringes. Losses were high for all samples, and showed no clear dependence on index contrast or waveguide width, although they generally seemed lower for higher index contrast.

An explanation for these losses can be sought in the mode profile of the fundamental TM mode. With scalar methods, nothing special could be discerned, but with a vectorial finite element method mode solver developed at the ETH Zürich [19], the modal field profile in figure 3.15 was found. The x -component, which gives the mode its TM character, looks normal, but the y -component, which is the non-dominant field component for this polarisation, and is usually very small, accounts for 2.5% of the power (whereas for TE polarisation the non-dominant x -component only accounts for 0.07%), and extends far to both sides. This shape has actually been observed at the output facet of the chip using a polariser. Because the waveguides on the measured chips lie $20 \mu\text{m}$ apart, the extent of the component can cause coupling to adjacent waveguides. This, too, has been observed: about as much power was seen in adjacent guides as in the guide under measurement. This can explain the highly irregular behaviour of the TM loss, because this coupling effect is of course very dependent on the length of the chip.

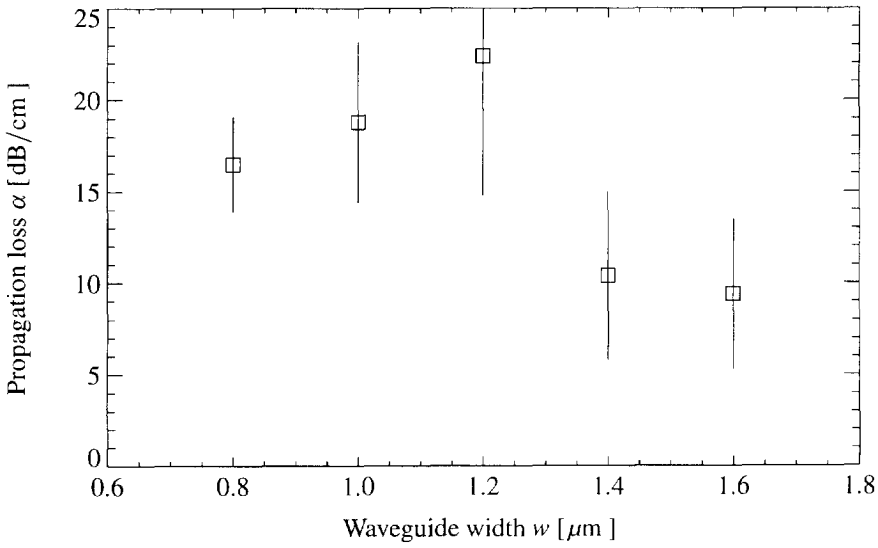


Figure 3.14: The propagation loss of of the lowest contrast waveguides (etch depth 195 nm) for TM polarisation. Both the losses and their scatter are large.

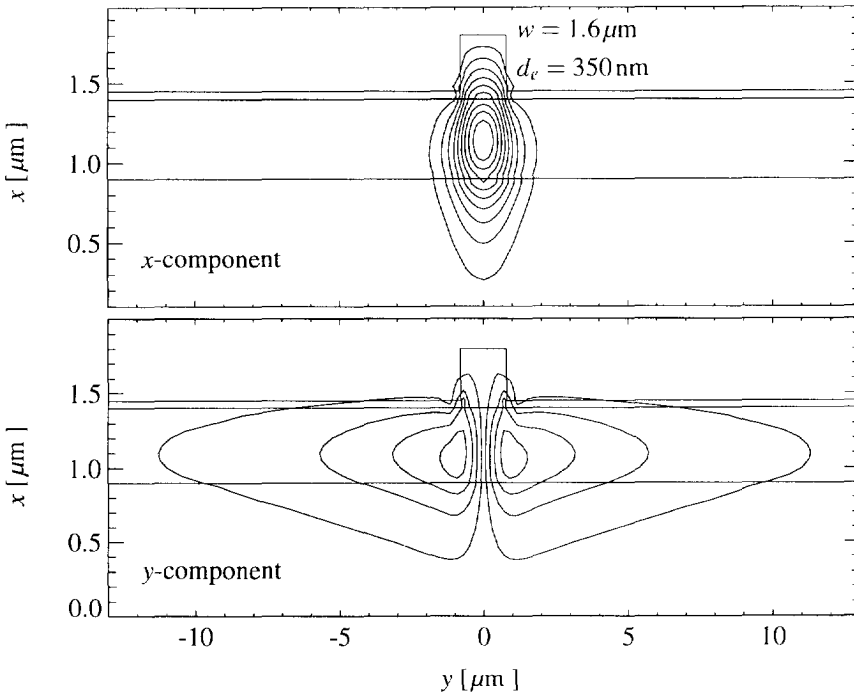


Figure 3.15: Profiles of two components of the electric field for TM polarisation.

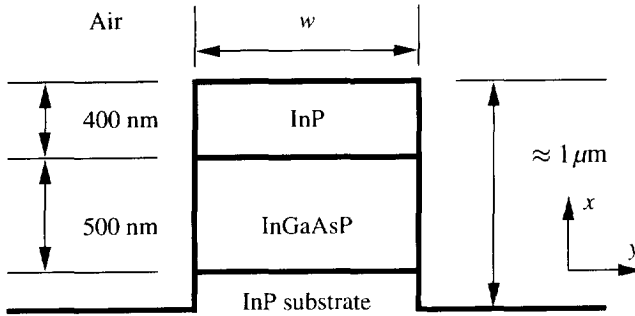


Figure 3.16: Geometry of deep-etched waveguides.

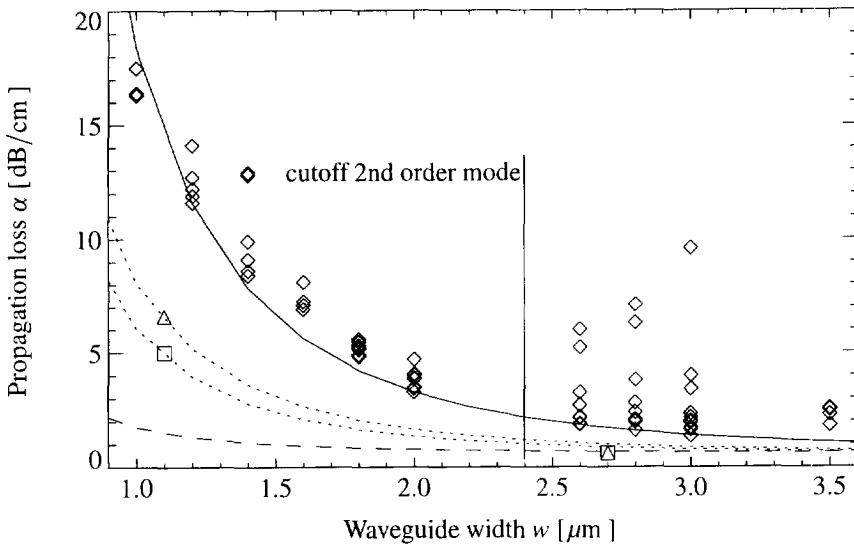


Figure 3.17: Measurement results: \diamond TE loss measured with Fabry-Pérot. \triangle and \square : other processing run measured with cut-back; TE and TM, respectively. Lines: see text.

Calculations show that the TM behaviour described here diminishes for waveguides wider or more deeply etched than the ones discussed in this section.

High contrast

The etching/descumming process described in paragraph 3.2.2 has been used to fabricate deep-etched waveguides as depicted in figure 3.16. Measurement results are given in figure 3.17. Data from two different processing runs are plotted. The points indicated with \diamond are from a chip that has been fabricated with a CH_4/He etching/descumming process followed by a wet polishing etch, while the points \triangle and \square are from a chip etched with a CH_4/H_2 etching/

descumming process. (For the latter see also section 3.3.4.) A scanning electron micrograph of the cross section of the waveguides from the first run (\diamond) showed a non-rectangular waveguide shape with steps at the InP/InGaAsP interfaces. This can be ascribed to the selectivity of the H_2SO_4 polishing etch. For this reason, the polishing etch was omitted for subsequent deep-etching runs. (Obviously, the polishing etch posed no problems for the shallow etch, because no InP/InGaAsP interfaces were exposed.)

Waveguides of the geometry of figure 3.16 support three or more modes when $w > 2.4\mu\text{m}$, so Fabry-Pérot measurements are expected to become difficult, as can be gathered from the larger scatter in the data for the waveguides of $2.6\mu\text{m}$ and wider. For some waveguides, behaviour of the Fabry-Pérot fringes characteristic for multi-mode waveguides was observed.

The solid line represents a fit of the field intensity through the waveguide sidewall to the losses of the lowest loss waveguides of widths 2 to $3\mu\text{m}$. This procedure yields $\alpha = (0.53 + 11.3 \cdot I)$ dB/cm, which seems to reasonably describe the losses of the best waveguides smaller than $2\mu\text{m}$ as well. The coefficient of the field intensity term is an order of magnitude larger than the coefficients found for the low contrast waveguides in table 3.2. (The dashed line in figure 3.17 indicates the behaviour that would have been expected on the grounds of this smaller coefficient.) The difference might be explained by a different type of roughness that may have been formed due to prolonged exposure to the RIE plasma, in combination with the anomalous waveguide profile.

The other points in figure 3.17 originate from the chip etched with the CH_4/H_2 process without wet polishing etch. The waveguides have the expected rectangular shape. The losses are considerably lower than those of the previous chip. The waveguides have been measured in transmission using cut-back. Fabry-Pérot measurements for the $1.1\mu\text{m}$ wide waveguides correspond to the cut-back results to within 0.5 dB/cm. Fabry-Pérot results for the $2.7\mu\text{m}$ wide waveguides produced values of 2.0 dB/cm for both polarisations, which is probably due to the multi-mode behaviour mentioned above. The dotted lines have no function other than to guide the eye. The TM loss (\square) is slightly smaller than the TE loss (\triangle). The TM mode is confined better than the TE mode, but the difference in confinement is too large to explain the difference in measured loss.

It can be concluded that the trends in the loss depending on waveguide width and polarisation can be explained by sidewall scattering, but an accurate quantitative description can not be given. This is partly because, as repeated processing runs have shown, the results are very dependent on the condition of the etching chamber.

3.3 Waveguide bends

Even though straight waveguides as treated in the previous sections of this chapter are useful integrated optic elements to interconnect components, some method to introduce a directional change is necessary in order to exploit the full two-dimensional surface of the chip.

An obvious way to make light go around the corner is using a mirror. Use of corner mirrors in integrated optical circuitry has been proposed by Benson in 1984 [45]. Another option, made possible by the fact that the light in question is confined in a waveguide, is to bend the

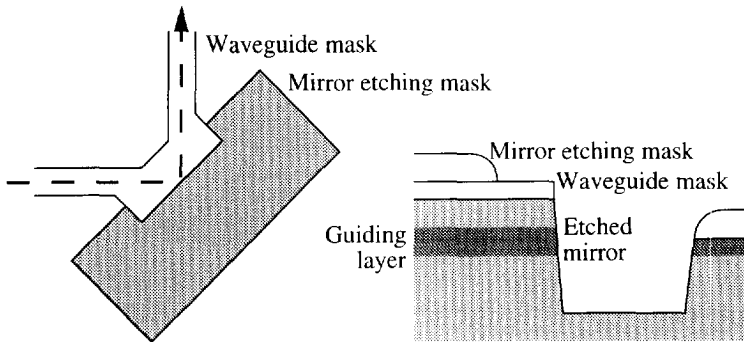


Figure 3.18: Typical geometry of a self aligned corner mirror. After waveguide etching, a mask with holes for the mirror etch is placed. The edge of the waveguide mask is still used to determine the position of the mirror.

waveguide, and make the light go through a smooth turn [46].

Each of these approaches has its own specific advantages and disadvantages. Curved waveguides can be made with extremely low (radiation) loss, but only for rather large bending radii. The mirror solution, on the other hand, results in extremely small components (a few hundred μm^2), at the cost of a higher loss (typically 1 dB/90°). In this section, ultra-sharp waveguide bends, which combine the low loss of bends with the extremely small size of corner mirror structures, will be presented [47]. For comparison, first some aspects of corner mirror and bend fabrication and performance will be discussed.

3.3.1 Corner mirrors

Corner mirrors on semiconductor material are typically fabricated in a self-aligned two-step process with a geometry as shown in figure 3.18. The waveguides are patterned in the first masking step, which also defines the position of the mirror, and then etched to the desired depth. The second masking step protects the entire chip, except for an etching window left at the position where the mirror is to be formed by a deep-etching step.

Total internal reflection would theoretically ensure low loss reflection. However, there are a number of critical parameters that make it difficult to attain low loss corner mirrors:

1. It is very important that the etched mirror facet is at right angles with the chip surface. A slight tilt, as shown in the figure, will reflect part of the light into the substrate instead of coupling it into the output waveguide. Therefore, an etching process optimised for facet verticality must be used. But even at angles of only 1.6° (obtainable with the optimised etching/descumming process described above), 0.5 dB loss can result [48].
2. Misalignment of the mirror facet will cause an offset between the reflected beam and the output waveguide, which can cause about 0.5–1 dB loss for $0.2\mu\text{m}$ misalignment [49].

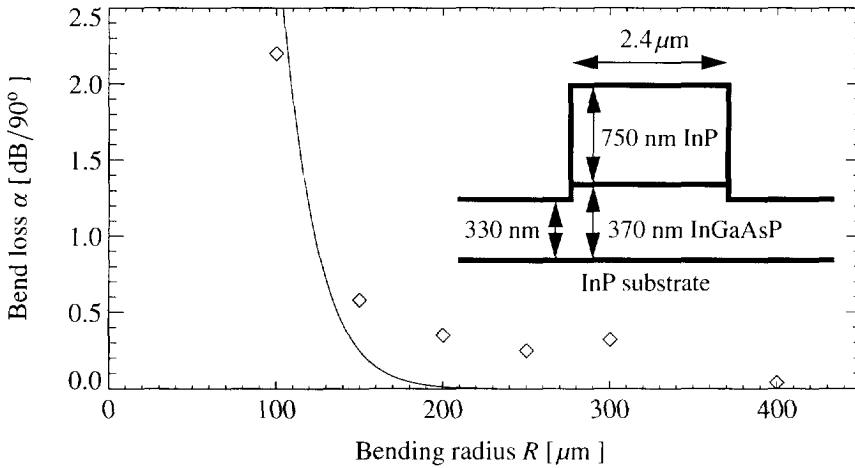


Figure 3.19: Radiation loss in a curved waveguide. The points are measurements from [51]. The solid line is a calculation on the basis of the EIM and a conformal transformation [20]. The inset shows the waveguide structure.

In a self-aligned fabrication process, such a mismatch can occur due to mask erosion during etching. Also, a tilt of the facet will influence the effective position of the mirror.

3. Finally, the facet roughness induced by imperfections in the mask or the etching process will introduce additional mirror loss, which is typically of the order of 0.5 to 1 dB for 90° mirrors [50].

The losses cited above are typical values which are, of course, dependent on waveguide geometry. It is clear that the mirror etch process must be optimised for high anisotropy (facet verticality), low mask erosion and low roughness etching—conditions which are difficult to combine. At present, 90° mirrors with a loss of 0.8 dB [50], and 45° mirrors (with multi-mode waveguides) with a loss of 0.3 dB have been reported [49].

3.3.2 Curved waveguides

In comparison with corner mirrors, directional change by means of curved waveguides is relatively easy to accomplish. The bends are simply waveguides, so no additional masking or etching steps are needed. There are, however, some aspects that need consideration.

1. Curved waveguides have radiation loss, the more so the smaller the radius of curvature. In figure 3.19, this effect is demonstrated. Typically, the radiation loss is negligible for large radii, but below a certain radius it quickly rises to unacceptable values. The radius around which this happens can be decreased by applying a larger refractive index contrast.

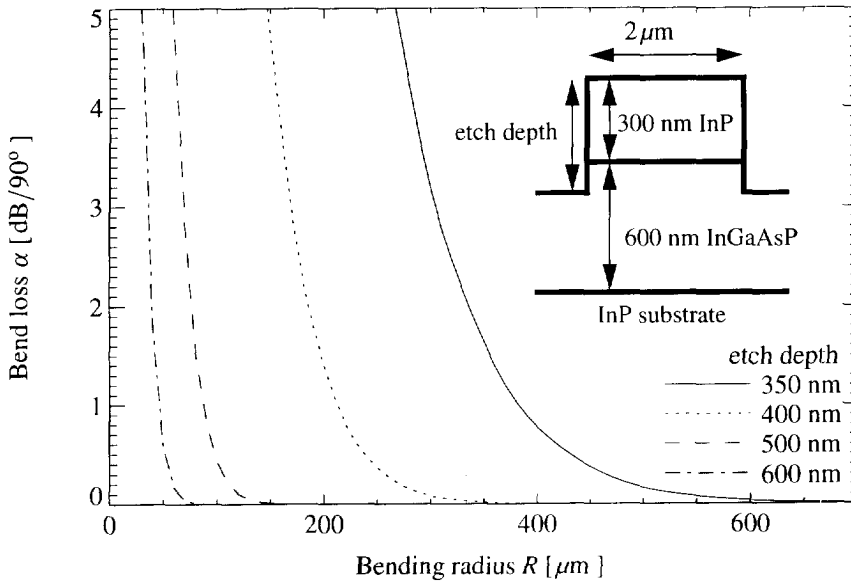


Figure 3.20: An increased etching depth decreases radiation loss, and consequently allows sharper bends. Calculation with EIM and conformal transformation.

2. In a bend, the optical mode shifts towards the outer edge of the waveguide. This shift is larger for smaller bending radii, and leads to coupling loss at the connection between waveguide sections with different radii of curvature. The application of a well-optimised offset at such a connection [52] typically reduces this loss to below 0.1 dB.

Waveguide bends thus allow for directional change with extremely low loss, at the cost of using a considerably larger chip area than a corner mirror would have needed.

3.3.3 High contrast curved waveguides

The radiation loss suffered in a bend can be reduced by increasing the mode confinement, e.g., by deeper etching, as illustrated by figure 3.20. Etching completely through the waveguide core presents the limiting case of this, with the additional advantage that the exact etching depth ceases to be of interest.

Pennings [53] describes a simple method for estimating usable bending radii of deep-etched ridge waveguides, based on the width of the waveguide and the effective indices of its regions, as well as the modal effective index for a straight waveguide. In this method, the effective index of the air regions beside the waveguide, which of course guide no slab modes, is taken to be unity. This usually results in the EIM giving fairly good approximations to the modal effective index, as compared to calculations with a scalar FEM (better than 1% for $w \geq 1 \mu\text{m}$ in the present waveguide structure).

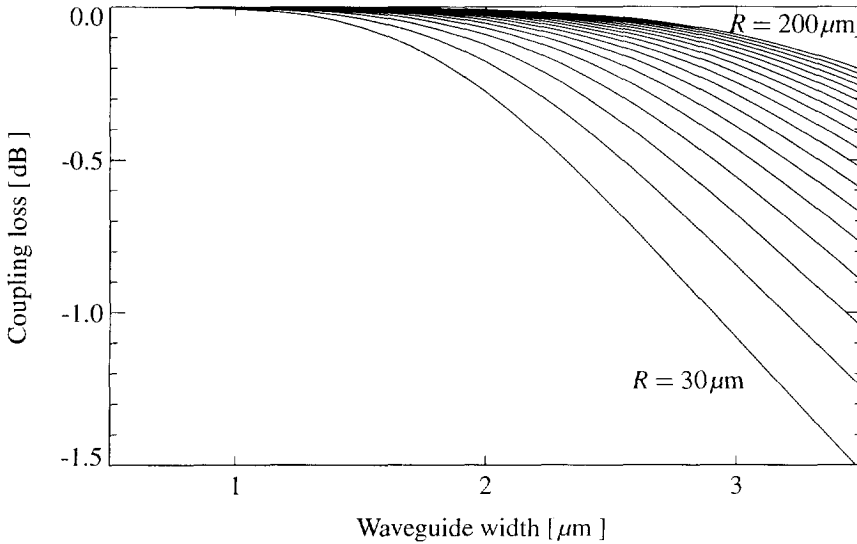


Figure 3.21: Straight-to-bend coupling loss with optimised offset for bending radii of 30 to 200 μm in 10 μm steps, as a function of waveguide width.

The method is based upon the idea that a mode propagating with an effective index below the substrate index, although guided laterally by the high index contrast, would leak into the substrate and be lost. With the conformal transformation technique [20], the effective index in the bend, defined as $N_{\text{eff}} = \text{Re}(\gamma)/k_0R$, with γ the angular propagation constant, is found to decrease with decreasing bending radius R [53], quickly dropping when R becomes smaller than the cutoff radius R_c given by

$$R_c = \frac{wN_{\text{ridge}}}{2(N_{\text{straight}} - n_{\text{substr}})} \quad (3.16)$$

where the effective index becomes equal to the substrate index. A deep-etched waveguide in the layer structure shown in figure 3.20 has an R_c of 26 μm for $w = 1 \mu\text{m}$. The cutoff radius becomes smaller for larger w because N_{straight} in (3.16) increases quickly.

Another factor influencing the range of usable bending radii is the the mode profile, which is not only shifted outward, but also changed in shape. The latter effect can not be cured with an offset. Figure 3.21 shows the straight-to-bend coupling loss (with optimal offset) for different radii and waveguide widths, calculated by overlapping the modal field profiles obtained with the EIM. Clearly, very wide waveguides are not a good choice. This is because the mode will only be guided by the outer waveguide boundary and is not influenced by the inner boundary. Such a mode is known as a “Whispering Gallery Mode” after Lord Rayleigh [54], and has an asymmetric shape, which results in coupling loss with the symmetric mode profile of a straight waveguide. Apparently, in narrower waveguides the influence of the inner boundary yields the mode profile more symmetric, and the coupling loss lower. On the other hand,

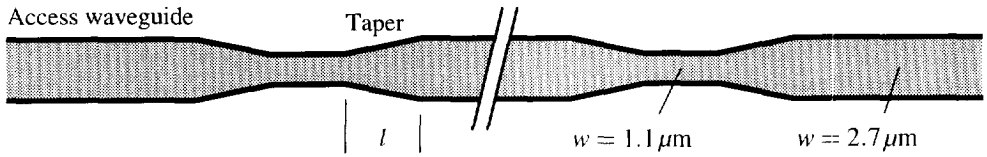


Figure 3.22: Structure used to determine taper loss. Total number of tapers is 10.

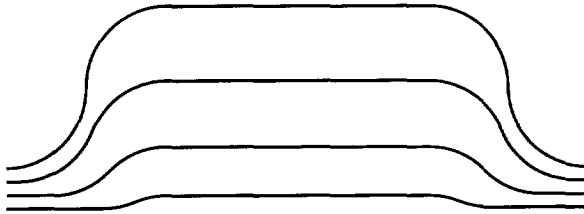


Figure 3.23: Structure used to determine bend loss. Two S-bends are connected by a straight section of 1 mm. Total bending angle is 90, 180, 270, or 360°.

narrow waveguides are not desirable from the perspective of scattering loss (see figure 3.17). Therefore, a compromise has to be found.

3.3.4 Experimental results

A chip was fabricated containing MMI structures (see chapter 4) and bend structures. The available wafer consisted of a SI-InP substrate with MOVPE-grown nominally undoped epitaxial layers: a 660 nm InGaAsP guiding layer with $\lambda_g = 1.3 \mu\text{m}$, and a 320 nm top layer. The thicknesses are slightly larger than the values of 600 and 300 nm, respectively, for which the calculations were done. This leads to a slightly larger index contrast, and a lower cutoff radius.

The waveguides were defined in photo-resist with projection lithography, and transferred into a 140 nm thick RF-sputtered SiO₂ masking layer with CHF₃ reactive ion etching. Subsequently, the chip was etched with the CH₄/H₂ etching/descumming process described earlier. The waveguide losses are plotted in figure 3.17 on page 32 (Δ and \square).

For reasons of waveguide scattering loss, wide access waveguides of $3 \mu\text{m}$ were used, while a width of $1.4 \mu\text{m}$ was chosen for the bend structures, in order to ensure low coupling loss (figure 3.21). Furthermore, at $1.4 \mu\text{m}$ width, deep-etched waveguides in the given layer structure support only a single mode with an effective index above the substrate index. The lithographic process reduced the dimensions to 2.7 and $1.1 \mu\text{m}$, respectively.

To connect these waveguides of different widths, tapers with a length of $50 \mu\text{m}$ were used. Test structures composed of series of 10 tapers configured as shown in figure 3.22 have an excess loss between 0.2 and 0.3 dB with respect to $2.7 \mu\text{m}$ wide straight reference waveguides, for taper lengths of 10, 20, 30, 40, and $50 \mu\text{m}$. It can be concluded that single tapers cause negligible loss.

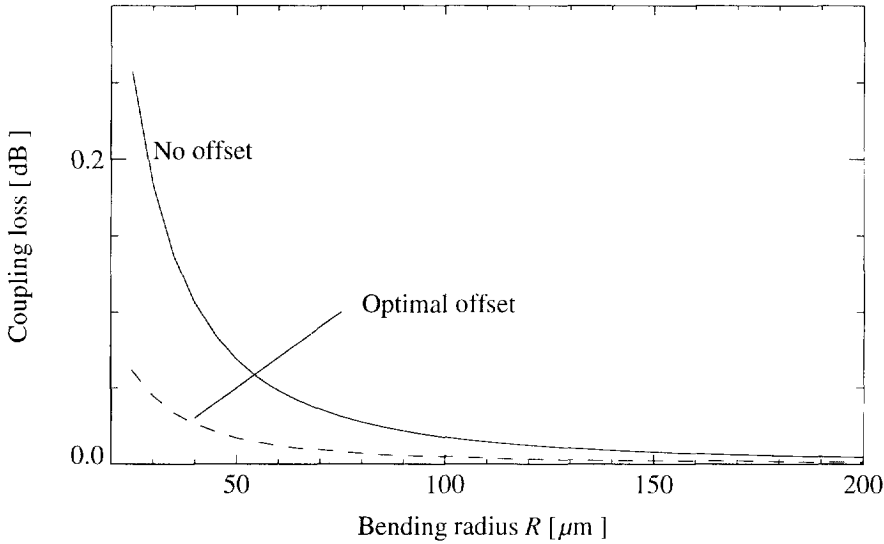


Figure 3.24: Junction loss when optimal offset (dashed) or no offset (solid) is used, for straight-to-bend junctions of $1.4\mu\text{m}$ wide waveguides. The optimal offset varies from $0.01\mu\text{m}$ at $R = 200\mu\text{m}$ to $0.1\mu\text{m}$ at $R = 25\mu\text{m}$.

Curved waveguide test structures consisting of S-bends connected by a straight section of 1 mm were used, as shown in figure 3.23. (The straight section was inserted to solve some technical problems in the production of the waveguide mask. Standard EBPB fractioning software is not very well suited for dealing with many smoothly curved sections in a small area.) Structures with bending radii of 30, 50, 70, and $100\mu\text{m}$ were present, with total bending angles of 90° , 180° , 270° , and 360° . No offsets were used in the straight-to-bend or bend-to-bend junctions. Optimal offsets would have been smaller than $0.1\mu\text{m}$ even for the $30\mu\text{m}$ bends, and coupling loss is low (see figure 3.24).

The excess losses of these structures were measured in transmission, relative to straight waveguides containing a 1 mm long $1.1\mu\text{m}$ wide section, to correct for the straight section inserted between the S-bends. In figure 3.25, the results are plotted with TE polarised light launched into the waveguides. The results for TM are similar.

When the light transmitted through the waveguides was analysed with a polariser, it was discovered that polarisation is not conserved in the deep-etched sharp bends under consideration [55]. The amount of polarisation rotation measured is plotted in figure 3.26. When TE polarised light is input, the percentage of conversion to TM is defined as

$$\text{conversion [\%]} = 100 \cdot \frac{P_{\text{TM}}}{P_{\text{TE}} + P_{\text{TM}}} \quad (3.17)$$

and *vice versa*. It is seen that in bends with a radius of $100\mu\text{m}$, almost no conversion takes place. A maximum conversion of 60% is found at a radius of $50\mu\text{m}$.

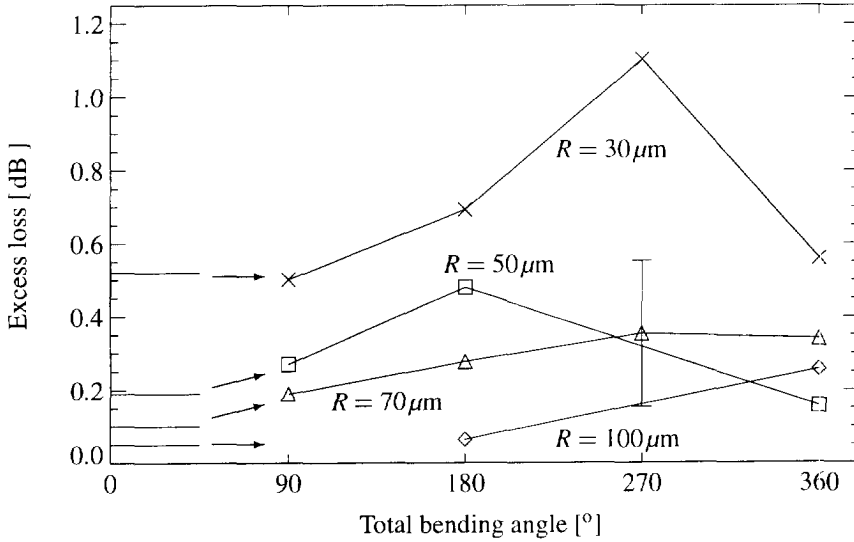


Figure 3.25: Excess loss of structures of figure 3.23 when TE polarised light is input. The estimated measurement error of ± 0.2 dB is indicated. The losses are plotted as a function of the total bending angle traversed by the light. A calculated value for the constant loss contribution of the four straight-to-bend and two bend-to-bend junctions present in the structure is indicated by the straight lines on the left. Bends that had higher losses due to defects have been omitted.

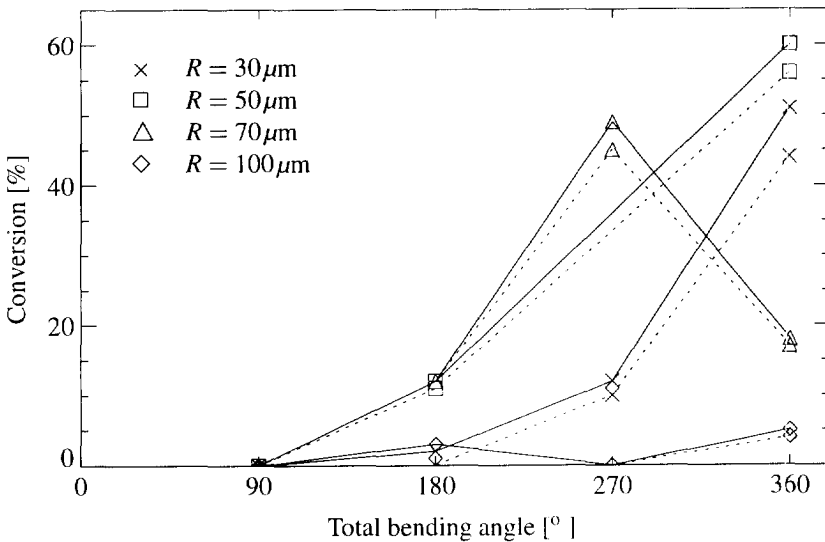


Figure 3.26: Polarisation conversion in bend structures of figure 3.23. Solid lines represent TE to TM conversion; dotted lines represent TM to TE conversion.

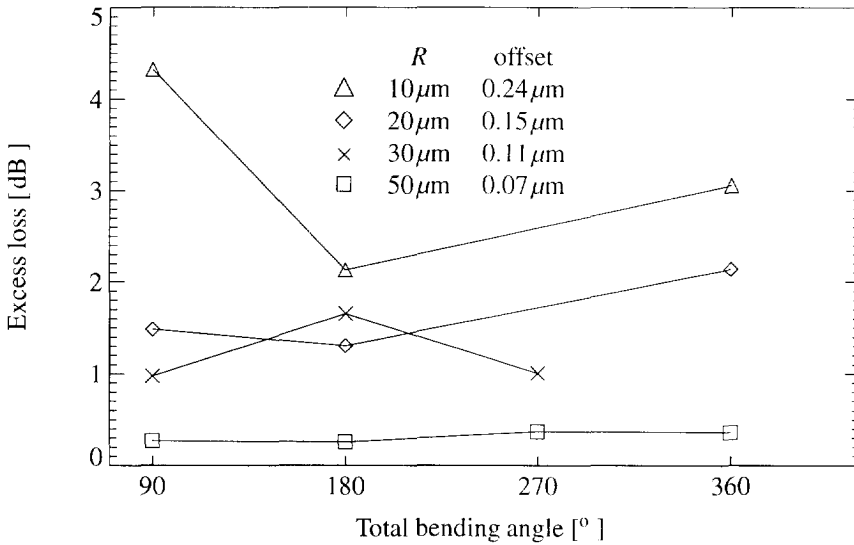


Figure 3.27: Excess loss of U-bends with offsets (the straight-to-bend offsets are given). Input: TE polarised light. The losses are plotted as a function of the total bending angle traversed by the light. The bends with $R = 50\mu\text{m}$ have a comparable loss to those in figure 3.25; the $R = 30\mu\text{m}$ losses are approximately twice as large as those of the bends without offset.

It is believed that the polarisation rotation found in these sharp bends is due to the relatively large non-dominant field components of the modes. At the junctions between different waveguide segments, these non-symmetrical components are excited by the dominant component of the other polarisation. Large rotations can build up when the distance between junctions that have opposite effects is close to the beat length of the TE and TM modes. This explains why conversion is low for the bends in figure 3.26 for which the total bend angle is small: the conversion experienced in one junction is immediately cancelled by the next junction, because no appreciable phase difference has been built up between the polarisations.

The losses in figure 3.25 do not increase monotonically with total bending angle (as would be expected in the presence of a bending loss contribution), but instead experience maxima (such as the 1.1 dB loss for a 270° bend). This can be ascribed to multi-mode (TE and TM) propagation, which yields the junction losses dependent on the coincidental distribution of the light between the polarisations.

A more comprehensive account of polarisation rotation in sharp bends will be given by Van Dam [56].

A second set of bends on a similar chip produced the results shown in figure 3.27. This time, offsets have been used between the waveguide segments. The losses of the $50\mu\text{m}$ bends are about equal to those in figure 3.25, while the losses of the $30\mu\text{m}$ bends are about twice as large. Again no clear increase of loss with bending angle is found. Modal mismatch at the

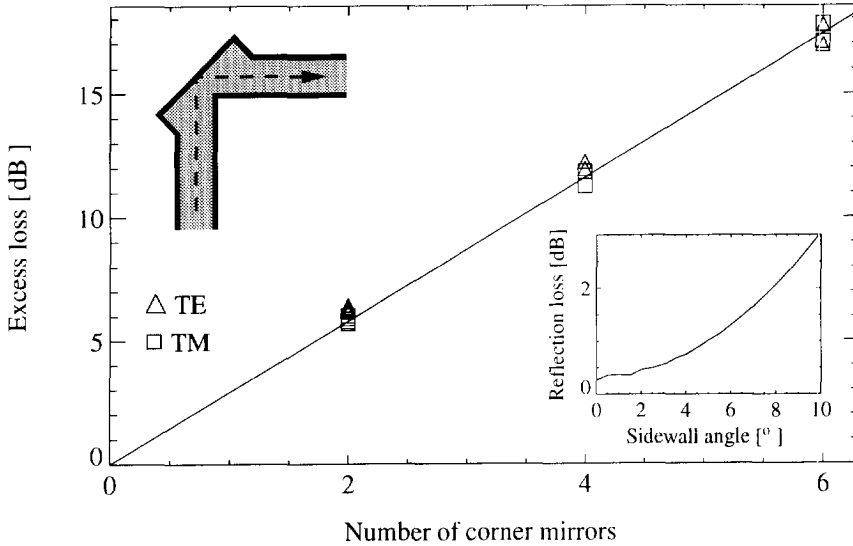


Figure 3.28: Loss of structures consisting of a number of corner mirrors, relative to a straight waveguide. The top left inset shows a top view of one corner mirror. Access waveguides are $3\mu\text{m}$ wide. Loss per mirror is $2.96 \pm 0.04\text{dB}$ for TE and $2.90 \pm 0.02\text{dB}$ for TM. The bottom right inset shows the calculated reflection loss as a function of facet angle.

junctions seems to be the most important loss mechanism.

Summarising, it has been shown that extremely sharp waveguide bends with low loss can be made with deep-etched ridge waveguides. There is no significant increase in loss with increasing total bend angle, indicating that radiation loss and substrate leakage are negligible. Mainly, the loss is due to the constant contribution of the waveguide junctions. For example, the excess loss of the $R = 30\mu\text{m}$ bends without offsets, around 0.6dB , can be explained by this contribution (indicated by the horizontal lines on the left of figure 3.25), which is 0.52dB , as predicted by modal overlap calculations.

A number of corner mirror structures as depicted in figure 3.28 have also been fabricated. A loss per corner mirror of 3dB has been found, both for TE and TM. No special precautions could be taken to ensure a vertical mirror facet, because the mirrors were etched along with the rest of the chip containing the S-bends, in a standard etching/descumming process optimised for low waveguide loss.

In the bottom right inset in figure 3.28, the reflection loss of the corner mirrors used is calculated as a function of facet angle. The calculation has been done by decomposing the modal profile of the incoming wave into its spatial Fourier components, and then separately considering their reflection at the mirror facet. The overlap of the resulting field with the mode in the output waveguide gives the reflection loss [17]. The expected loss at 10° is in accordance with the measured mirror loss. This is about the sidewall angle that was realized.

3.4 Conclusion

In this chapter we have presented a comprehensive study of InP ridge waveguide loss. Surface scattering has been identified as the most important loss mechanism in straight waveguides. A novel reactive ion etching process with oxygen descumming steps has been introduced, which produces waveguides with very low scattering loss.

For medium contrast waveguides (shallow etched, index contrast 0.01...0.03), roughness of the etched surface next to the ridge, as opposed to the ridge sidewall, is the most important factor for scattering loss. For TE polarisation, $1.4\mu\text{m}$ wide waveguides with 1 dB/cm of propagation loss have been measured. For TM polarisation, losses are much higher due to an anomalous non-dominant field component. Deep-etched high contrast waveguides with losses of 6 dB/cm at a width of $1.1\mu\text{m}$, and 0.6 dB/cm at a width of $2.7\mu\text{m}$, for both polarisations, have been fabricated.

Deep-etched waveguide bends, i.e., with the maximum possible lateral index contrast, have been made with negligible radiation loss and low overall loss down to bending radii of $30\mu\text{m}$. The most important loss factor for ultra-sharp bends has been shown to be the loss at junctions between waveguide segments of different curvature. This is caused by the asymmetry introduced in the modal field profile. Another problem is the increased non-dominant field component, which causes polarisation conversion at the junctions. This problem is avoided by choosing larger bending radii ($R \geq 100\mu\text{m}$), and does no harm in short bend sections. In comparison with corner mirrors, ultra-sharp deep-etched bends offer strongly reduced loss for only slightly larger use of chip area.

The concepts discussed in this chapter, of deep-etched waveguides, bends, and tapers, will be used extensively in the chapter on miniaturised MMI couplers (chapter 4).

3.A Appendix: Derivation of reflection formula (3.9)

In trying to formulate a criterion from which one can decide when specular reflection becomes diffuse scattering, i.e., when one should call a surface smooth, and when one should call it rough, Rayleigh suggested the following way to relate this problem to a number of relevant parameters.

Consider a surface with step irregularities of height h , and two rays incident upon it at an angle θ with the normal (figure 3.29). The phase difference between the two reflected rays due to the step is

$$\Delta\phi = \frac{2\pi}{\lambda} 2h \cos\theta = 2k_x h, \quad (3.18)$$

with k_x the wave number in the direction normal to the surface. If $\Delta\phi$ is small, the two rays are almost in phase, like they would be when reflecting from a perfectly flat surface. If the phase difference increases, the rays interfere, until they totally cancel for $\Delta\phi = \pi$. The power that is not going in the direction of specular reflection due to this interference, is distributed in other directions because of conservation of energy. Rayleigh chose a value of $\Delta\phi$ halfway between these two extremes: a surface is considered smooth when $h < \frac{\pi}{4k_x}$.

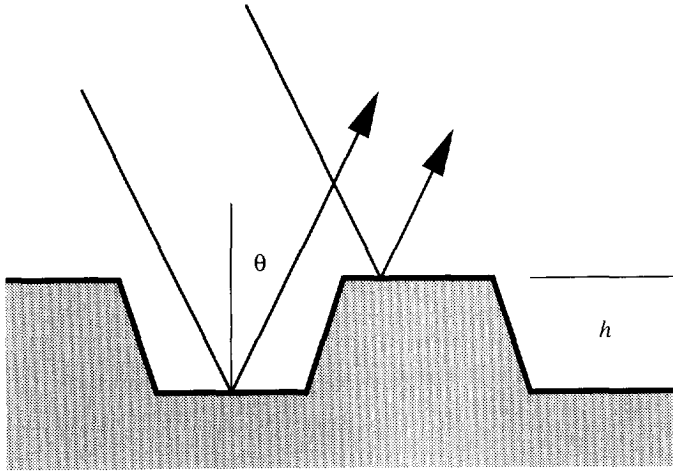


Figure 3.29: Two rays incident on a rough surface.

This argument can easily be quantified with a simple physical argument. The fraction of incident power going in the direction of specular reflection is, for two rays,

$$\mathcal{R} = \left| \underbrace{\frac{1}{2} e^{i\phi_0}}_{\text{ray 1}} + \underbrace{\frac{1}{2} e^{i(\phi_0 + \Delta\theta)}}_{\text{ray 2}} \right|^2. \quad (3.19)$$

When the distribution function $w(x)$ of the position of the interface around its mean is given, and an infinite number of rays is considered, this can be written as

$$\mathcal{R} = \left| \int_{-\infty}^{\infty} w(x) e^{2ik_r x} dx \right|^2. \quad (3.20)$$

If $w(x)$ is assumed to be a Gaussian distribution with a standard deviation σ , the integral becomes

$$\frac{1}{\sqrt{2\pi}\sigma} \int e^{-\frac{x^2}{2\sigma^2}} e^{2ik_r x} dx, \quad (3.21)$$

which, after a change of integration variable $x = \sqrt{2}\sigma y$, can be written

$$\frac{1}{\sqrt{\pi}} \int e^{-y^2} e^{2\sqrt{2}i\sigma k_r y} dy. \quad (3.22)$$

With the substitution $b = \sqrt{2}i\sigma k_r$ and another change of integration variable $y = z + b$, the integral becomes

$$\frac{e^{b^2}}{\sqrt{\pi}} \int e^{-z^2} dz. \quad (3.23)$$

Because $\int_{-\infty}^{\infty} e^{-z^2} dz$ is a well-known integral with value $\sqrt{\pi}$, we find

$$\mathcal{R} = |e^{h^2}|^2 = e^{-(2\sigma k_v)^2}, \quad (3.24)$$

which is the sought result (3.9).

3.B E -dependence of scattering loss

For a slab waveguide, E is constant in the plane of each of its interfaces, and for the scattering loss a simple proportionality with the field intensity E^2 at these interfaces is found. In the case of two dimensional confinement, matters are not that simple. Generally E varies appreciably in the plane of, e.g., a rough sidewall. Deri *et al.* have found the expression (3.13) for the scattering loss in this case, i.e., the loss is proportional to the integral of E^2 over the part of the interface under consideration.

In contrast with this result, Hewson-Browne *et al.* have found [37] that substrate radiation loss can be described with

$$\alpha_{\text{subs}} = \frac{a^2 \Delta n^2 C^2}{4\beta} \left(\int_{\text{sidewall}} E dx \right)^2 \quad (3.25)$$

with a the amplitude of the roughness, and C a parameter related to its spatial period. On comparison, the main difference with (3.13) is that the square of the integral is taken, instead of the integral of the square. The authors reason that the far field of E depends on the value of $\int E dx$ locally.

In order to be able to evaluate this argument, consider the following thought experiment, which is completely analogous to Young's famous double-slit interference experiment: Instead of a distribution of dipole radiators on a waveguide interface, we take a simplified configuration with only two radiators (or two slits in a plane illuminated from the back) at a distance d (see figure 3.30).

Let $E_1(x)$ and $E_2(x)$ denote the fields from each of the radiators separately, measured in the detector plane at distance D from the radiators. Each of these fields is proportional to the field strength at its radiative source, and it has a phase factor due to the distance D_i to its source. The intensity in the detector plane is $I(x) = (E_1(x) + E_2(x))^2$. The integration in (3.25) has been replaced by a "+"-sign, because we are only considering two radiators. With $D \gg d$ and $|x| \ll D$, and taking the phase factors into account, we find

$$I(x) = 4I_0(x) \cos^2 \left(\frac{\pi d}{D\lambda} x \right), \quad (3.26)$$

with $I_0(x) = E_1(x)^2 = E_2(x)^2$ the intensity that would be measured if only one of the two radiators would have been present. (It is assumed that $I_0(x)$ varies only slowly.) But the total intensity $\int I(x) dx$ is just equal to $2 \int I_0(x) dx$. So even though the power in the detector plane may be denoted by

$$P = \int (\sum E_i)^2 dx, \quad (3.27)$$

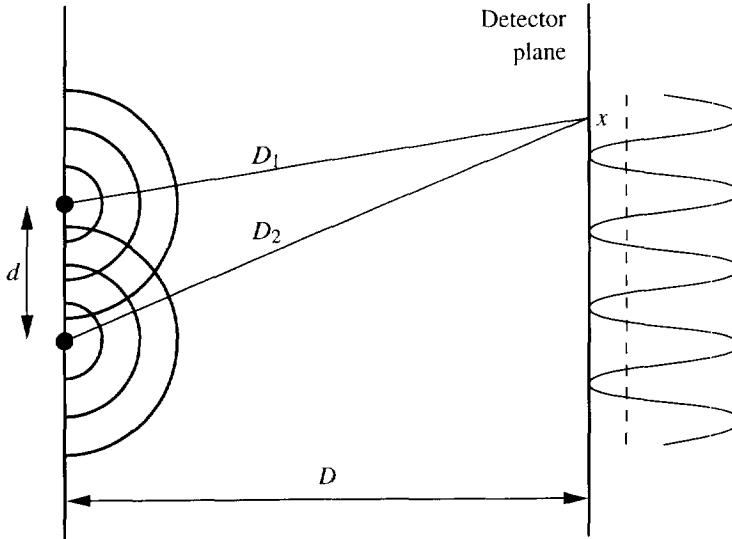


Figure 3.30: The interference pattern of two radiators. The dashed line indicates the power distribution in the detector plane when only one radiator is present.

(where the correct phase factors in $E_i(x)$ describing the distance D_i from the source must be used!), this is equivalent to

$$P = \int \sum |E_i|^2 dx = \sum_i \left(\int |E_i|^2 dx \right), \quad (3.28)$$

where the E_i are directly proportional to the field strengths at the sources. When the two radiators are again replaced by a distribution, and the summation in (3.28) is replaced by an integral sign, we arrive at the integral of the square of the field, as opposed to the square of the integral.

The reason the latter is found in [37] is because in that calculation the problem of sidewall scattering is converted from a distribution of sources across the sidewall each in a field $E(x)$, into a form with a single source at the bottom of the sidewall in a field $\int E dx$, and the radiation loss is determined as the radiation loss of this single source; i.e., the integration is done in the near field instead of in the far field.

Chapter 4

Miniaturisation and tolerance analysis of multi-mode interference couplers

Couplers are important elements of optical networks. The so-called multi-mode interference coupler has important advantages over traditional directional couplers in terms of fabrication tolerance. Its operation, based on the self-imaging effect in multi-mode waveguides, is described with modal propagation analysis.

In order to miniaturise MMI couplers, devices have been fabricated in a deep-etched ridge waveguide structure, which resulted in the smallest low loss MMI couplers to date. By varying the width of the input waveguides, it is shown that the width tolerance of MMI devices becomes better when the input field is made wider. The good crosstalk of passive MZI structures shows that the phase transfer of the constituent MMI 3 dB couplers is as expected.

4.1 Introduction

All optical communication systems other than the simplest point-to-point connections involve more than just fibres or other waveguides. In a broadcast system, for instance, where one signal source serves multiple receivers, a splitter is needed that distributes the signal power (see figure 4.1(a)). And when waveguides are used in interferometric configurations, as in figures 4.1(b) and 4.1(c), the signal has to be split up and combined. In general, the couplers providing this functionality are important components in an optical network.

An optical coupler can be fabricated in planar optical components by bringing two waveguides close together (figure 4.2). Optical power will be able to “tunnel” from one waveguide to the other, the fraction of power transferred depending strongly on the distance of the waveguides and the confinement of the fields in the cores. Therefore, tolerance requirements for the

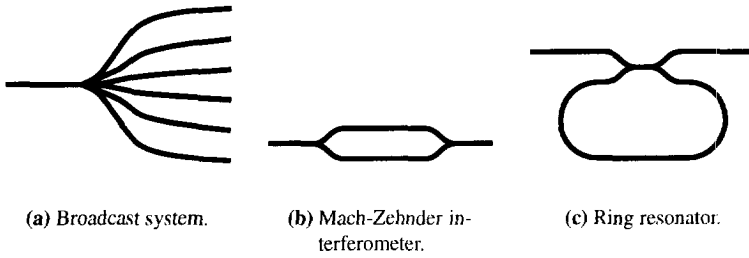


Figure 4.1: Examples of the use of optical couplers.

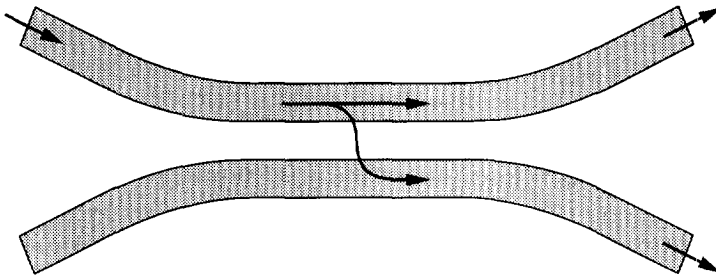


Figure 4.2: A directional coupler, lithographically defined in planar waveguides. The fraction of power coupled to the other waveguide depends heavily on the waveguide distance and the etch depth.

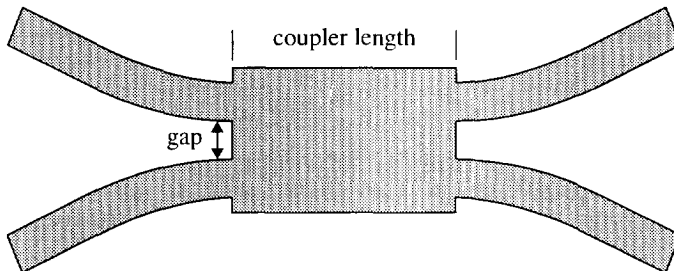


Figure 4.3: A multi-mode interference coupler. Its operation is based on the self-imaging effect (see section 4.2). The coupling is almost independent of the etching depth. The most critical parameter is the width of the multi-mode section.

fabrication process are extremely strict. Both the lithographic line-width and the etch depth must be very well controlled. In addition, the contribution of the curved connecting waveguides to the coupling must be included in the analysis.

A different approach is the application of couplers based on the self-imaging effect in multi-mode waveguides [57, 58]. In these couplers, the parallel waveguides and the gap are replaced by a wide multi-mode waveguide (see figure 4.3), and the coupling takes place as a result of the images of the input field that are formed onto the output waveguides. This mechanism will be explained in section 4.2.

The gap between the access waveguides of an MMI coupler can be chosen large enough so that they are (for practical purposes) completely decoupled. The self-imaging mechanism in the multi-mode section is almost independent of the etching depth, making the MMI a very fabrication tolerant component. This has made MMI couplers very popular devices. At present, they are being used on a large scale in, among other things, interferometric switches [59–62], modulators [63], ring lasers [64–66], and mixers for coherent detection [67, 68].

The interest in these components has brought about much attention in the literature for their properties, e.g., regarding self-imaging and phase relations [69], and bandwidth and fabrication tolerances [70]. Because the size of components is becoming increasingly important, e.g., for switches in large switching fabrics [71], miniaturisation of MMI couplers has raised a lot of interest [72–76]. At the moment, the world's smallest MMI 3 dB coupler is $4 \times 40 \mu\text{m}$, exhibiting an insertion loss of 4.3 dB [74]. The smallest low loss coupler is a device of $4.5 \times 90 \mu\text{m}$, with an insertion loss of 0.7 dB [76].

In this chapter, after a brief overview of the mechanism of operation of MMI couplers, it will be shown in section 4.3.1 that the deep-etching technique developed in chapter 3 can be used to fabricate ultra-small MMI couplers. This is possible, essentially, because the strong confinement in the waveguides provides a large number of guided modes even in small MMI sections. The result found in [70] that smaller MMI couplers require tighter fabrication tolerances is verified experimentally for these deep-etched couplers in section 4.3.2.

4.2 Multi-mode interference and self-imaging

The operation of MMI couplers is based on the self-imaging effect, as occurring in a multi-mode waveguide. Bryngdahl was the first to suggest that formation of images could take place in a multi-mode waveguide [77]. The formation of multiple self-images in a slab waveguide was described ray-optically and experimentally demonstrated by Ulrich [78].

4.2.1 Modal propagation analysis

Modal propagation analysis (MPA) is the simulation method providing the most insight in the operation of devices based on self-imaging in waveguides [79]. This method decomposes a field entering a multi-mode section into the modes supported by the section, individually propagates them, and adds them at the end of the section where the resulting field is coupled to the output waveguides (hence the name *multi-mode interference*).

With the *Dirac notation* and *Einstein's summation convention* (see appendix 4.A), the spectral decomposition of a normalised input field $|\phi\rangle$ into the modes $|\psi_n\rangle$ of a multi-mode section is given by

$$|\phi\rangle = c_n |\psi_n\rangle. \quad (4.1)$$

Using the closure relation $|\psi_n\rangle\langle\psi_n| = I$, the modal excitation coefficients c_n are found to be the overlap integrals $\langle\psi_n | \phi\rangle$:

$$|\phi\rangle = I|\phi\rangle = |\psi_n\rangle\langle\psi_n | \phi\rangle. \quad (4.2)$$

In a well-designed MMI coupler, nearly all the incident power is coupled into guided modes, so the radiation part of the modal decomposition is usually ignored in the MPA.

The modes ψ_n propagate through the multi-mode waveguide with propagation constants β_n . For the field $\phi(z)$ at a distance z from the input we obtain

$$|\phi(z)\rangle = e^{-i\beta_n z} |\psi_n\rangle\langle\psi_n | \phi\rangle, \quad (4.3)$$

and the coupling efficiency to a field ξ (e.g., the modal field of an output waveguide) is

$$\langle\xi|e^{-i\beta_n z}|\psi_n\rangle\langle\psi_n | \phi\rangle. \quad (4.4)$$

The propagation constants β_n are related to the wave number k ($=k_0 n_r$, with n_r the effective index of the guiding region) and the lateral wave numbers $k_{y,n}$ through the equation

$$k_{y,n}^2 + \beta_n^2 = k^2. \quad (4.5)$$

When the multi-mode waveguide is infinitely guiding, i.e., it provides infinite confinement, the mode profiles ψ_n are cosine profiles with n nodes, and

$$k_{y,n} = \frac{(n+1)\pi}{W} \quad (4.6)$$

with W the width of the multi-mode waveguide. For physical waveguides, (4.6) is not exact, but for high contrast waveguides it is a good approximation. With equation (4.5) and $k_{y,n}^2 \ll k^2$, we find

$$\beta_n = k - \frac{(n+1)^2 \pi}{4n_r W^2 / \lambda_0}, \quad (4.7)$$

and the propagation constant spacing is

$$\beta_0 - \beta_n = \frac{n(n+2)\pi}{4n_r W^2 / \lambda_0} = \frac{n(n+2)\pi}{3L_\pi}, \quad (4.8)$$

when we define $L_\pi \equiv \pi/(\beta_0 - \beta_1) = 4n_r W^2 / 3\lambda_0$, the beat length between the two lowest order modes.

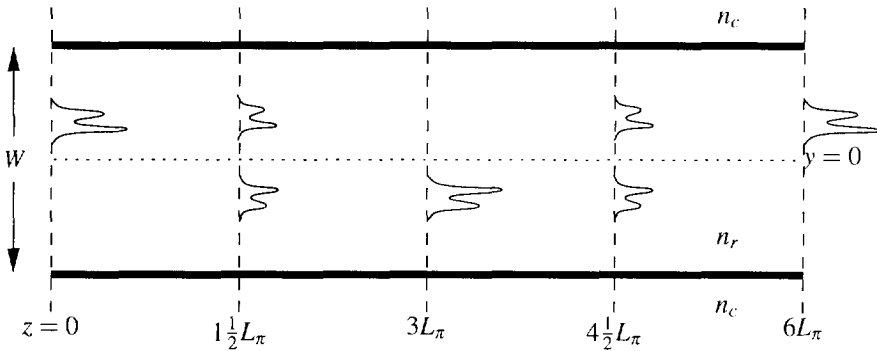


Figure 4.4: Self-imaging in a multi-mode waveguide. Shown are direct, mirrored, and two-fold images.

4.2.2 Image formation

When we take a phase contribution $e^{-i\beta_0 z}$ outside the summation in (4.3), the remaining phase difference

$$e^{i(\beta_0 - \beta_n)z} = e^{i\pi n(n+2)z/3L_\pi} \quad (4.9)$$

takes on a particularly simple form for certain values of z . For instance, at $z = 6L_\pi$, it is 1 for all n , so $|\phi(6L_\pi)\rangle$ is a direct image of $|\phi(0)\rangle$ (hence the name *self-imaging effect*). Of course this is only true under the assumption that (4.6) is valid. For small aberrations, a small correction to the theoretical imaging length $6L_\pi$ will give better results [80].

When $z = 3L_\pi$, (4.9) is 1 for even modes, and -1 for odd modes. This means that the image $|\phi(3L_\pi)\rangle$ is a mirror image of the input field with respect to the middle of the multi-mode waveguide (see figure 4.4). At $z = \frac{1}{2}L_\pi$, the even and odd modes are exactly 90° out of phase, so a direct *and* a mirror image will be formed, each containing half the power of the original field, and having 90° phase difference. In general, it has been shown that N images can be found at distances $\frac{3M}{N}L_\pi$, with M an integer [69].

It has also been shown that some special cases of multi-mode interference exist, that allow for shorter image lengths. These cases depend on the absence of certain modes from the modal spectrum excited by the input field. When every third mode (i.e., $n = 2, 5, 8, \dots$) is absent, the images occur at distances three times shorter [57]. This configuration is called *paired interference*, because the mode pairs 0-1, 3-4, 6-7, ... provide increasing orders of symmetric and antisymmetric functions for the decomposition of the input field [79]. It can be obtained by exciting the multi-mode waveguide with a symmetric input field at a $y = \pm W/6$, because there the profiles of the modes 2, 5, 8, ... change sign.

Another special case is one where the multi-mode waveguide is excited symmetrically, i.e., with a centred symmetric field distribution [73]. Now only even modes will be excited in the multi-mode section, and N images will appear at an image distance of $\frac{3M}{4N}L_\pi$. In table 4.1, a summary is given (taken from [58]) of the properties of all cases discussed.

Interference mechanism	<i>General</i>	<i>Paired</i>	<i>Symmetric</i>
Inputs \times outputs	$N \times N$	$2 \times N$	$1 \times N$
First N -fold image distance	$\frac{3L_\pi}{N}$	$\frac{L_\pi}{N}$	$\frac{3L_\pi}{4N}$
Excitation requirements	none	Exclude 2,5,8,...	Only symmetric modes
Input field	any	$y = \pm W/6$	$y = 0$

Table 4.1: Summary of the properties of the various cases of self-imaging discussed in paragraph 4.2.2.

It has been seen that MMI couplers can be made in various splitting and combining configurations. The devices are not very sensitive to variations in the etching depth, because these hardly affect the propagation constant spacings $\beta_0 - \beta_n$ [81]. The same argument goes for the polarisation dependence of the devices. Furthermore, the balance between the outputs of MMI splitters is inherently better than that of traditional couplers, because the sensitivity of the transmission to a length variation is at a minimum for the optimum design length of an MMI device, while it is at a maximum for the traditional coupler. The drawback that MMI couplers can only split power in equal parts has been removed by the appearance of MMI couplers with free selection of power splitting ratios [82].

Unlike conventional directional couplers, MMI devices are zero-gap structures, which leads to large $\Delta\beta$ s and, consequently, very compact devices. MMI devices are also compatible with deep-etched structures, which would give problems with very small gaps in traditional directional couplers [83]. Thus, MMI couplers are a process tolerant and compact alternative for conventional directional couplers.

4.2.3 Performance of MMI couplers

For N -way splitters, the relevant quantities for describing the performance are the excess loss and the balance between the outputs. (For 3 dB couplers, the phase difference between the outputs is also of relevance.) For cross couplers, the important values are the excess loss and the crosstalk.

The excess loss of a splitter is defined as

$$\text{Loss [dB]} \equiv -10 \log \sum_n \frac{P_n}{P_{\text{ref}}}, \quad (4.10)$$

where P_n is the power measured at output n , and P_{ref} is a reference power, usually, the transmission through a straight waveguide. The balance between outputs m and n is defined as

$$\text{Balance}_{m,n} \text{ [dB]} \equiv -10 \log \frac{P_m}{P_n}. \quad (4.11)$$

For a 2×2 cross coupler, the excess loss is defined as

$$\text{Loss [dB]} \equiv -10 \log \frac{P_{\text{cross}}}{P_{\text{ref}}}, \quad (4.12)$$

and the crosstalk is defined as

$$\text{Crosstalk [dB]} \equiv -10 \log \frac{P_{\text{bar}}}{P_{\text{cross}}}. \quad (4.13)$$

with P_{cross} and P_{bar} the power emerging from respectively the cross and bar outputs, as defined in figure 4.5. Thus, an MMI coupler is characterised by measuring the power transmitted to all its outputs, relative to the power transmitted by a straight reference waveguide.

In an ideal N -way splitter, N perfect images, each carrying a fraction of $1/N$ of the input power, will be projected onto the output waveguides, so the loss (4.10) will be 0dB, as will the balances (4.11). Due to the finite image resolution in physical MMI splitters, some loss will be incurred. When the dimensions of the MMI coupler deviate from the design dimensions, e.g., due to fabrication variations, the images will be slightly out of focus, leading to additional loss. Because in first order approximation the loss will increase equally for all outputs, the balance will stay good over an appreciable range of variations.

What was said above about the loss of splitters also holds for cross couplers. As crosstalk is concerned, it would be absent in ideal cross couplers, because all power would be imaged onto the cross output with infinite accuracy. For physical cross couplers, however, the finite accuracy with which the mode spectrum is constructed will not leave the area in front of the bar output absolutely dark, so there will be some crosstalk, which can be used besides the loss as a measure of the imaging accuracy. In the presence of fabrication variations, part of the power in the out-of-focus image projected onto the cross output will be coupled into the bar output, rapidly increasing the crosstalk.

Measuring the parameters (4.10)–(4.13) for varying dimensions (i.e., length or width) of an MMI coupler provides information about the optimum performance of the devices measured, as well as about their fabrication tolerance. This method will be used for a number of devices as described in the following section to assess the limits of MMI coupler miniaturisation.

4.3 Experimental results

Experiments have been performed with two chips produced with a nominally identical fabrication process, as outlined in section 3.3.4. The deep-etched waveguide structure provides for strong lateral confinement of the modes, which makes (4.6) nearly exact, and results in a large number of guided modes even for very small MMI sections. This allows a proper decomposition of the input field to be made in ultra-compact devices.

In section 4.3.1, ultra-small 2×2 splitters and cross couplers are described that illustrate the miniaturisation potential of the deep-etched waveguide structure used. As an example of a device that needs a very large number of guided modes to operate properly, a 1×16 splitter is presented. In section 4.3.2, measurements of MMI couplers of different size demonstrate that there is a trade-off between the degree of miniaturisation of an MMI device and its fabrication tolerance.

All measurements have been performed by launching linearly TE or TM polarised light with a wavelength of 1508nm into the devices, and taking the transmission relative to the transmission of straight reference waveguides.

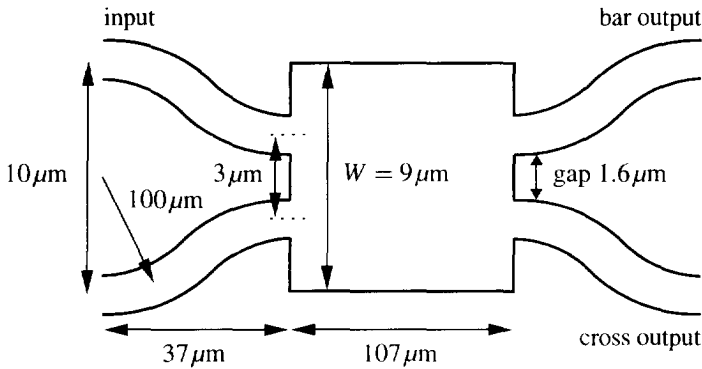


Figure 4.5: Layout of multi-mode interference 3 dB coupler. A cross coupler is similar, only twice as long. The dimensions are design dimensions. The line-widths on chip have been reduced by approximately $0.3\mu\text{m}$ in lithography.

4.3.1 Miniaturised MMI couplers

Cross and 3 dB couplers were designed with a layout as given in figure 4.5 [75]. They are constructed to operate in the paired interference regime (see table 4.1), so the access waveguides are connected at $1/3$ and $2/3$ of the MMI width. In this regime, the shortest couplers can be made with only moderately small widths, so any problems with the number of guided modes is avoided. The width was chosen such that a reasonable gap was kept between the access waveguides, to avoid problems with lithography. The MMI section of the fabricated devices is about $8.7\mu\text{m}$ wide. In the deep-etched structure, this yields a L_π of around $220\mu\text{m}$. There are 11 guided modes, so the paired interference occurs for modes 0-1, 3-4, 6-7, and 9-10.

S-bends having radii of $100\mu\text{m}$ are used to fan out the access waveguides to a distance of $10\mu\text{m}$, which is just resolvable by the pinhole in the transmission measurement setup. The bends are $1.1\mu\text{m}$ wide. This ensures monomode behaviour and low coupling loss (see section 3.3.4). $50\mu\text{m}$ long tapers are used to connect straight $2.7\mu\text{m}$ wide waveguides to the S-bends. Straight reference waveguides with a $1.1\mu\text{m}$ wide section as long as MMI plus bends are present for measurement of relative transmission.

In figure 4.6, measurement results are plotted for 3 dB couplers varying in length from 98 to $120\mu\text{m}$. The good balance of the devices over a large range of length is evident. It can also be seen that the length tolerance is so tight that a penalty is incurred for polarisation independent behaviour. Figure 4.7 shows the same data plotted in terms of excess loss and balance. For TE polarisation, the best device is the one $107\mu\text{m}$ long, with 0.9 dB excess loss and an unbalance of -0.2dB . For TM, the best device is $111\mu\text{m}$ long, with a loss of 0.7 dB, and 0.03 dB unbalance. (The balance is taken positive if the cross output carries more power.) The best polarisation independent behaviour is observed for the $108\mu\text{m}$ long coupler, with excess losses of 1.5 and 1.2 dB for TE and TM, respectively, and a balance within $\pm 0.3\text{dB}$. It is seen that ultra-small MMI 3 dB couplers can be made with low loss and good balance. In fact, these are the smallest

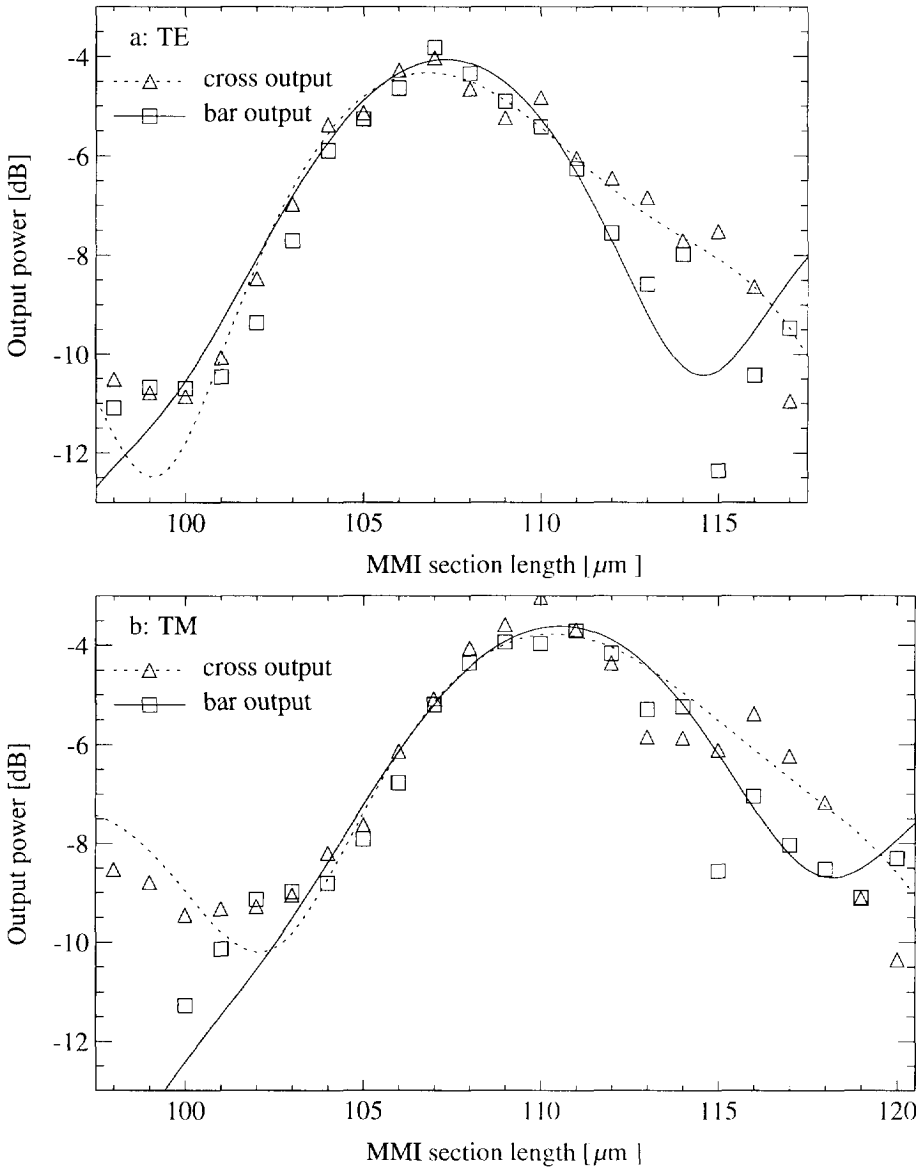


Figure 4.6: Transmission of the two output ports of MMI 3dB couplers under excitation of one of the inputs. The output power relative to the transmission of straight reference waveguides is plotted. \square : power from bar port; solid line: MPA simulation. \triangle : power from cross port; dotted line: MPA simulation. The top graph displays the results for TE polarisation; the bottom graph does the same for TM.

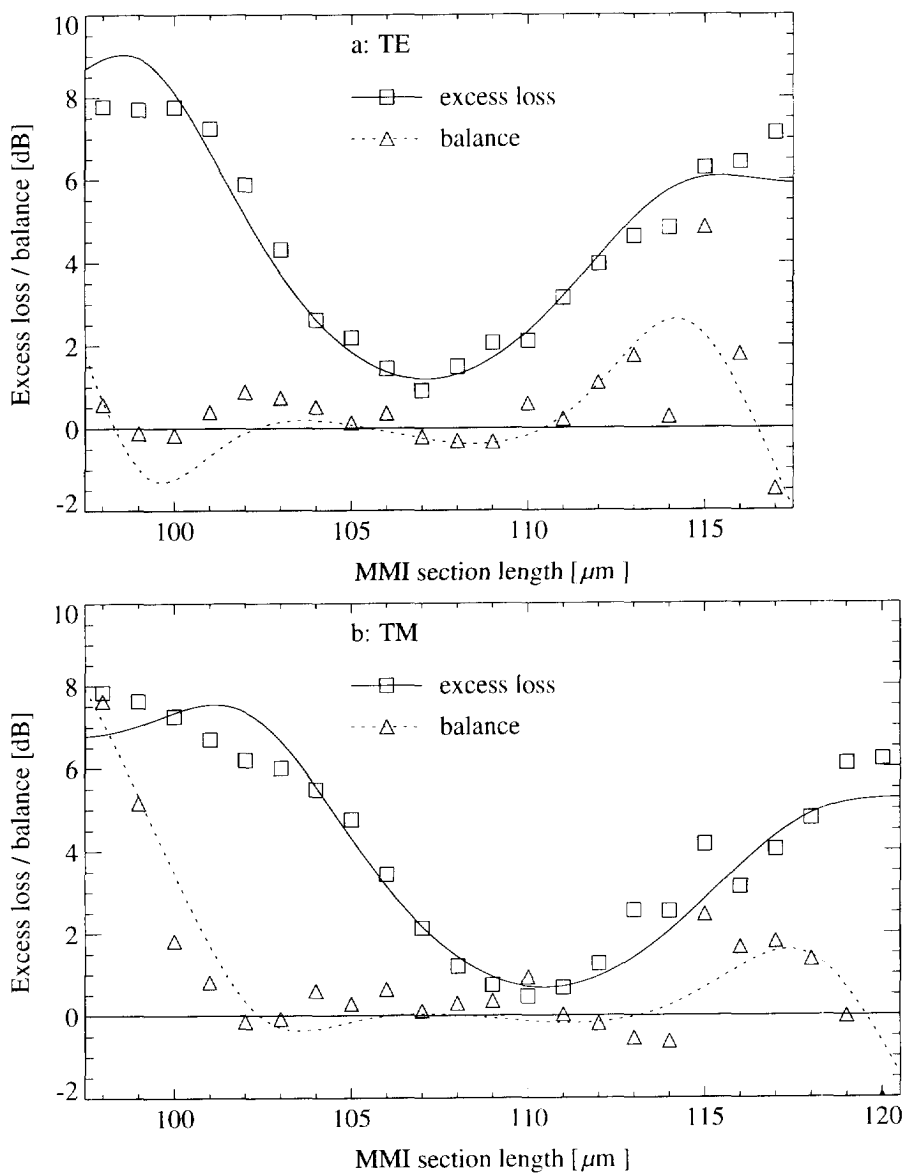


Figure 4.7: The same data as in figure 4.6, plotted as excess loss and balance, according to the definitions of (4.10) and (4.11). \square : excess loss; solid line: MPA simulation. \triangle : balance; dotted line: MPA simulation. The top graph displays the results for TE polarisation; the bottom graph does the same for TM.

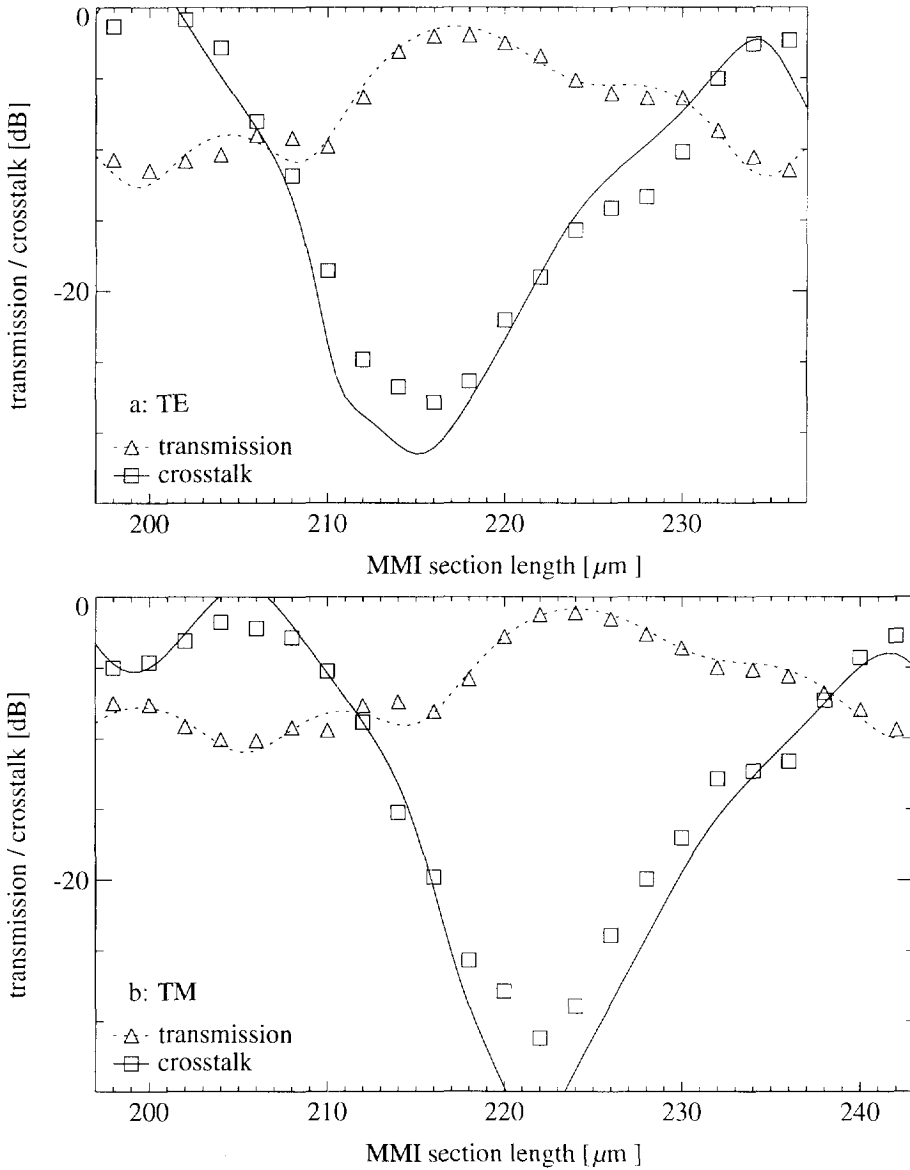


Figure 4.8: Operation of MMI cross couplers under excitation of one of the inputs. Plotted are (—) excess loss (Δ ; dotted line: MPA simulation) and crosstalk (\square ; solid line: MPA simulation), according to the definitions of (4.12) and (4.13). The top graph displays the results for TE polarisation; the bottom graph does the same for TM.

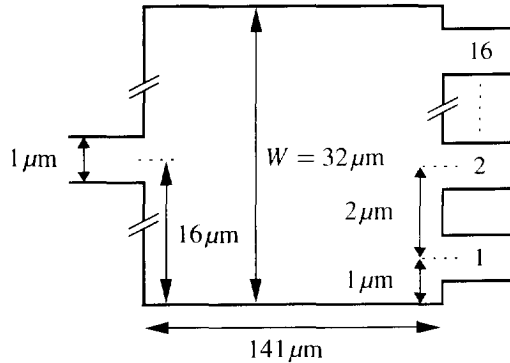


Figure 4.9: Layout of multi-mode interference 1×16 splitter. Design dimensions are indicated. S-bends (not shown) with radii of 50 to $190 \mu\text{m}$ have been used to fan out the 16 outputs to a pitch of $13 \mu\text{m}$.

low loss 3 dB couplers made to date.

Figure 4.8 shows results of measuring cross couplers of lengths $198\text{--}242 \mu\text{m}$. The best device for TE ($216 \mu\text{m}$) has an excess loss of 2.0 dB and a crosstalk of $-27.8 \mu\text{m}$. For TM, the best device ($222 \mu\text{m}$) has an excess loss of 1.2 dB and a crosstalk of $-31.2 \mu\text{m}$. At $220 \mu\text{m}$, excess loss is below 2.8 dB and the crosstalk is better than $-22.1 \mu\text{m}$, independent of polarisation. The low crosstalk indicates that the imaging mechanism works as expected, projecting almost all power onto the cross output and leaving the area in front of the bar output waveguides almost dark.

The lines in the figures 4.6, 4.7, and 4.8 are MPA simulations of the device performance. Two parameters have been varied to obtain the best fit: the MMI width, which influences the position in the graphs of the performance peaks, and the access waveguide width, which influences the width of the performance peaks and the absolute value of the excess loss (i.e., the vertical position of the trace). The best values are $8.6 \mu\text{m}$ for the MMI width (design width: $9 \mu\text{m}$), and $1.06 \mu\text{m}$ for the access waveguide width (design width: $1.4 \mu\text{m}$). These are in good agreement with the $0.3 \mu\text{m}$ lithographic linewidth reduction observed on scanning electron micrographs.

Figure 4.9 is a schematic layout of a symmetric 1×16 splitter. This device needs at least 17 even modes for low loss and well balanced operation [80]. This means that a total of 35 modes need to be guided by the multi-mode section. This is therefore an excellent device for determining if small deep-etched MMI sections provide sufficient confinement.

In order for the device to be as small as possible, both the access waveguides and the gaps have been chosen to be $1 \mu\text{m}$ wide, which leads to an MMI width of $32 \mu\text{m}$. From (4.8) (with $n_r = 3.32$, determined by the effective index method) and table 4.1, it follows that the device length should be $141 \mu\text{m}$.

In figure 4.10, the transmission of each of the 16 paths through the splitter is plotted, relative to the transmission of a reference waveguide. A loss of 1–3.5 dB on top of the expected

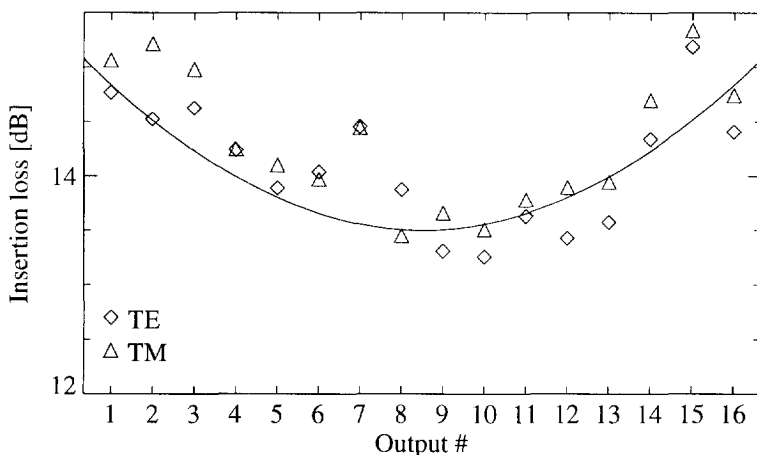


Figure 4.10: Insertion loss for 1×16 MMI splitter. The expected loss for 16 way splitting is 12 dB. The insertion loss of the outputs varies from 1 to 3.5 dB above this value. Line: Loss calculated by overlapping output self-images with output waveguide mode profiles under the assumption that a lithographic width variation of $0.4 \mu\text{m}$ has taken place.

splitting loss of 12 dB is found. The excess loss according to the definition of (4.10) is 2.0 and 2.2 dB (TE, TM), and the worst unbalance according to (4.11) is 1.9 dB.

When a lithographic reduction or expansion of the dimensions will have occurred, the 16 self-images produced at the end of the MMI section will have moved towards or away from the lateral axis of symmetry of the MMI proportionally, creating a mismatch with the output waveguide locations. This gives an offset loss contribution on top of the imaging loss, which is larger for exits further away from the axis of symmetry. The line in figure 4.10 is the theoretical loss expected for an assumed average imaging loss of 1.5 dB, and a dimension reduction or expansion of $0.4 \mu\text{m}$. The unbalance created in this way can be avoided by either increasing the linewidth accuracy of the technology, or by making the waveguides, and consequently the entire MMI, wider, as this will decrease the loss incurred by a lateral offset.

The devices have reasonably low loss (< 3 dB, the minimum loss that would be expected of a diffractive coupler with a waveguide/gap width ratio of 1), and the unbalance can be explained by a dimension variation consistent with the variation found in other devices on the same chip. It must be concluded that the self-imaging mechanism does its work as expected, and that apparently a sufficiently large number of guided modes are present to make this possible.

4.3.2 Tolerance analysis

In section 4.3.1, the performance of MMI cross and 3 dB couplers has been studied by varying the length of the devices. Loss, balance and crosstalk values have been found for the optimal devices, as well as for longer and shorter devices, thus showing how these figures deteriorate

when the field in the image plane is out of focus. In order to evaluate directly what impact fabrication variations have on device performance, in this section a number of devices are presented of varying size and varying degree of fabrication tolerance, in which the device width, the most sensitive dimension, has been varied. As an illustration of how tolerant MMI couplers can be used to build more complex devices, passive Mach-Zehnder interferometers are presented, which also provide information about the phase relations of the fields at the exit of the constituent 3 dB couplers.

Analytical expressions have been derived by Besse [70] for the fabrication tolerance of MMI couplers, based on the overlap of the imaged field in the output plane of the MMI coupler with the modes of the output waveguides. The fields have been approximated with Gaussian beams, and deviations from the correct longitudinal position of the imaged field have been taken into account by considering the diffraction of these beams. It is shown that in order to limit the loss penalty to α , the deviation δW of the design width W_{mmi} of an $N \times N$ MMI coupler should stay within the bounds given by

$$|\delta W| \leq Z(\alpha) \frac{N\pi}{16} \frac{d_0^2}{W_{mmi}}. \quad (4.14)$$

The exact form of $Z(\alpha)$ will not be discussed here, as it is not important for our purpose. d_0 is the waist of the Gaussian beam describing the input field. The implication of (4.14) is that wider input waveguides, and smaller MMI width, will increase the tolerance for width variations.

It can easily be understood qualitatively how the width of the input waveguides influences the tolerance for width deviations. The diffraction angle of wide input fields will be much smaller than that of narrow input fields. Because the spots at the outputs are *images* of the input field, the same diffractive behaviour will be present at the output (see figure 4.11). Evidently, the focal depth (i.e., the longitudinal displacement of the focal spots that can be tolerated before a certain penalty will be incurred) is much larger for a wide field than for a narrow field. Because width variations induce a longitudinal displacement of the focal spots, a device with wide input fields can tolerate a larger deviation from the design width than a device with narrow input fields.

To experimentally determine how miniaturised, deep-etched MMI couplers behave under variation of the width of the input field, four series of MMI couplers have been made in which the width of the input waveguides has been varied using tapers, as shown in figure 4.12. If the input fields are approximated with a cosine profile, it is easily shown that the $1/e$ width d_0 is approximately $0.76W_{wg}$. The couplers are operated in the general interference regime to avoid having to adjust the position of the access waveguides when the width is varied. The width of the devices is determined by the width of the access waveguides and the (lithographically safe) gap of $1.5\mu\text{m}$. The access waveguide width has been varied from 1.5 to $3\mu\text{m}$, in steps of $0.5\mu\text{m}$. The device dimensions are listed in table 4.2.

For each series of devices, the MMI width has been varied around its design width by varying the gap around its nominal value of $1.5\mu\text{m}$. Figure 4.13 shows the measurement results for the 3 dB couplers, and figure 4.14 shows the results for the cross couplers. It is clear that the

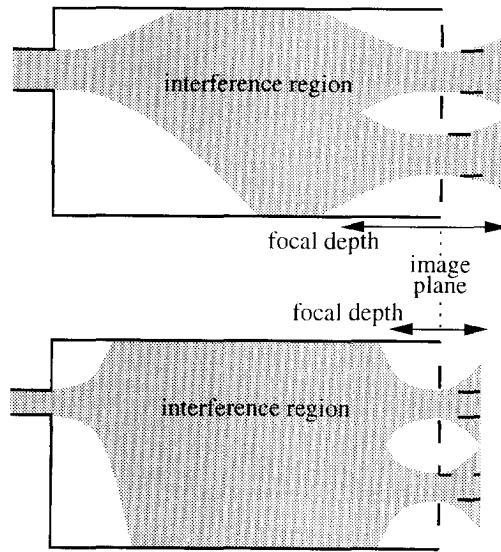


Figure 4.11: A qualitative sketch of the distribution of optical power in MMI 3 dB couplers. The diffraction that takes place at the input will be reproduced in the image plane. A small diffraction angle (top) results in a large focal depth of the output field. A larger diffraction angle (bottom) leads to a smaller focal depth, and a more severe penalty for a deviation in the longitudinal position of the focal spots with respect to the image plane.

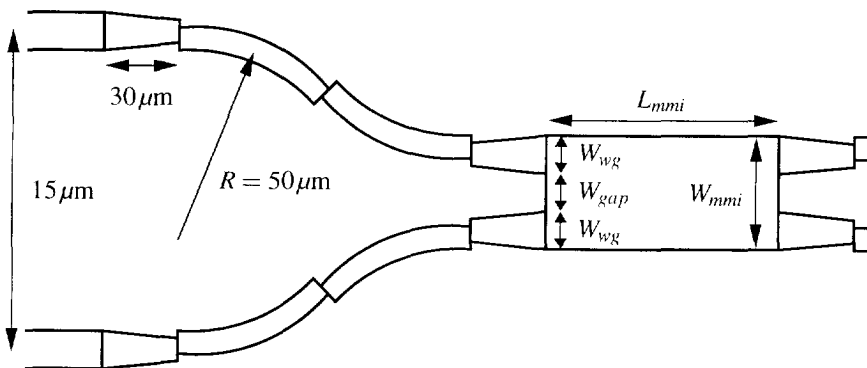


Figure 4.12: Layout of 2×2 multi-mode interference couplers in which the input width is varied by applying tapers. Some design dimensions are indicated.

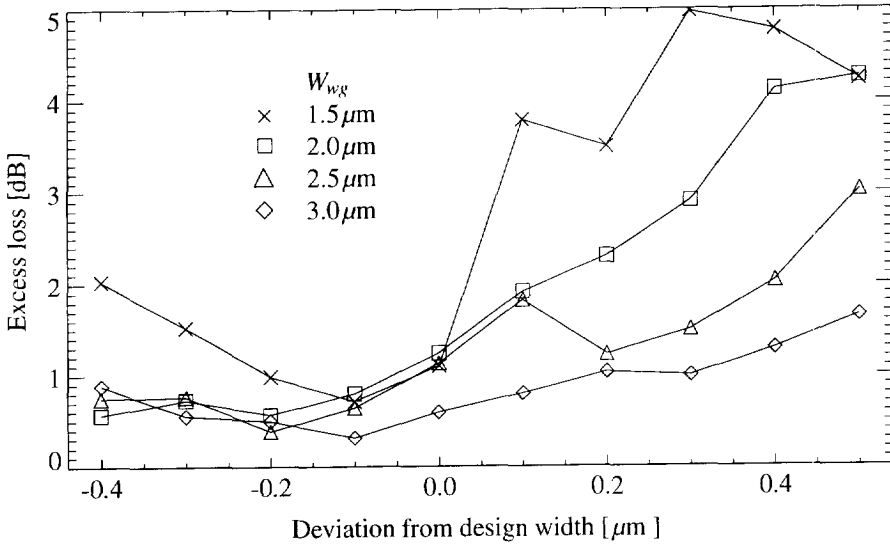


Figure 4.13: Excess loss of MMI 3dB couplers under excitation of one of the inputs. As expected, the dependence on the width deviation is less strong for the devices with wider inputs. The performance optima are found for devices that should have been slightly smaller than the design width, indicating slight lithographic linewidth enlargement. The data are plotted for TE polarisation. Refer to figure 4.18 for a comparison with MPA simulations.

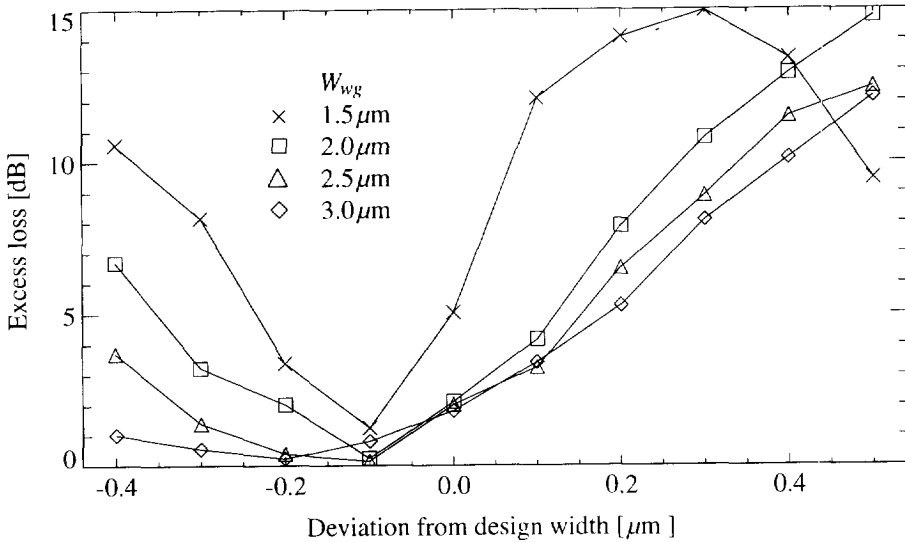


Figure 4.14: As 4.13, but for cross couplers. Refer to figure 4.17 for a comparison with MPA simulations.

W_{wg}	W_{mmi}	d_0^2/W_{mmi}	L_{mmi}	Loss	δW
1.5 μm	4.5 μm	0.29 μm	90 μm	0.7 dB	0.18 μm
			180 μm	1.2 dB	0.06 μm
2.0 μm	5.5 μm	0.42 μm	135 μm	0.6 dB	0.25 μm
			270 μm	0.24 dB	0.07 μm
2.5 μm	6.5 μm	0.56 μm	188 μm	0.4 dB	0.28 μm
			375 μm	0.14 dB	0.14 μm
3.0 μm	7.5 μm	0.69 μm	249 μm	0.3 dB	0.49 μm
			498 μm	0.23 dB	0.18 μm

Table 4.2: Parameters of the MMI couplers for which figures 4.13 and 4.14 show the measurement results. The first four columns are design parameters. L_{mmi} has been determined by MPA simulations. The loss column lists the loss measured for the best device from the series, and the δW column lists the measured width tolerances for a loss penalty of 1 dB. The first of each pair of lines pertains to 3 dB couplers, the second to cross couplers.

width variations have less influence on the devices with wider input waveguides. In table 4.2, the width tolerances δW for a maximum loss penalty of 1 dB have been listed, as obtained by interpolation from the measurement data (see section 4.4). The excess loss in the optimum is listed as well. Figure 4.15 shows the transmission of the most tolerant (249 μm long) 3 dB couplers to both outputs and for both polarisations. Apparently polarisation independent behaviour has been obtained.

Figure 4.16 shows the excess loss and crosstalk of passive Mach-Zehnder interferometers (as sketched in the inset) obtained by combining two 188 μm long MMI 3 dB couplers having input waveguides 2.5 μm wide, with two equal interferometer arms 150 μm in length, making a structure with a total length of 690 μm , including the sections fanning out the access waveguides to a pitch of 15 μm . The best devices have a polarisation independent excess loss of 1 dB and a crosstalk of -25 dB. The deep crosstalk minimum suggests that the phase difference of the fields after the first MMI is very close to the expected 90° , because a deviation from this would cause optical power to appear at the bar output of the device.

4.4 Discussion

The figures 4.6, 4.7 and 4.8 show striking agreement between simulations and experimental data. Apparently, the MPA is a good method to model MMI behaviour especially in the realm of deep-etched structures, where the number of guided modes is high and the influence of laterally radiative modes is unimportant as compared to shallow etched structures.

The figures 4.17 and 4.18 compare the measurements for the tolerance analysis with MPA simulations. Generally, good agreement is found. The simulations ease the estimation of the width tolerance figures δW , which is otherwise difficult because the width steps for which the measurement data are available are hardly fine-grained enough especially for the ‘least tolerant’ ($W_{wg} = 1.5 \mu\text{m}$) series.

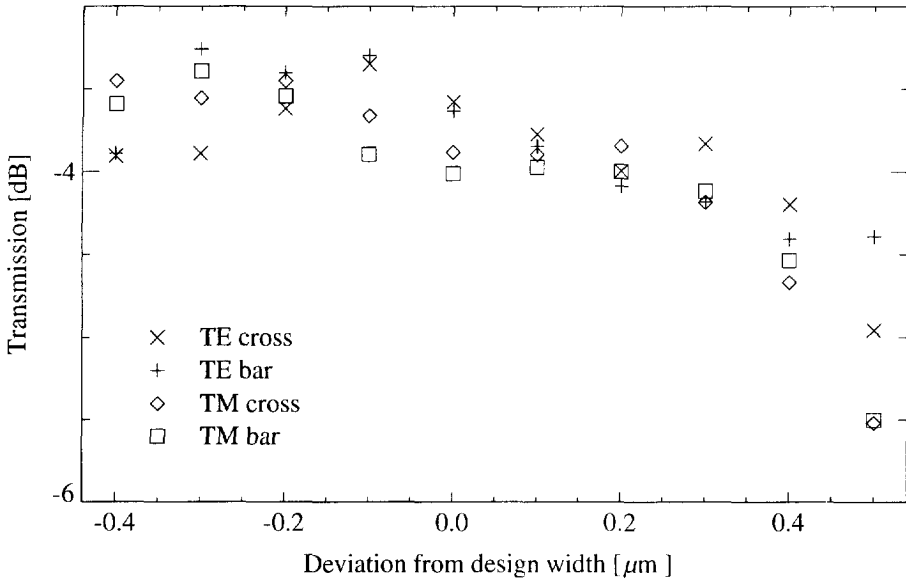


Figure 4.15: Transmission to cross and bar outputs of most tolerant, $249\mu\text{m}$ long 3dB coupler. This coupler works independent of polarisation.

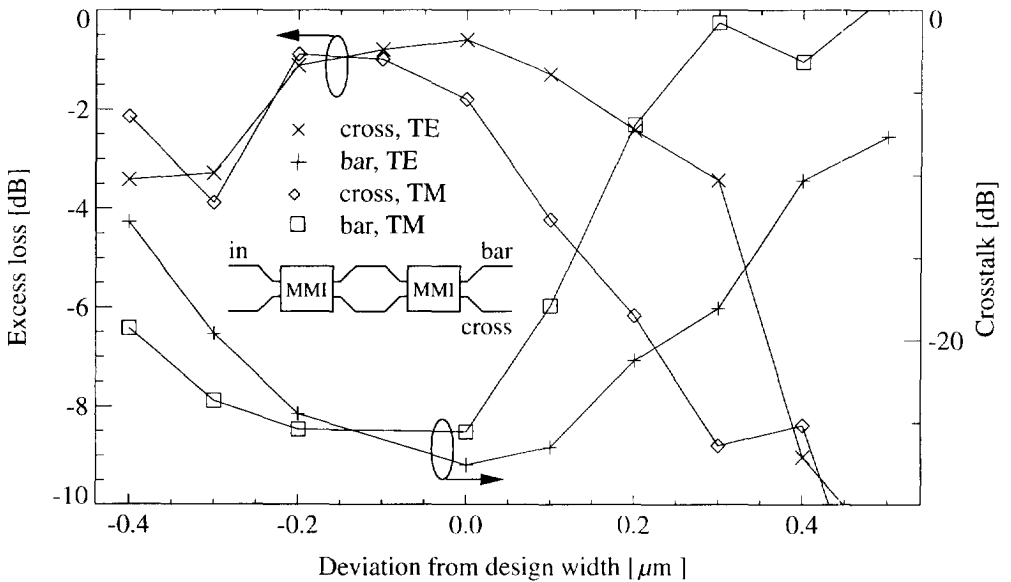


Figure 4.16: Response of passive Mach-Zehnder interferometer. In the optimum, the device exhibits low loss and excellent crosstalk characteristics independent of polarisation.

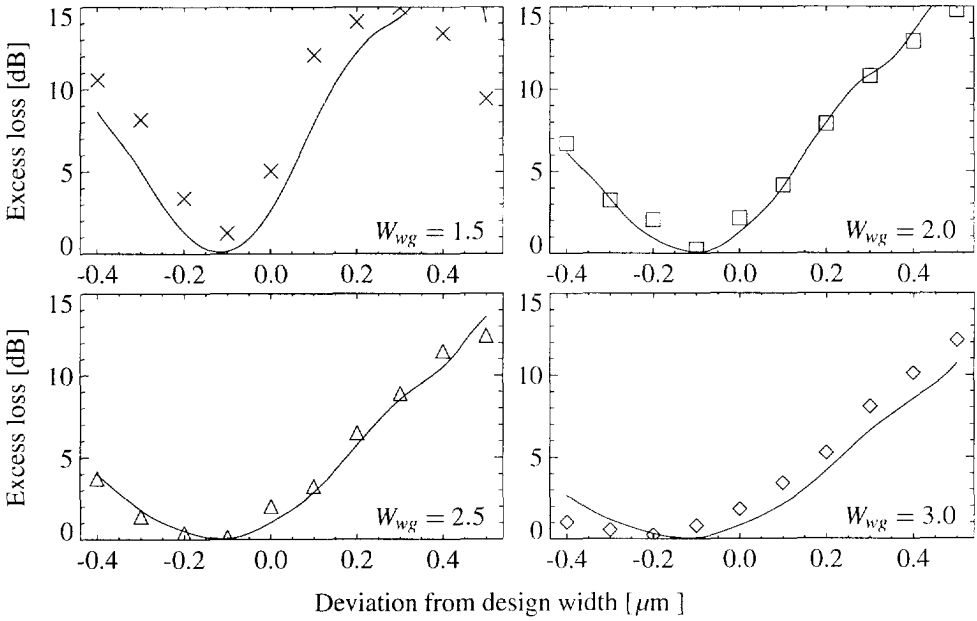


Figure 4.17: Comparison of the excess loss of the MMI cross couplers from figure 4.14 with MPA simulation.

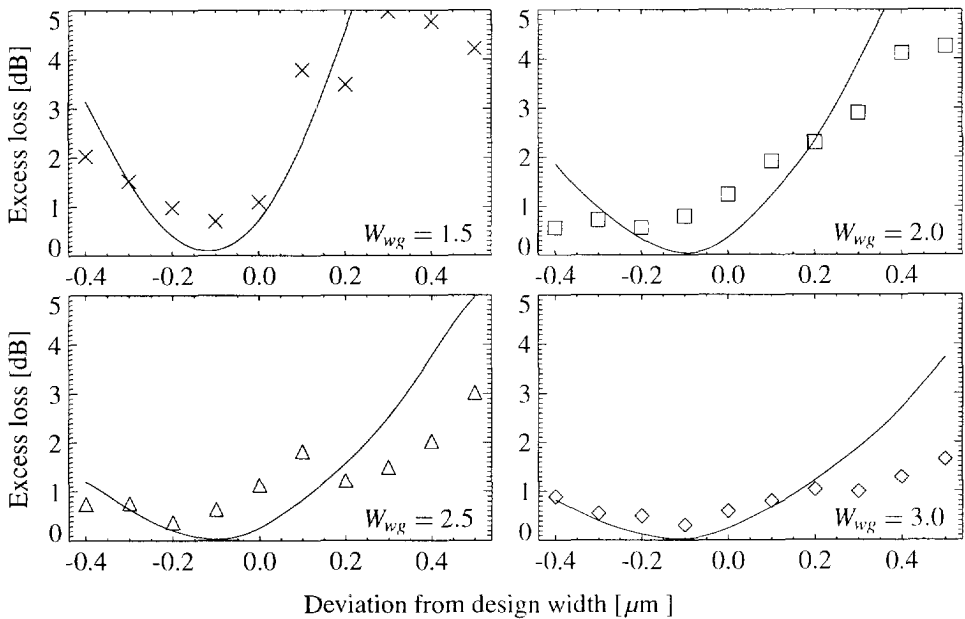


Figure 4.18: Comparison of the excess loss of the MMI 3dB couplers from figure 4.13 with MPA simulation.

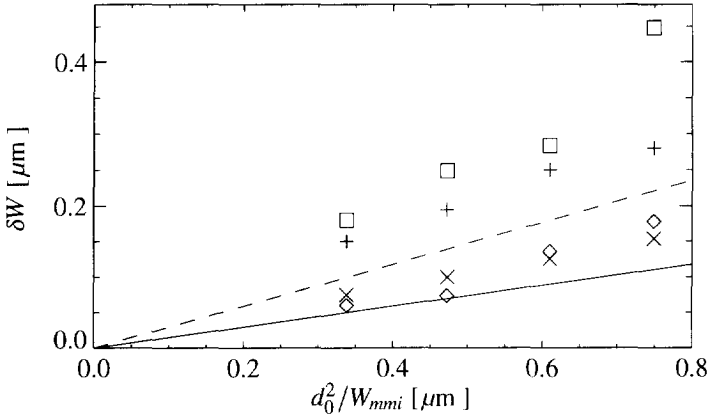


Figure 4.19: δW goes linearly with d_0^2/W_{mmi} according to (4.14). The lines give the theoretical relationship for cross (solid) and 3dB (dashed) couplers, respectively. The \diamond (cross) and \square (3dB) are the experimental values from table 4.2. The \times and $+$ are calculated from the MPA simulations in figures 4.17 and 4.18.

To obtain δW , the distances of the loss minima to the points of 1dB penalty on both sides were determined and averaged. The points of 1dB penalty were estimated by a quadratic interpolation between the minimum loss measurement and the adjacent higher loss measurement, or, where possible, by a linear interpolation between two adjacent higher loss measurements.

The thus obtained values for δW are plotted in figure 4.19 as \diamond (for the cross couplers) and \square (for the 3dB couplers). The values calculated from the MPA simulations are plotted as \times and $+$, respectively, and the width tolerance from the theory of Besse [70] is given as a solid and a dashed line.

The theory of Besse seems to be slightly pessimistic with respect to the MPA simulations. The measured tolerances of the cross couplers are in good agreement with the MPA calculated tolerances, but the 3dB couplers seem to be more tolerant than the calculations predict. This can partly be explained by the fact that the excess losses in the optima are slightly higher, leading to an overestimation of the 1dB penalty width. Nevertheless, the expectation that wider input fields should lead to more tolerant MMI couplers has clearly been confirmed by the measurements. A trade-off exists between device size and fabrication tolerance. When the absolute linewidth definition of the fabrication process becomes twice as accurate, according to figure 4.19, d_0^2/W_{mmi} can become twice as small, leading to MMI devices less than half as long.

4.5 Conclusion

In this chapter the miniaturisation of MMI couplers by using deep-etched structures has been discussed. It has been shown that 3dB couplers with lengths of the order of $100\mu\text{m}$ can be

made. Combining these with the ultra-sharp bends discussed in the previous chapter results very compact structures indeed. Couplers made in this fashion show good balance, making them very suitable for use in Mach-Zehnder structures. The good crosstalk in passive Mach-Zehnder interferometers fabricated suggests that the couplers also exhibit the expected 90° phase difference at the outputs.

It has also been shown in this chapter that miniaturisation has its price. A small MMI width implies less room to connect access waveguides. This leads to narrow access waveguides being used, which results in poor width tolerance due to strong diffraction. Widening the access waveguides and, consequently, also the MMI, leads to better width tolerance in agreement with theory.

4.A Appendix: The Dirac notation

After Pennings [84], the Dirac notation is used in this chapter to denote field profiles and overlap integrals because of its elegance and compactness. The symbol $|\phi\rangle$ denotes a field profile; $|\phi(z)\rangle$ denotes a z -dependent field profile. For real-valued fields, $\langle\phi|$ is identical to $|\phi\rangle$. The scalar product $\langle\phi|\psi\rangle$ is defined as

$$\langle\phi|\psi\rangle \equiv \int \phi(y)\psi(y)dy, \quad (4.15)$$

with y the coordinate across the field profile. With a linear operator A , we have

$$\langle\phi|A|\psi\rangle \equiv \int \phi(y)A\psi(y)dy. \quad (4.16)$$

The fields are assumed to be normalised, i.e., $\langle\phi|\phi\rangle = \langle\psi|\psi\rangle = 1$, so $\langle\phi|\psi\rangle$ is the overlap integral of fields ϕ and ψ . The orthogonality of the modes in a multi-mode structure consisting of materials with real refractive indices can be denoted with $\langle\psi_m|\psi_n\rangle = 0$, for $m \neq n$.

Einstein's summation convention is adopted for summing over all indices that appear more than once in the same term of an equation. E.g., in the spectral decomposition (4.1), $c_n|\psi_n\rangle$ stands for $\sum_n c_n|\psi_n\rangle$. The summation must be replaced by an integration for the continuous part of the spectrum (the radiation modes). The completeness requirement for the modes of a waveguide leads to the *closure relation* $|\psi_n\rangle\langle\psi_n| = I$, with I the identity operator.

Chapter 5

Polarisation independent phased array wavelength demultiplexing on InP

Novel phased array demultiplexer designs have been made by combining the approach of using different array orders for TE and TM to obtain polarisation independence, and a method of flattening of the wavelength response to improve fabrication tolerances with respect to the TE-TM shift.

Two phased-array wavelength demultiplexers have been fabricated, each having four channels per order spaced by 1 nm around a central wavelength of $1.55\mu\text{m}$. It is found that the response of the largest device is broadened, and part of the flattening lost, probably due to variations in the phase transfer of the array. The response of the smaller demultiplexer fits well with the expected shape. It has 0.2 nm of polarisation independent flattened response for each channel, an insertion loss of 1.5–3 dB, and a crosstalk of -17 to -19 dB.

5.1 Introduction

Wavelength Division Multiplexing (WDM) is a simple and effective way of exploiting the large bandwidth of optical fibres. The *Phased Array wavelength (de)multiplexer* [85] has been shown to be the superior WDM multiplexer for systems with a small number of channels [86].

Because of the undefined polarisation state of the signal from an optical fibre, a demultiplexer must be polarisation-independent. For grating demultiplexers, this can be accomplished by exploiting the low polarisation dependence of a low contrast slab waveguide [87]. In phased array devices, it has been achieved in a number of different ways, e.g., by insertion of a half wave plate in the middle of the array waveguides [88], by use of non-birefringent waveguides composed of low band gap InGaAsP [89], by using square embedded waveguides [90], or by

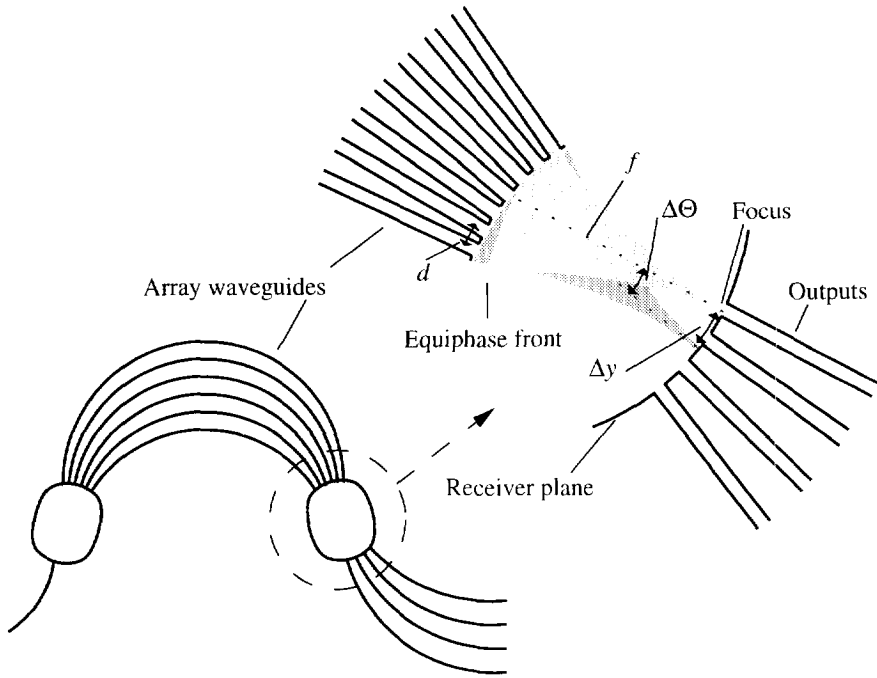


Figure 5.1: Operating principle of a phased array. The input field is reproduced in the receiver plane; tuning the wavelength tilts the phase front, thus addressing different outputs.

a design in which the Free Spectral Range (FSR) of the phased array equals the waveguide TE-TM shift, thus overlapping different orders of the TE and TM response [91].

The latter approach, which is used for the demultiplexers in this chapter, is appealing because it requires no new technology in addition to standard waveguide processing. The most important restriction it imposes is that all demultiplexer channels must fit within a range equal to the TE-TM shift, which limits the number of channels and/or the channel spacing. Several designs using the approach have been reported [91–96].

In addition, the TE-TM shift must be matched very precisely to the FSR, or polarisation independence will be lost. This requirement can be relaxed when the (usually parabolic) pass-band shape can be flattened [97]. This chapter presents the first phased array wavelength demultiplexers that combine the approaches of matching the TE-TM shift with the FSR and flattening of the passband to obtain tolerant, polarisation independent demultiplexers.

5.2 Phased array operating principle

A phased array demultiplexer consists of a dispersive waveguide array connected to input and output waveguides through two radiative couplers as shown in figure 5.1. Its operation is based

λ_c	Demultiplexer central design wavelength
Δl	Length difference of adjacent array waveguides
m'	Number of wavelengths in Δl
m	Order of demultiplexer corrected for dispersion
N_{eff}	Effective (phase) index of mode
N_g	Group index of mode
N_{slab}	Effective index of slab mode in free propagation section
$N_{\text{TE},\lambda_{\text{TE}}}$	Index of TE mode at λ_{TE}
$N_{\text{TM},\lambda_{\text{TE}}}$	Index of TM mode at λ_{TE}
$N_{\text{TM},\lambda_{\text{TM}}}$	Index of TM mode at λ_{TM}
$\Delta\lambda_{\text{TE-TM}}$	TE-TM shift of array waveguides
d	Array waveguide pitch at free propagation section
f	Focal length
$\Delta\Theta$	Phase front tilt
Δy	Focal spot displacement

Table 5.1: List of symbols used in this chapter.

on the imaging of the input field onto the output waveguides. Light from an input waveguide diverging in the first star coupler is collected by the array waveguides, which are designed in such a way that the optical path length difference between adjacent waveguides equals an integer multiple of the central design wavelength of the demultiplexer,

$$\Delta l_{\text{optical}} = N_{\text{eff}}\Delta l = m'\lambda_c, \quad (5.1)$$

where λ_c is *in vacuo*. This results in the phase and intensity distribution of the collected light being reproduced at the entrance of the second star coupler, causing the light to converge and focus on the receiver plane (see figure 5.1). Due to the path length difference, the reproduced phase front will tilt with varying wavelength, thus sweeping the focal spot across different output waveguides.

From (5.1) it follows that m' is the number of wavelengths fitting in the path length difference. This quantity could therefore very well qualify as the *order* of the device. However, the term “order” is also used for the multiplication factor applicable to a phase change, phase front tilt, or other relevant change occurring as a result of a wavelength change. (A high order device needs less wavelength change than a low order device to accomplish the same shift of a focal spot, for instance.) Let us call this multiplication factor m .

In many cases, m' and m are equal. They are not equal in the present discussion, however, and this can be explained by the dispersion occurring in the phased array waveguides. As we have seen, the number of wavelengths fitting in the path length difference Δl is $m' = \Delta l N_{\text{eff}}/\lambda_c$. Now the *change* in the number of wavelengths fitting in this path length difference when we change the wavelength by an amount $\Delta\lambda$ is

$$\Delta m' = \Delta\lambda \frac{dm'}{d\lambda} = \Delta\lambda \Delta l \frac{d \frac{N_{\text{eff}}}{\lambda}}{d\lambda} = -\Delta\lambda \Delta l \frac{N_g}{\lambda_c^2} \quad (5.2)$$

where the definition of the group index has been used:

$$N_g = N_{\text{eff}} - \lambda_c \frac{dN_{\text{eff}}}{d\lambda}. \quad (5.3)$$

Negated, $\Delta m'$ can also be seen as the number of wavelengths that has been 'pushed out' of the phased array arm. (To be more precise, as the difference in number of wavelengths that has been pushed out of phased array arms n and $n - 1$, of course.) When we define, with a modest amount of foresight,

$$m = \Delta l \frac{N_g}{\lambda_c}, \quad (5.4)$$

we recognise the multiplication factor in (5.2):

$$\Delta m' = -\Delta \lambda \frac{m}{\lambda_c}. \quad (5.5)$$

(Note that m is just m' corrected for dispersion by a factor N_g/N_{eff} , as can be seen by comparing equations (5.4) and (5.1).) Because the wavelength in the material still is λ_c/N_{eff} , the phase front will have advanced by

$$\Delta l_{\text{ph}} = -\Delta m' \frac{\lambda_c}{N_{\text{eff}}} = \Delta \lambda \frac{m}{N_{\text{eff}}}, \quad (5.6)$$

or, again said more precisely, the phase front advances in phased array arms n and $n - 1$ will differ by this amount. Since the ends of these array arms lie a distance d apart (see figure 5.1), this will give rise to a phase front tilt

$$\Delta \Theta \approx \Delta \lambda \frac{m}{N_{\text{eff}} d} \frac{N_{\text{eff}}}{N_{\text{slab}}} \quad (5.7)$$

where the rightmost factor is added to account for the transition from the waveguides to the free propagation section of the radiative coupler, where the effective index is N_{slab} ; it is the result of Snell's law.

The tilt leads to a focal spot displacement

$$\Delta y = f \Delta \Theta \quad (5.8)$$

with f the focal length. Smit [92] described a procedure to come to a correct array configuration for a desired $\Delta y/\Delta \lambda$ ratio (i.e., a desired channel spacing given an output waveguide configuration) using only one circularly curved and two straight sections for each array waveguide. This procedure has been used to design the demultiplexers described in section 5.4.

5.2.1 TE-TM shift

Unless special precautions are taken, most planar waveguides are birefringent. Because of the slight difference in the effective indices for TE and TM, wavelengths which are identical *in the waveguide*,

$$\frac{\lambda_{\text{TE}}}{N_{\text{TE}, \lambda_{\text{TE}}}} = \frac{\lambda_{\text{TM}}}{N_{\text{TM}, \lambda_{\text{TM}}}}, \quad (5.9)$$

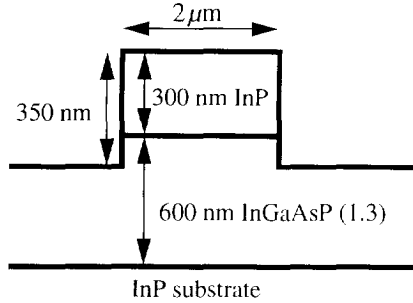


Figure 5.2: Waveguide structure used in the demultiplexer designs.

correspond to differing wavelengths λ_{TE} and λ_{TM} *in vacuo*. This gives rise to a shift in the wavelength response of a phased array $\Delta\lambda_{TE-TM} = \lambda_{TE} - \lambda_{TM}$ which, after correcting for the waveguide and material dispersion with

$$N_{TM,\lambda_{TM}} = N_{TM,\lambda_{TE}} - \Delta\lambda_{TE-TM} \left(\frac{dN_{TM}}{d\lambda} \right)_{\lambda_{TE}}, \quad (5.10)$$

can be shown to be

$$\Delta\lambda_{TE-TM} = \lambda_{TE} \left(1 - \frac{N_{TM,\lambda_{TE}}}{N_{TE,\lambda_{TE}}} \right) / \left(1 - \frac{\lambda_{TE}}{N_{TE,\lambda_{TE}}} \left(\frac{dN_{TM}}{d\lambda} \right)_{\lambda_{TE}} \right) \quad (5.11)$$

which is an expression for the TE-TM shift evaluated at wavelength λ_{TE} .

5.2.2 Polarisation Independent Design

In the waveguide structure that has been used for the fabrication of the demultiplexers described in section 5.4, $\Delta\lambda_{TE-TM}$ is of the order of 4–5 nm. A polarisation independent four channel demultiplexer with channel spacing 1 nm can be designed in such a structure by choosing the array order such that the demultiplexer periodicity, (the FSR), equals the TE-TM shift, in order to overlap the TE_m and the TM_{m-1} demultiplexer orders (shown in figure 5.3):

$$FSR \approx \frac{\lambda_c}{m} = \Delta\lambda_{TE-TM}. \quad (5.12)$$

(The FSR is not exactly equal to $\frac{\lambda_c}{m}$. It is $FSR_+ = \lambda_c / \left(m - \left(1 - \frac{\lambda_c}{N_{eff}} \frac{dN_{eff}}{d\lambda} \right) \right)$ and $FSR_- = \lambda_c / \left(m + \left(1 - \frac{\lambda_c}{N_{eff}} \frac{dN_{eff}}{d\lambda} \right) \right)$ for the longer and the shorter wavelength side, respectively. The FSR is not a constant here due to the fact that we are working with wavelengths instead of frequencies. However, the influence of this is negligible in practice. For a device working in 327th order at $\lambda = 1.55 \mu\text{m}$, which agrees with a TE-TM shift of 4.7 nm, the deviation is less than 0.015 nm.)

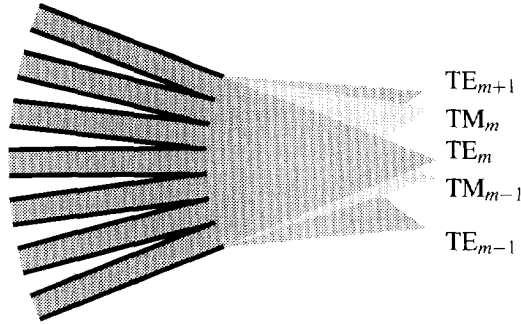


Figure 5.3: The different orders radiating from the waveguide array. The waveguide birefringence causes the TE and TM foci to be separated. By properly choosing the Free Spectral Range, the m th order for TE and the $m - 1$ th order for TM can be overlapped.

However, the equality between λ_c/m and $\Delta\lambda_{\text{TE-TM}}$ in (5.12) is exact. This can be seen by requiring that

$$m' \frac{\lambda_c}{N_{\text{TE},\lambda_c}} = (m' - 1) \frac{\lambda_c}{N_{\text{TM},\lambda_c}}, \quad (5.13)$$

(the mathematical expression of the fact that the demultiplexer works in adjacent orders for the two polarisations), which can be simplified to

$$1 - \frac{N_{\text{TE}}}{N_{\text{TM}}} = \frac{1}{m'}. \quad (5.14)$$

(Here, m' is not the demultiplexer order, but the path length difference between adjacent array waveguides from (5.1), in units of the wavelength in the material.) When the left-hand side of (5.14) is eliminated using (5.11), and both sides are multiplied by $\frac{m'}{m} = \frac{N_{\text{eff}}}{N_g}$, the right hand equality in (5.12) follows. Thus, choosing the (dispersion corrected) order according to

$$m = \frac{\lambda_c}{\Delta\lambda_{\text{TE-TM}}} \quad (5.15)$$

yields polarisation independence.

5.3 Fabrication Tolerance Analysis

Figure 5.4 shows the dependence of the TE-TM shift on different waveguide parameters. The data have been calculated with (5.11), using the InGaAsP refractive index model from [23] for taking account of material dispersion, and a scalar Finite Element mode solver for obtaining the effective mode indices.

It is seen that $\Delta\lambda_{\text{TE-TM}}$, although very tolerant of etch depth variations, is sensitive to layer thickness and waveguide width variations. A layer thickness variation of 3% will cause the

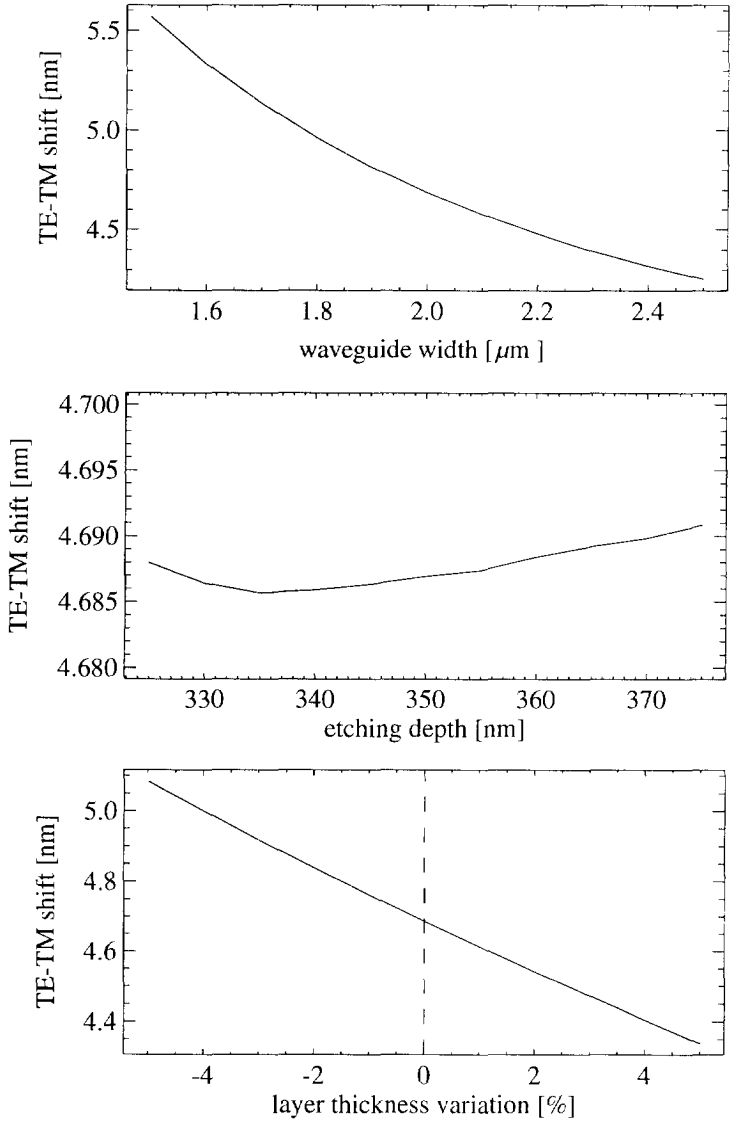


Figure 5.4: Dependence of TE-TM shift on several waveguide parameters. The unperturbed waveguide structure is as indicated in figure 5.2, i.e., with a width of $2\mu\text{m}$ and an etch depth of 350nm . The TE-TM shift hardly depends on the etching depth, but strongly varies with waveguide width and layer thicknesses.

TE-TM shift to deviate 0.2 nm from its computed value, as will a waveguide width variation of $\pm 0.2 \mu\text{m}$. Thus, practical fabrication tolerances will most likely result in a mismatch between the TE-TM shift and the FSR.

In a “traditional”, i.e., non-flattened phased array, the response is determined by the overlap integral of the focal spot (which is an image of the input waveguide field) with the modal distribution in the monomode output waveguides, having a parabolic shape. Therefore, the mismatch has a strong impact on its polarisation independence. However, by flattening the wavelength response of the device over a region of, say, 0.2 nm, there is within practical fabrication tolerances always a certain wavelength range for each channel in which the device works within specs irrespective of the polarisation state of the incoming light.

Flattening of the wavelength response can be done in two ways:

1. The focal spot can be modified so that it approximates a rectangular field profile, as proposed in [98], by adding small path length corrections to the phased array arms, changing the phase distribution at the entrance of the output radiative coupler in such a way that its Fourier transform has the desired shape.
2. Multi-mode output waveguides can be used [97], so that the focal spot, exciting different combinations of modes while sweeping across them, always couples efficiently to the outputs within a certain wavelength range.

The former approach has the obvious advantage that it remains possible to couple the output waveguides of the device to monomode fibres, but it always “spills over” a certain amount of light in the flat wavelength region, and thus necessarily exhibits some additional loss with respect to a traditional phased array. The latter approach is particularly suited for application at the receiver end of a system, i.e., by directly integrating photodetectors on the multi-mode output waveguides. It doesn’t suffer from extra loss, because the output waveguides will collect almost 100% of the light in the focal spot, as long as it is not too close to one of the edges [86]. It should be noted that coupling to a single mode fibre will not be possible when this approach is used, because the loss would depend heavily on the modal pattern in the output waveguides.

5.4 Experimental results

For proper focusing in the receiver plane, the phase transfer through the array arms must be correct, which means that the device must be as small as possible in order for local variations in waveguide width and layer thickness to have as little influence as possible. But the high order in which the device must operate to meet (5.12) will lead to a large device, and employing (wide) multi-mode outputs will cause the device to become even larger, as the focal spot displacement Δy in (5.8) must be bigger to obtain a certain channel spacing $\Delta\lambda$, which requires a larger focal length.

Two different demultiplexers have been designed and fabricated. For the first one, the configuration in the receiver plane has been chosen conservatively, with $6 \mu\text{m}$ wide multi-mode

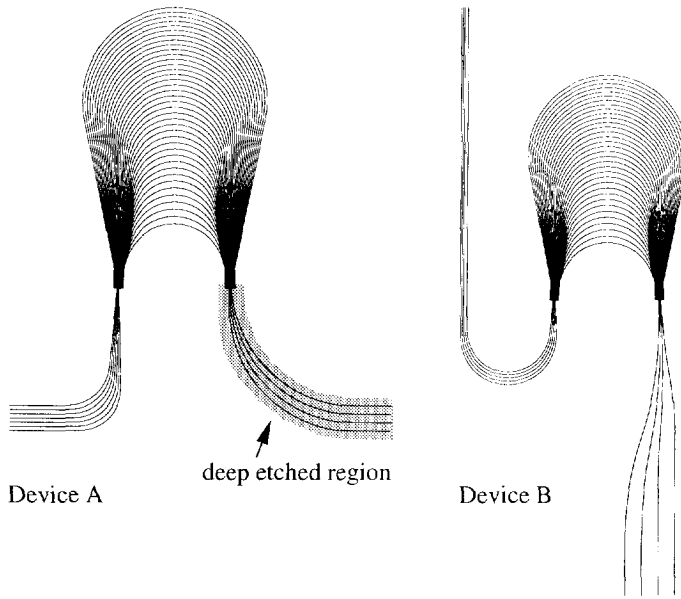


Figure 5.5: Mask layouts of phased array designs.

outputs so as to assure a wide region of flatness, and an output pitch Δy of $9\mu\text{m}$ for low crosstalk between the channels [94]. This device is designated below as demultiplexer A. The standard procedure of fanning the input and output waveguides out towards the chip facets with 90° bends necessitated using an etch window for etching the output waveguides deeper than the device itself, to ensure that higher order modes are not lost, while keeping the output bending radii down to $1500\mu\text{m}$. The device measures $2.2 \times 3.4\text{mm}^2$ excluding the input and output branches. (The layout is shown in figure 5.5.)

When it was found experimentally that the rather large device that this design resulted in showed widening of the passband peaks with less flattening than was expected, and this was attributed to phase transfer variations, another design was made that aimed to be as small as possible. This second demultiplexer [95] (demultiplexer B) has $4.5\mu\text{m}$ wide multi-mode outputs at a pitch of $7\mu\text{m}$, both at the limit of what was thought to give acceptable flattening/crosstalk. For this configuration the simulated response peaks of the demultiplexer are flattened over 0.5nm , and the simulated crosstalk is below -20dB . To avoid having to use the double etch technique again, the device is placed on the chip in such a way that the receiver plane faces the output facet. Therefore, output bends with a very large radius of curvature can be used ($R=4\text{cm}$), and the etch window can be omitted (see figure 5.5). The device size is $2 \times 2.7\text{mm}^2$.

From (5.15) it follows that the devices should work in 327th order (for TE, 326th order for TM). With (5.7) and (5.8), using $\Delta y = 9$ and $7\mu\text{m}$, respectively (and $d = 3\mu\text{m}$ in the present design), the focal lengths f can be found. These are 237 and $210\mu\text{m}$, respectively. (Note that $\Delta\Theta$ is different for the devices, because the wafers available at the time of fabrication had

somewhat different layer stacks.) From the diffraction angle of the input field entering the first radiative coupler, the number of array waveguides needed to catch virtually all of the diffracted light can now be deduced. In our case this was 39 for device A and 30 for device B. The final device designs were made with the procedure described in [92].

5.4.1 Fabrication

The devices were fabricated in layer stacks MOVPE-grown on a Si-InP substrate. For demultiplexer A, a wafer with a 660 nm InGaAsP(1.3) guiding layer and a 320 nm InP top layer was used. Demultiplexer B was made on a wafer with 600 nm InGaAsP(1.3) and 300 nm InP.

A 140 nm thick RF-sputtered SiO₂ layer was used as etch mask. Device A was etched to a depth of 400 nm, after which a photo-resist etching window was applied to etch the output waveguides an additional 50 nm. Device B was etched to a depth of 350 nm in one single etch step. The etching/descumming process as described in section 3.2 has been used for these etching steps. Finally, the devices were cleaved and anti-reflection coated by evaporation of suitable Si_xO_y layers onto the facets.

5.4.2 Transmission experiments

The chips have been measured by launching linearly polarised light from a single-mode source into the waveguides with an AR-coated microscope objective. The output light was picked up from the multi-mode output waveguides with a similar microscope objective and projected onto a Ge-detector.

The propagation loss of straight reference waveguides was measured to be 1.5 dB/cm for device A, and 2.0 dB/cm for device B, for both polarisations. This was determined by Fabry-Pérot contrast ratio measurements of the samples before AR coating.

The response of the demultiplexers was measured by exciting the device in the central input channel. The results are plotted in figures 5.6 and 5.7. The TM peaks are shifted 0.2 nm to longer wavelengths relative to the TE peaks in both cases, indicating that the TE-TM shift is 0.2 nm smaller than the 4.1 and 4.7 nm, respectively, that can be calculated for the waveguide structures.

The peaks of demultiplexer A are wider than the parabolic response expected of a non-flattened device, but certainly cannot be called "flattened". Probably the variations in waveguide structure over the large chip area the device takes up influences the phase transfer of the individual array arms. In addition, the large range of bending radii in the array arms (500-1100 μm) may have given phase contributions, the correction for which may not have been adequate. These two factors can cause a broadening of the image of the input field. The excess loss of the device is 2.5 to 4 dB, and the crosstalk is -14 dB (worst case).

The response of device B is flattened over 0.5 nm, yielding almost 0.3 nm of polarisation independent flattened response for each channel. Its excess loss is 1.5 dB for the inner channels and 3 dB for the outer channels. The crosstalk is -17 (worst case) to -19 dB. This device is smaller than device A, and the range of bending radii in the array arms is only 500-900 μm.

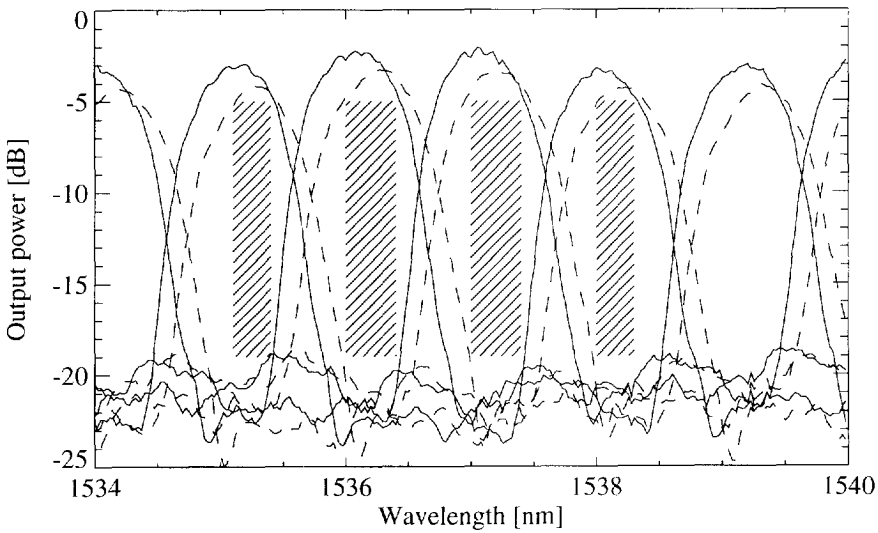


Figure 5.6: Response of each of the four output channels of demultiplexer A for TE (solid) and TM (dashed). The device has 2.5 to 4 dB excess loss. The ranges over which the device has an excess loss below 5 dB and a crosstalk of better than -14 dB are indicated. The adjacent orders can be seen on both sides.

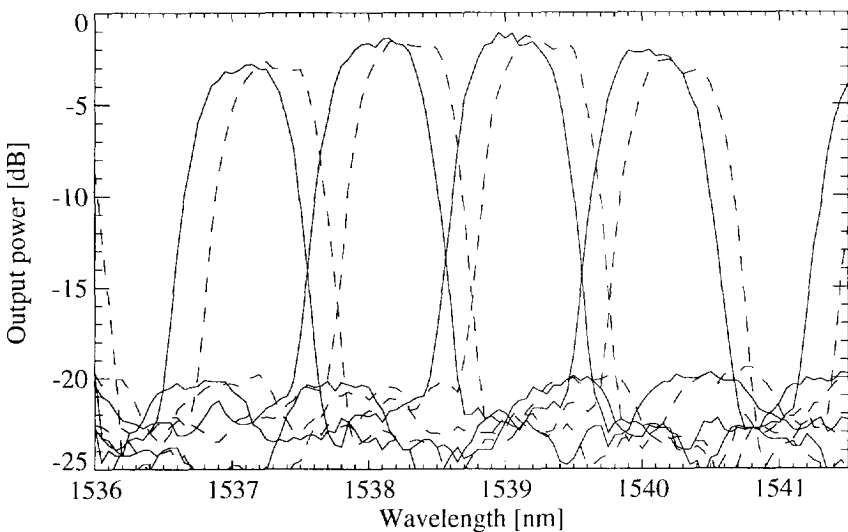


Figure 5.7: Response of each of the four output channels for TE (solid) and TM (dashed) of demultiplexer B. Insertion loss is 1.5 to 3 dB, crosstalk is -17 dB (worst case). There is 0.2 nm of polarisation independent flattened response per channel. The adjacent orders can just be discerned on both sides.

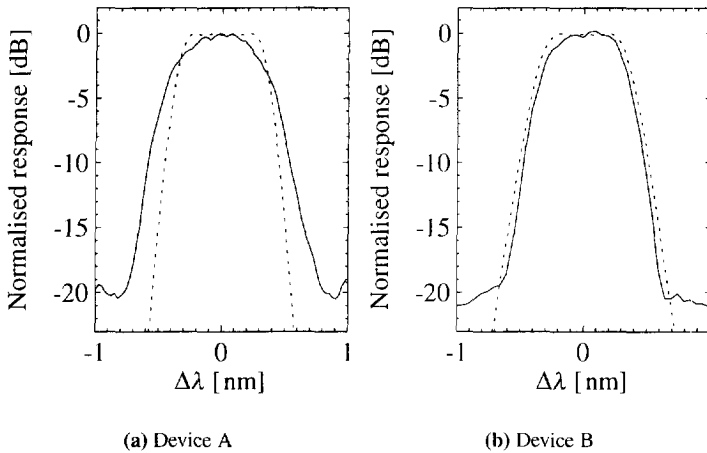


Figure 5.8: Simulated (modal overlap, dotted) and measured (solid) response for a demultiplexer channel. The excellent agreement for device B indicates good focus and phase transfer through the array. Far from the peak wavelength transmission through the substrate (among other things) contributes more than the overlap between focal spot and output guide modes, hence the discrepancies seen there.

Figure 5.8(b) compares the response of one channel of device B with what is theoretically expected, i.e., the field of a monomode input waveguide sweeping across a multi-mode output waveguide. Agreement is excellent, indicating that phase transfer through the array and the focus in the receiver plane are good. Figure 5.8(a) makes the same comparison for device A. Agreement is much worse. Evidently, the smaller device B considerably improves the flatness of the response. Besides that, the maximum insertion loss is reduced from 5 to 3 dB for all channels.

5.5 Conclusion

It has been shown that fabrication of polarisation independent phased arrays is feasible with practical fabrication tolerances by using a flattened response, which counterbalances variations in the TE-TM shift. A four-channel wavelength demultiplexer has been made in InGaAsP/InP with a central wavelength of 1539 nm and a channel spacing of 1 nm. This has been done without requiring new technology and with very simple one step waveguide processing. The insertion loss of the device is 1.5 dB for the inner channels and 3 dB for the outer channels.

Chapter 6

Wavelength demultiplexing with polymeric phased arrays

The possibility to easily fabricate fibre matched waveguide structures in polymer, and the excellent thermal tunability of the refractive index of the material, as well as its low price, make polymer a favourable material for fabrication of photonic devices such as phased array multiplexers. Although a polymeric multiplexer operating around 1300 nm has already been demonstrated, making a device for operation in the 1550 nm wavelength window has proved difficult in the past because of the relatively high material loss around that wavelength. This problem has been addressed by both aiming at a multiplexer design that is as compact as possible, and developing lower loss materials. The result of this work, the first polymeric phased array multiplexer operating around 1550 nm, is presented in this chapter.

Phased Array wavelength (de)multiplexers in a polymeric waveguide structure have been designed for a number of square waveguide structures of $6 \times 6 \mu\text{m}$, with refractive index contrasts of 0.008, 0.006, and 0.004. These contrasts allow for bending radii of 10, 20, and 40 mm, respectively.

At the moment of writing, one processing run has been made with a wafer with a low contrast waveguide structure. The performance of the device meant for this structure is in good agreement with theoretical predictions. A TE-TM shift of 2.5 nm has been found, however, which is ascribed to stress effects originating from thermal processing steps, inducing birefringence in the waveguides.

6.1 Introduction

As mentioned in chapter 5, the Phased Array wavelength (de)multiplexer is an important component for WDM systems with a small number of channels. In such systems, a phased array is needed at the transmitter side to combine several signals of different wavelengths into the same output fibre. At the receiver side, a similar device should demultiplex the signals to different

output channels for detection. In a more complicated system containing multi-wavelength optical cross connects, a larger number of phased arrays is needed, for demultiplexing the incoming signals going into the switching matrix and for multiplexing the signals coming out of the switches into the different output fibres.

Obviously, two approaches are available for constructing an optical cross connect: monolithic integration, for which the InP material system seems to form a good basis, or connecting separate components (multiplexers, switches) with fibres. Clearly, the latter way demands very low fibre to fibre insertion loss, and for the multiplexers also a good match of the absolute wavelength responses of the separate devices.

Components fabricated in polymeric waveguides can satisfy these demands, because the waveguide cores fabricated in this technology are highly compatible with standard single-mode fibre, and the large thermo-optical effect of the used polymers makes easy tuning of the central operating wavelength of the (de)multiplexer possible. The fact that the phased array requires only waveguide processing enables simple fabrication and low-cost mass production.

A 14×14 channel polymeric phased array has already been demonstrated for the $1.3 \mu\text{m}$ wavelength window [99]. Having a multiplexer for the $1.55 \mu\text{m}$ window would be desirable because of the availability of amplifiers (EDFAs) at this window. However, this has proved to be more difficult because of the generally larger polymer material loss around $1.55 \mu\text{m}$. Development of lower loss materials at Akzo Nobel Central Research and design of more compact devices has led to the fabrication of the first polymeric multiplexers around $1.55 \mu\text{m}$ [100, 101].

In this chapter, design, fabrication, and characterisation of 8×8 phased array demultiplexers for the $1.55 \mu\text{m}$ window will be described. First, a waveguide structure will be established which is fibre-compatible and supports the sharp bends needed in phased array demultiplexers. Then, a number of demultiplexers will be designed for different refractive index contrasts. Finally, measurement results will be presented.

6.2 Waveguide structure

Figure 6.1 shows the waveguide structure that has been used as the starting point. It is an embedded square waveguide of $6 \times 6 \mu\text{m}$. The refractive index of the core material is 1.513, and the index of the cladding is 1.509 (the indices are given at $\lambda = 1565 \mu\text{m}$). This waveguide structure can also be used for the fabrication of polymeric thermo-optic switches [102].

There are two basic ways in which such a waveguide structure can be fabricated (see figure 6.2). Polymer layers are spun onto a Si substrate. The waveguide core is formed by either using a photo-bleachable polymer for the middle layer, of which the refractive index can be lowered under influence of UV light, or by reactive ion etching.

The wavelength dependence of the refractive indices of the polymers can be given in the form of a Sellmeier fit. For the waveguide cores used here,

$$N^2 = 1.5089^2 + \frac{0.0297[\mu\text{m}^2]}{\lambda^2}. \quad (6.1)$$

From this, an index $N = 1.51291$ is found at $\lambda = 1565 \text{nm}$, and an index $N = 1.51299$ is obtained at $\lambda = 1550 \text{nm}$. The material dispersion is almost two orders of magnitude smaller

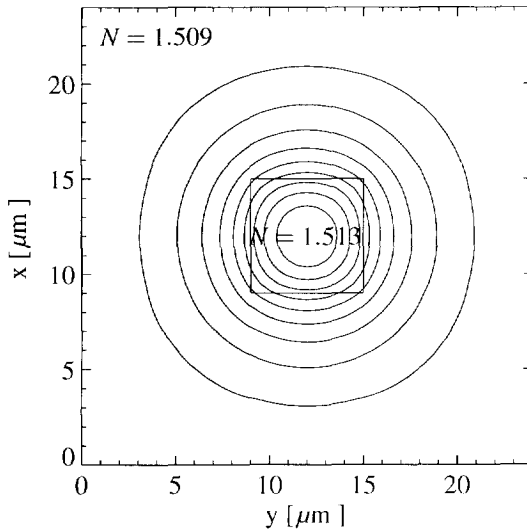


Figure 6.1: The waveguide structure taken as a starting point. The core size of $6 \times 6 \mu\text{m}$ and the index contrast of 0.004 result in fundamental (TE, TM) modes that couple excellently to standard single mode fibre (a few 10ths of a dB coupling loss). The contour lines show an equi-amplitude plot for the field of the fundamental modes in 10% steps.

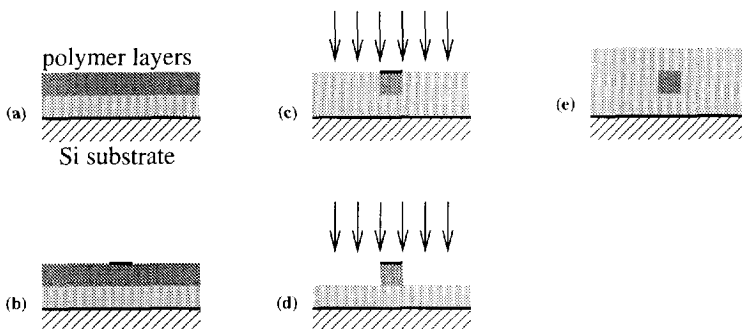


Figure 6.2: Methods to fabricate the waveguide structure of figure 6.1. (a) Spin polymer layers on Si substrate. (b) Apply waveguide pattern. Transfer waveguide pattern into layer by (c) UV photo-bleaching or (d) reactive ion etching. (e) Remove mask pattern and spin on top layer.

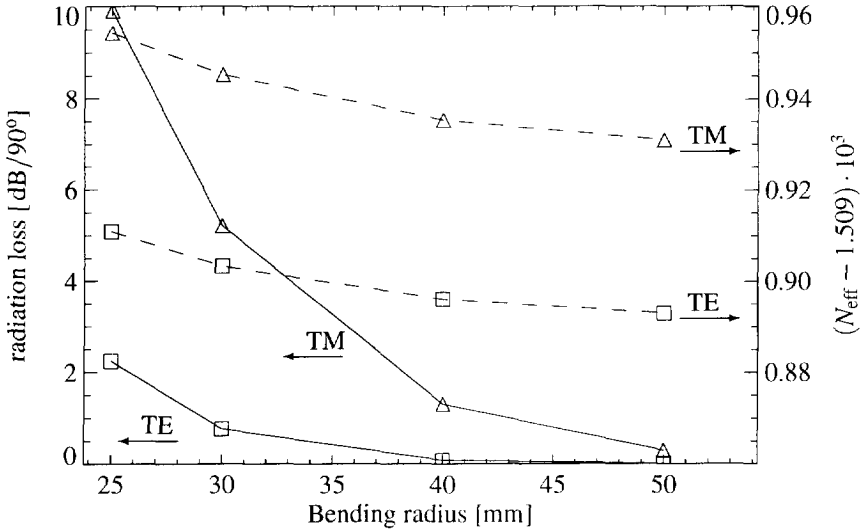


Figure 6.3: Radiation loss and modal effective index for curved waveguides in the structure given by figure 6.1. Note that the right axis runs from 1.50986 to 1.50996; ΔN_{eff} due to the bend is of the order of 10^{-5} .

than that of InP. $\lambda_c \frac{dN_{\text{eff}}}{d\lambda} \approx 8 \cdot 10^{-3}$ in (5.3), so N_g and N_{eff} differ by approximately 0.5%, instead of around 10% for InP. Material dispersion can therefore be neglected.

The refractive index contrast in the waveguide of figure 6.1 is very small in comparison to the index contrasts in the InP-based waveguides discussed in earlier chapters. This can pose problems with the minimum allowable bending radius of curved waveguides, and with coupling between adjacent waveguides. Due to this coupling the distance between the receiver waveguides (see figure 5.1) has to be chosen large in order to avoid excessive crosstalk, and this increases the dimensions of the multiplexer.

6.2.1 Radiation loss in curved waveguides

The radiation loss calculations that follow were done with a two-dimensional mode solver for curved waveguides based on the Method of Lines [103]. With this method, regions containing possible solutions for N_{eff} in the complex plane are found by searching local extrema of a characteristic equation. When these regions are determined, one is chosen and a mode is found by a complex zero search algorithm. This results in the effective index of the mode and the radiation loss per 90° . Finally, the three components of the modal field are calculated, from which it can be determined which mode was found.

Figure 6.3 shows the radiation loss of the TE and TM fundamental modes in the waveguide structure described above. (These are the only modes guided by the structure.) Also shown are the modal effective indices, which are almost independent of the bending radius. A correction for the ‘bending effect’ as mentioned in [86], pp. 53–57 therefore seems unnecessary for these

waveguides.

The polarisation dependence of the waveguides is low: The TE-TM shift is approximately -0.04 nm, and this is probably more a computational than a physical effect, because this value remains almost constant even in the limit of large bending radius.

6.2.2 Coupling between waveguides

Directional coupling between waveguides is one of the mechanisms of crosstalk between the output channels of a phased array. The other mechanism is coupling of part of the light that is focused in the receiver plane into an unwanted output channel. Both crosstalk mechanisms are influenced by the distance of the output waveguides in the receiver plane. For low contrast waveguides, coupling between waveguides is the more serious problem. From modal overlap it can be calculated that crosstalk due to coupling of the focal spot to the wrong output waveguide is less than -50 dB for a centre to centre output waveguide distance of $20\ \mu\text{m}$. The coupling length for $20\ \mu\text{m}$ spaced waveguides is 18 mm (as calculated from a system mode analysis), which gives a crosstalk due to directional coupling of -21 dB after a propagation distance of 1 mm. These values become 65 mm and -32 dB respectively, for a centre to centre spacing of $25\ \mu\text{m}$. If the distance between the output waveguides is quickly increased by use of curves, the latter figures are probably sufficient.

The present waveguide structure necessitates using an inconveniently large bending radius as large as 50 mm to keep radiation losses low, and a large receiver waveguide pitch, which leads to a large phased array design. Therefore, a higher index contrast structure is considered next.

6.2.3 High contrast waveguide structures

Fibre-optimised multi-mode structure

As seen in chapter 3, lower bending loss can be obtained by increasing the refractive index contrast. When this is done, the confinement will increase, so the mode will get smaller. To compensate, a larger waveguide core is necessary. After a doubling of the contrast, a core of about $8 \times 8\ \mu\text{m}$ is needed to retain good coupling to a fibre (figure 6.4). The resulting mode profile is almost equal to that of figure 6.1, so the fibre-chip coupling quality should be comparable. The waveguide does become multi-mode, however.

Table 6.1 summarises modal effective indices and radiation losses in this structure. For a bending radius of 10 mm, the fundamental modes have negligible loss, and most of the higher order modes are lossy. However, the TE_{10} mode could become a problem, with only 2 dB/90°.

Single mode structure

The higher order modes that can propagate in the high contrast structure described above may lead to problems in thermo-optic switches (which operate on the basis of mode selection).

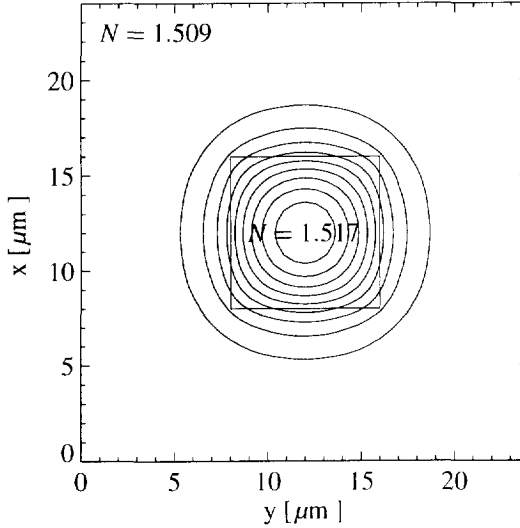


Figure 6.4: Waveguide structure with increased index contrast of 0.008 and core size of $8 \times 8 \mu\text{m}$. The modes of this waveguide couple to a fibre (Gaussian approximated) with a loss of only 0.15 dB more than those of the waveguide depicted in figure 6.1. The contour lines show an equi-amplitude plot for the field of the fundamental modes in 10% steps.

Mode	N_{eff}	Loss [dB/90°]
TM ₀₀	1.51395910	$0.19740 \cdot 10^{-5}$
TE ₀₀	1.51394090	$0.10157 \cdot 10^{-3}$
TM ₁₀	1.51010887	16.710
TM ₀₁	1.51008303	59.167
TE ₀₁	1.51007021	44.750
TE ₁₀	1.51001884	1.8918

Table 6.1: Effective indices and radiation losses for the modes propagating in the structure depicted in figure 6.4, for a radius of curvature of 10 mm, as calculated with the Method of Lines.

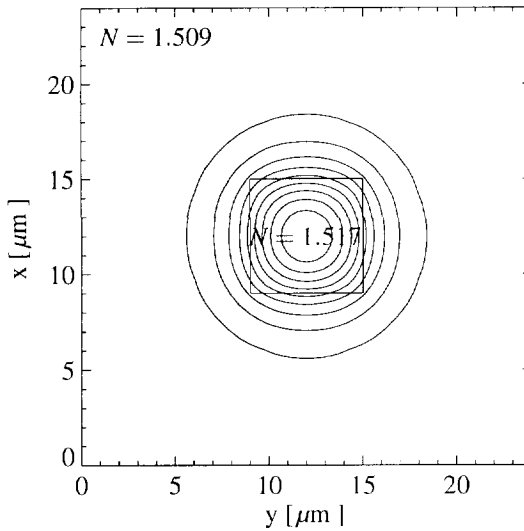


Figure 6.5: Waveguide structure with increased index contrast of 0.008 and core size of $6 \times 6 \mu\text{m}$. The modes of this waveguide couple to a fibre (Gaussian approximated) with a loss of only 0.3 dB more than those of the waveguide depicted in figure 6.1. The contour lines show an equi-amplitude plot for the field of the fundamental modes in 10% steps. The structure only guides the fundamental TE and TM modes.

Because in the future polymeric phased arrays and switches will be integrated to form add/drop filters, a monomode waveguide structure must be found.

Reducing the size of the waveguide core to that of the original low contrast structure, while retaining retaining the high index contrast of 0.008, yields single mode waveguides. The result is shown in figure 6.5. With this structure, a penalty of 0.3 dB is suffered in fibre coupling efficiency relative to the fibre matched low contrast structure.

Figure 6.6 shows the radiation loss and the effective mode index of the modes guided by this waveguide structure (the TE and TM fundamental modes are the only ones guided). At a radius of 10 mm, the radiation loss is about 10^{-3} dB/90°, and the mode index is close to that of a straight waveguide. ($N_{\text{eff}} = 1.512582$ is found with the Finite Element Method.)

Waveguides spaced $15 \mu\text{m}$ (centre to centre), will exhibit a coupling length of 44.3 mm. After a propagation distance of 1 mm, -23 dB crosstalk will result. The allowable bending radius being almost an order of magnitude smaller than in the case of the fibre matched waveguides of section 6.2, the output waveguides can be made to diverge sufficiently quick to keep the resulting crosstalk considerably lower.

6.2.4 Fabrication variations

A variational analysis performed on the high contrast waveguides of section 6.2.3 shows that when the waveguide width increases with $0.5 \mu\text{m}$ (or the thickness increases with 5%, which

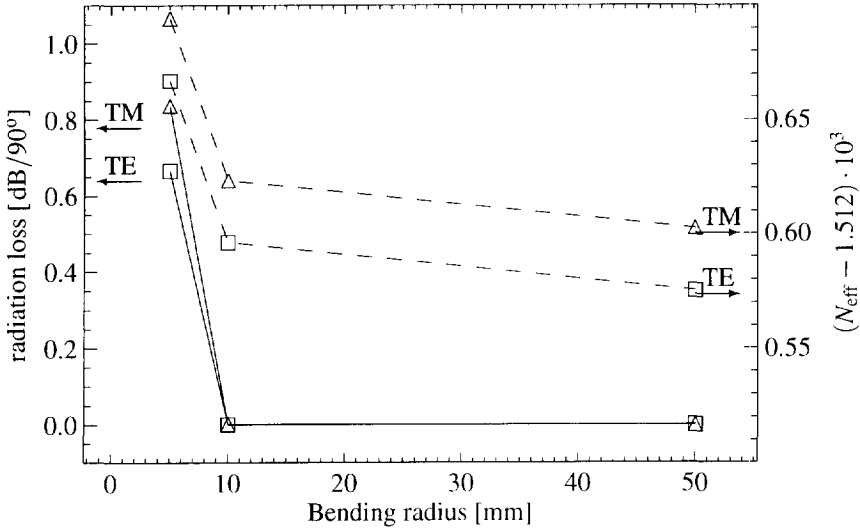


Figure 6.6: Radiation loss and modal effective index for curved waveguides in the structure given by figure 6.5.

is the same, because the waveguides are square), the effective index of the fundamental modes increases with 0.000122, or 0.008%. When the core and cladding indices are raised with an amount 0.0001, the effective index, not surprisingly, increases with the same amount. Even a refractive index change 10 times larger will cause an effective index change of only 0.07%, which means that optical path lengths will change with this same amount.

Variations like those mentioned above will have a considerable influence on the central wavelength of the phased array, but as long as the thermal tunability of the device is larger than the free spectral range, the specified central wavelength can always be reached. The relative change in the other phased array parameters, like the channel spacing and the spectral characteristics of a channel, will be of the order of the optical path length change, and are therefore negligible.

A waveguide width or layer thickness variation does, however, disturb the polarisation independence of the (by design square) waveguides. An enlargement of one of these dimensions of $0.5 \mu\text{m}$, with the other one remaining constant, results in a TE-TM shift of 0.02 nm, which can be neglected.

6.3 Phased array design

A number of phased array wavelength (de)multiplexers have been designed according to the specifications summarised in table 6.2. The frequency accuracy of the device is determined by the thermal tuning capability. With a thermally induced refractive index change of about $-8 \cdot 10^{-5} \text{K}^{-1}$ or $-0.005\% \text{K}^{-1}$, the optical path lengths and thus the central wavelength will

Number of channels	8
Central wavelength	193.41 THz = 1550 nm
Frequency Accuracy	± 6 GHz = ± 0.05 nm
Channel spacing	400 GHz = 3.2 nm
Response > -1 dB	± 60 GHz = ± 0.48 nm
Response < -20 dB	± 300 GHz = ± 2.41 nm
Response < -30 dB	± 700 GHz = ± 5.63 nm
Insertion loss	≤ 10 dB

Table 6.2: Specifications of the (de)multiplexers to be designed.

Response	$\Delta\lambda$	Low contrast (sec. 6.2)	High contrast MM (sec. 6.2.3)	High contrast SM (sec. 6.2.3)
-1 dB (chosen)	0.5 nm	$2.6 \mu\text{m}$	$2.0 \mu\text{m}$	$2.0 \mu\text{m}$
Dispersion		$5.2 \mu\text{m}/\text{nm}$	$4 \mu\text{m}/\text{nm}$	$4 \mu\text{m}/\text{nm}$
-20 dB	2.4 nm	$12.6 \mu\text{m}$	$9.7 \mu\text{m}$	$9.6 \mu\text{m}$
-30 dB	3.0 nm	$15.5 \mu\text{m}$	$12.2 \mu\text{m}$	$12.1 \mu\text{m}$
$\Delta\lambda_{\text{chan}}$	3.2 nm	$16.7 \mu\text{m}$	$12.8 \mu\text{m}$	$12.8 \mu\text{m}$

Table 6.3: Wavelength response of the (de)multiplexer in relation to the dispersion. The dispersion is chosen by fixing the 1 dB passband width. The table gives the displacement of the focal spot in the receiver plane for three different waveguide structures that is caused by a change in wavelength $\Delta\lambda$. Note that, even though the specs only require the response to have fallen to -30 dB at $\Delta\lambda = 5.6$ nm, due to the parabolic shape of the response this extinction is already obtained at $\Delta\lambda = 3$ nm.

change with the same relative amount, from which it follows that $\Delta\lambda_c = -0.08 \text{ nm K}^{-1}$. A temperature stability of ± 0.5 K will be needed to stay within the specified frequency accuracy of ± 0.05 nm for this thermo-optic coefficient. This can be done by means of a Peltier element. The other parameters are directly related to the phased array design, and will be discussed below.

6.3.1 Channel spacing and wavelength response

The wavelength response of a phased array is determined by the parabolic variation of the coupling efficiency when the focal spot in the receiver plane sweeps over an output waveguide. The width of the passband is the only degree of freedom left in this response. It can be chosen by specifying the desired response in dB for a certain $\Delta\lambda$ off the channel wavelength, thereby fixing the dispersion of the phased array, i.e., the shift in μm of the focal spot of the array in the receiver plane per nm of wavelength change. This quantity is conveniently denoted by the unit $\mu\text{m}/\text{nm}$.

When the 1 dB point is chosen at ± 0.5 nm, according to the specifications given in table 6.2, the dispersion needed is fixed for the three waveguide structures discussed as indicated in

	Specified	Low contrast	High contrast MM	High contrast SM
$\Delta\lambda_{\text{chan}}$	3.2 nm	25 μm	15 μm	15 μm
Dispersion		7.8 $\mu\text{m}/\text{nm}$	4.7 $\mu\text{m}/\text{nm}$	4.7 $\mu\text{m}/\text{nm}$
1 dB	0.48 nm	0.33 nm	0.43 nm	0.42 nm
1.1 dB			0.48 nm	
1.3 dB				0.48 nm
2.0 dB		0.48 nm		
20 dB	2.41 nm	1.6 nm	2.1 nm	2.0 nm
30 dB	5.63 nm	2.0 nm	2.6 nm	2.6 nm

Table 6.4: Wavelength response of the (de)multiplexer with the dispersion determined by the output waveguide distance. This distance in the receiver plane is chosen according to the crosstalk requirements. From this follows the array dispersion, which in turn fixes the passband shape.

table 6.3. The 20dB and 30dB bandwidths are also given, as well as the distance the focal spot travels in each case. It is seen that the centre-to-centre distance of the output waveguides needed to obtain the specified channel distance is smaller than what was seen in the previous sections to be the minimum receiver waveguide separation needed for low crosstalk.

We can also approach the problem the other way around. First the receiver waveguide distance is determined from the crosstalk requirement obtained earlier; the array dispersion is then fixed by the desired channel spacing. Table 6.4 lists the shape of the passband at the specified $\Delta\lambda$'s. The specification for the 1 dB response within ± 0.48 nm cannot be met for the low contrast structure, but it is almost met for the other structures.

6.3.2 Insertion loss

The specified maximum insertion loss is 10dB. When 2×0.5 dB for each of the fibre-chip couplings and about 4 dB for the propagation loss (sc. 0.5 dB/cm over a 3" wafer) are subtracted, we are left with an allowable insertion loss of the phased array alone of about 5 dB.

The loss of a phased array consists of two main contributions [92]: the loss of the (virtual) central channel, and the extra loss of the outer channels (the angular loss). The first contribution is the result of the coupling loss the input field suffers when it is diffracted in the input free space region and is coupled into the array waveguides, and of the power lost into higher orders at the output free space coupler. (These parts are equal, because they are two sides of the same reciprocal mechanism.)

Figure 6.7 shows the loss as a function of the gap between the array waveguides according to the simple formula (6.22b) in [92], p. 194. The gap range shown isn't likely to pose problems for lithography; only spin-coating the cladding in small gaps may be an obstacle.

The contribution of the angular loss is directly related to the focal length of the free space couplers. For larger f the angular loss will be smaller because the outer channels of the (de)multiplexer can be reached with less angular displacement of the focal spot.

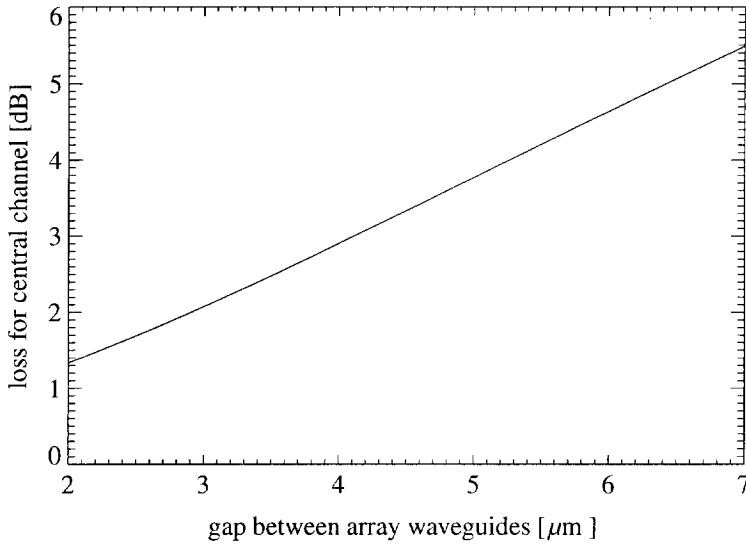


Figure 6.7: The diffraction loss for a (virtual) central channel as a function of the gap (in μm) between the array waveguides for medium contrast polymeric waveguides, which have an effective mode width of about $4.5\mu\text{m}$.

6.3.3 Free propagation sections

Figure 5.1 shows the configuration of the output free propagation coupler of a Phased Array (de)multiplexer. A number of parameters are indicated which, in conjunction with the dispersion of the array, determine the properties of the (de)multiplexer.

For the central wavelength, the field in the coupler has an equi-phase front at the ends of the array waveguides, and the light is focused onto the centre of the receiver plane at the focal distance f . Due to the dispersive nature of the waveguide array, a wavelength change will incur a tilt of this equi-phase front and a shift of the focal spot.

By crosstalk considerations, we have already determined that the output waveguide distance y should be $15\mu\text{m}$ (in the high contrast structure), so this is the distance the focal spot must travel for a wavelength change of $\Delta\lambda_{\text{chan}} = 3.2\text{nm}$. The angular displacement $\Delta\Theta$ needed to accomplish this can be varied with f according to the relation (5.8).

Relative outer channel loss

Assuming a Gaussian far-field radiation pattern for a single waveguide, we can assume an equivalent Gaussian loss envelope for the field in the receiver plane when the focal spot sweeps along it:

$$L(\Theta) = 10 \log e^{-2 \frac{\Theta^2}{\Theta_0^2}} \quad (6.2)$$

with $\Theta_0 \approx \frac{\lambda/N_{\text{slab}}}{\pi w_0} = \frac{1.550/1.515}{3.8\pi} = 0.086\text{rad}$ for the high index waveguide structure.

It follows that for a maximum outer channel loss of, e.g., 2 dB relative to the virtual central channel, the angle at which this channel is addressed should be at most 0.041 rad, so that we must have $\frac{1}{2}(N_{\text{ch}} - 1)y = 3.5y = 0.041f$, or $f = 1280\mu\text{m}$. Increasing f of course decreases the relative outer channel loss, but at the same time necessitates increasing the number of array waveguides to avoid spillover at the input free propagation coupler [92], increasing the total size of the device.

Central channel loss

The loss for the virtual central channel is mainly caused by radiation into adjacent orders in the output free propagation coupler, and due to coupling loss in going from the input free propagation region to the array waveguides. (These loss contributions are equal in size due to reciprocity.)

In figure 6.7, the dependence of the central channel loss on the gap between the array waveguides is given. A gap of $3\mu\text{m}$, corresponding to $d = 9\mu\text{m}$ in figure 5.1, results in a loss of approximately 2 dB. Lower losses are possible with a smaller gap, but technological difficulties might arise when it is made too small. (Hida [99] already experienced difficulties with the larger value of $d = 25\mu\text{m}$. He mentions cracks appearing in the spinned-on cladding film due to stress differences between this film in the free propagation region and in the array. In our technology, previously used to fabricate sharp y-junctions for thermo-optic switches, $d = 9\mu\text{m}$ is thought to be a safe value.)

6.3.4 Waveguide array

Path length difference

Under a wavelength change $\Delta\lambda$, the difference in wavefront displacement between array waveguides n and $n - 1$ is $m\frac{\Delta\lambda}{N_{\text{eff}}}$, with m the order in which the (de)multiplexer works. Such a phase change difference leads to a phase front tilt

$$\Delta\Theta \approx \frac{m\Delta\lambda}{dN_{\text{eff}}} \frac{N_{\text{eff}}}{N_{\text{slab}}}, \quad (6.3)$$

at the start of the free propagation output coupler, with the rightmost factor correcting for refraction at the array/slab transition. From the geometry described in section 6.3.3, it follows that m must be 50. The fact that m was rounded to the nearest integer gives a slight correction to the focal length: $f = 1274\mu\text{m}$.

The difference in the number of wavelengths that fit in array waveguide n and array waveguide $n - 1$, m' , follows from

$$\frac{m'}{m} = \frac{N_{\text{eff}}}{N_{\text{g}}}, \quad (6.4)$$

with the group index

$$N_{\text{g}} = N_{\text{eff}} - \lambda_c \frac{dN_{\text{eff}}}{d\lambda}. \quad (6.5)$$

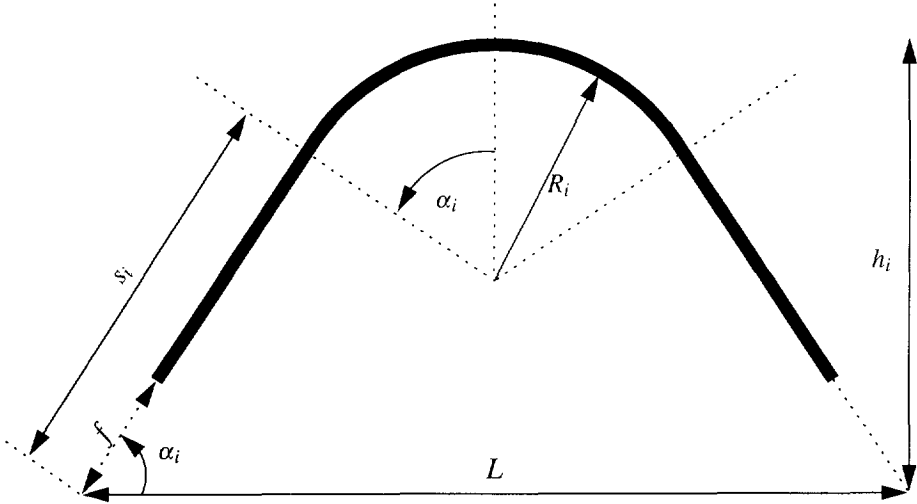


Figure 6.8: Geometry of the i -th arm of a phased array.

Even though material dispersion is very low, $\frac{dN_{\text{eff}}}{d\lambda} \approx -8.6 \cdot 10^{-6} \text{ nm}^{-1}$ due to waveguide dispersion. Therefore, N_g is almost 1% higher than N_{eff} , and $m' \approx 49.56$. Now the length difference between adjacent array waveguides must be

$$\Delta l = m' \frac{\lambda_c}{N_{\text{eff}}} = m \frac{\lambda_c}{N_g} \approx 51 \mu\text{m}. \quad (6.6)$$

Array layout

In order to avoid spillover at the input free propagation coupler, the array aperture must be taken sufficiently large, e.g., $4\Theta_0$ for a spillover $< 0.01\%$ [92]. This corresponds to an array aperture of 20° , and 50 array waveguides.

In the strategy described in [92] to construct the waveguide array, each array waveguide consists of two straight waveguide sections emanating from the free propagation sections and one curved waveguide connecting them. The curved waveguides of the array are not necessarily concentric, and there are only two straight/curve junctions in each arm.

The configuration is fully defined by the sets R_i , s_i , and α_i , respectively denoting the radius of the curved section, the length of the straight section (including the focal length, to simplify the formulas), and the angle between the straight sections and the base line of the array (the line through the centre of the receiver plane and the centre of the transmitter plane; see figure 6.8). These sets can be found by solving

$$\alpha_i = \alpha_0 + i\Delta\alpha \quad (6.7)$$

$$l_i = l_0 + i\Delta l = 2s_i + 2\alpha_i R_i \quad (6.8)$$

$$L = 2s_i \cos \alpha_i + 2R_i \sin \alpha_i, \quad (6.9)$$

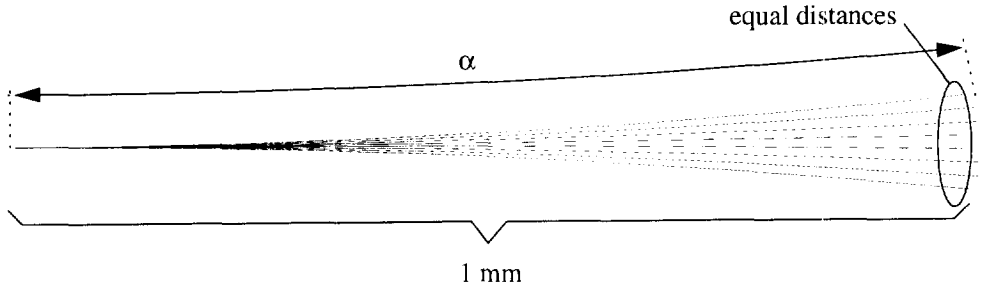


Figure 6.9: Construction of the input/output waveguides, equidistant at a distance of 1 mm from the start.

for a suitable choice of α_0 , l_0 , and L . $\Delta\alpha$ follows from f and d , and Δl has been found in (6.6). A procedure for the construction is given in [92] and [86].

By properly choosing values for the three degrees of freedom, array configurations have been found which yield reasonably small (de)multiplexers in which the spread in R_i 's is small (so a correction for the *bending effect* ([86], pp.53–57) is unnecessary), and which has a minimal waveguide separation Δh at the point half way the array arm of $31\ \mu\text{m}$.

6.3.5 Crosstalk in the array

If the distance between the waveguides in the array becomes too small, the array arms will no longer be decoupled, and crosstalk in the array will occur, distorting the response. However, up to the junction between the straight and the curved section in the array, crosstalk does no harm [92], because in all waveguides the light has the same phase. At this junction in the outmost array waveguide, the distance to the adjacent arm is $18\ \mu\text{m}$, and in the case of parallel waveguides the coupling length would be $l_c \approx 17\ \text{cm}$. For the central array arm, where most of the optical power is, the distance at the junction is $25\ \mu\text{m}$, and l_c is over 4 m. Of course these numbers are only approximations, because we are not dealing with parallel waveguides, but they seem to indicate that crosstalk in the array will not be of such order that it will deteriorate the response of the device.

6.3.6 Input/output waveguide configuration

The input/output waveguides of the two smallest phased arrays have a pitch at the transmitter/receiver plane of $15\ \mu\text{m}$. In two parallel straight waveguides with this centre-to-centre distance, a crosstalk of $-23\ \text{dB}$ would occur after a propagation length of 1 mm as a result of directional coupling. Therefore, it is important that the input/output waveguides fan out as quickly as possible, e.g., by using curves. Optimally, the gaps between them should increase evenly while moving away from the free propagation sections.

In order to determine the optimal configuration, a construction is made in which the bending radius of the two outer waveguides is taken to be the minimum allowable bending radius

Refractive index contrast	0.008	0.006	0.004
λ_c	1550 nm		
$\Delta\lambda_{\text{chan}}$	3.2 nm		
Number of channels	8		
Receiver pitch y	15 μm	18 μm	20 μm
Array pitch d	9 μm	10 μm	11 μm
w_0	3.8 μm	4.2 μm	5.0 μm
Θ_0	4.9°	4.5°	3.7°
Order m	50		
Free spectral range	31 nm		
Focal length f	1274 μm	1698 μm	2075 μm
Central channel insertion loss	2 dB	≈ 2 dB	≈ 2 dB
Angular insertion loss	2 dB	≈ 2 dB	≈ 2.3 dB
Array aperture ($=4\Theta_0$)	20°	18°	15°
Number of array waveguides	50	54	51
R_{min}	10.00 mm	19.69 mm	39.74 mm
R_{max}	10.24 mm	20.05 mm	49.31 mm
Δh_{min}	31 μm	33 μm	56 μm
Array base length L	19.3 mm	33.0 mm	52.3 mm
Array height h_{max}	6.3 mm	8.4 mm	8.7 mm

Table 6.5: Properties of the Phased Array designs for the three refractive index contrasts. All designs are for $6 \times 6 \mu\text{m}$ square waveguide structures. Entries that have been left empty in the last two columns are equal to the entry in the first column.

($R = 10\text{mm}$ for the highest contrast device), and the gaps are chosen to be distributed evenly at a distance of 1 mm of the free propagation section. To simplify the mathematics, the waveguides are assumed to emanate from the same point. (See figure 6.9.) Due to the gap and angle between the waveguides in the real design, the distance at 1 mm in the real device will be even larger than calculated here.

6.3.7 Summary of device parameters

All references made in the previous sections to actual dimensions and values are for a phased array intended for a high contrast waveguide structure. Two more designs have been made for lower contrast structures. An overview of the parameters of the three devices is given in table 6.5. The device designed for the lowest contrast structure barely fits on a 4" wafer, so the construction described in section 6.3.6 is not used in it in order to save length. Still, a rather small minimum bending radius of 40mm had to be used to make the device fit, which will probably result in about 1dB extra loss for TM polarisation (see figure 6.3).

Figure 6.10 shows the mask layout for the designed devices, in which the sizes of 3" and 4" wafers are indicated. The fanned-out input/output waveguides of the devices are continued in a curve in such a way that they end up as parallel waveguides with a pitch of $250 \mu\text{m}$.

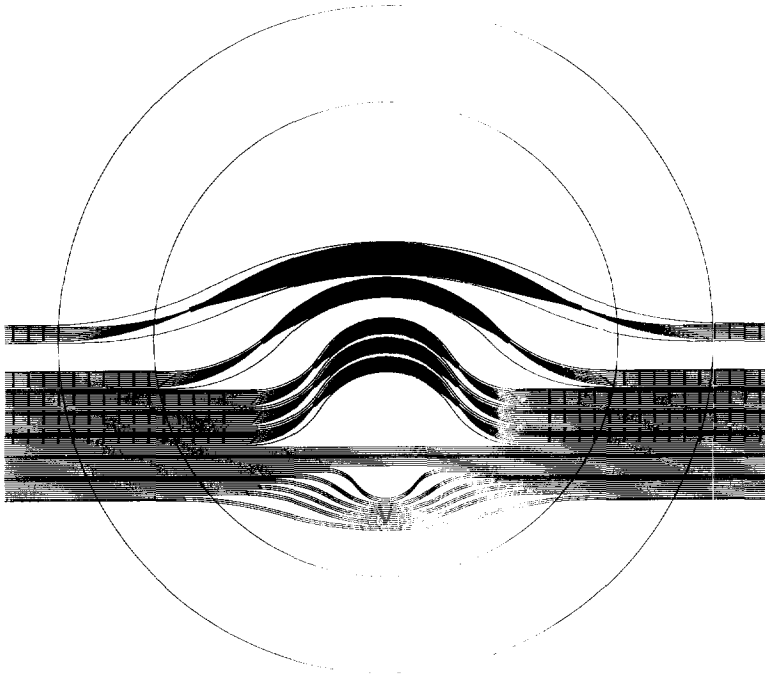


Figure 6.10: Overview of the mask layout for the polymeric (de)multiplexers, in actual size. The circles with diameters of 62 and 88 mm indicate the usable area of 3" and 4" wafers.

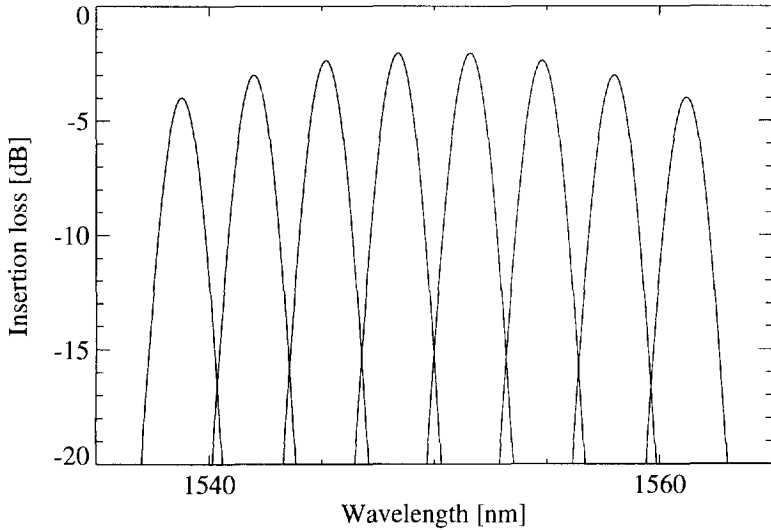


Figure 6.11: Theoretical response of the high contrast Phased Array (de)multiplexer.

Figure 6.11 shows the theoretical response of the high contrast device. This figure was produced on the basis of the overlap integral of the image of the input modal field with the output waveguides. The central channel loss and the angular loss have been taken into account. However, no crosstalk or phase transfer phenomena have been taken into account, nor have fibre-chip and propagation losses been accounted for, so it must be stressed that this figure is *not* a rigorous simulation of the device. It just serves as an example of what kind of response we might expect.

6.4 Experimental results

At the moment of writing, one processing run has been finished with a wafer with a low contrast waveguide structure, which has been fabricated with reactive ion etching. The devices are measured by butt-coupling cleaved fibres (*in casu* the end faces of standard FC/PC connectors) to the as diced wafer, using some index matching liquid to fill the air gaps.

6.4.1 Demultiplexers

An external cavity laser has been used to excite the largest demultiplexer in one of the central inputs (input 4, counting from the top in figure 6.10). Figure 6.12 plots the wavelength dependent loss for all eight phased array channels. The fibre-to-fibre loss in the transmission maxima is 10dB. Crosstalk is between 20 and 25dB. The rising crosstalk background towards larger wavelengths is caused by the rising spontaneous emission in the source, that is driven towards the end of its wavelength range. The central wavelength of the device is 1555nm at room

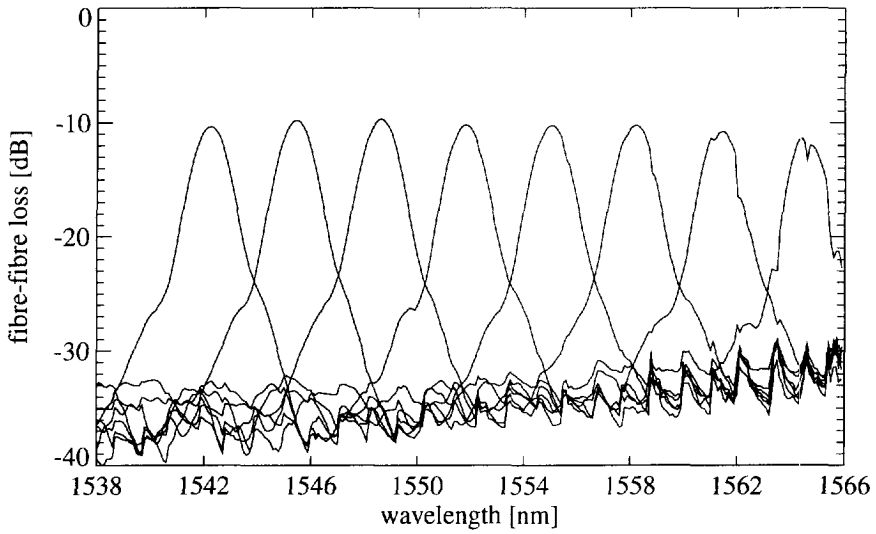


Figure 6.12: Transmission characteristics (fibre-to-fibre loss) of largest ($52 \times 9 \text{ mm}^2$) polymeric Phased Array for TE polarisation.

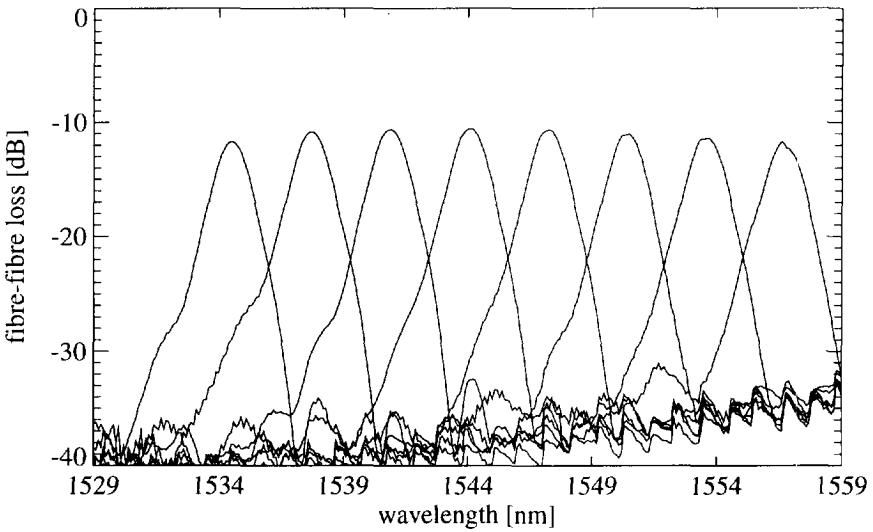


Figure 6.13: Transmission characteristics (fibre-to-fibre loss) of middle ($33 \times 8 \text{ mm}^2$) polymeric Phased Array for TE polarisation.

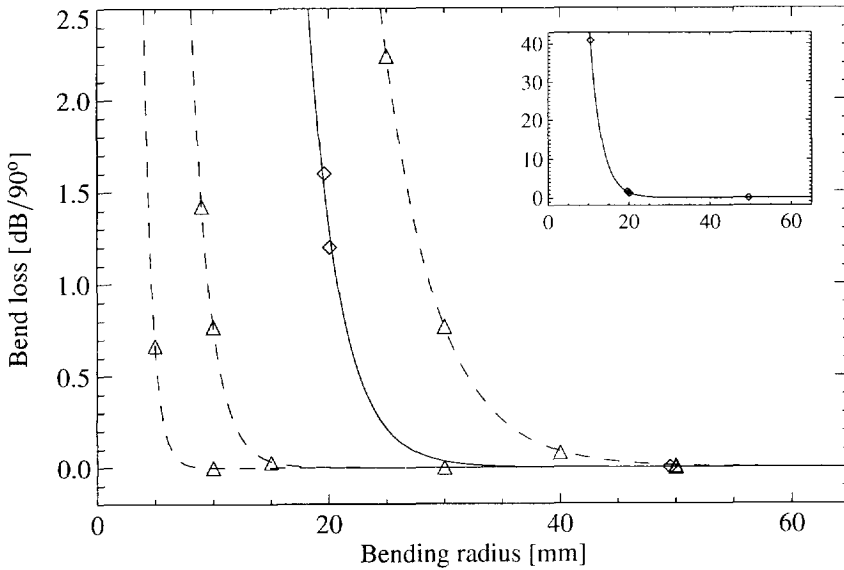


Figure 6.14: Bend loss per 90° measured from some test bends on the chip (solid line, \diamond), compared to calculated values for a number of refractive index contrasts (dashed lines, \triangle ; Left to right: $\Delta N = 0.008, 0.006, 0.004$). The lines through the calculated and measured points are simple exponential fits. The inset shows the measured points over an extended y-range.

temperature. The design value of 1550 nm can easily be reached due to the thermal tunability properties of the polymeric material.

The fibre-to-fibre loss of 10 dB is composed of 6 dB fibre coupling and waveguiding loss and 4 dB phased array loss. The 6 dB has been measured for reference waveguides running alongside the phased array. Assuming a few tenths of a dB coupling loss at each fibre-chip coupling, this measurement indicates the waveguide loss on this 9 cm long chip is about 0.6 dB/cm. The 3 dB remaining loss is in good agreement with the design value.

Measurements for a smaller device are shown in figure 6.13. In this device, losses in the 2 cm radius bends increase the total fibre-to-fibre loss to 11–12 dB. The device has been excited in input 2; the central wavelength is $1553.5 \mu\text{m}$. Obviously, the smaller size of the device allows the chip to be diced back. Reducing the length to 64 mm, and thereby getting rid of some sections of straight waveguide, reduced the fibre-to-fibre loss of the phasor to 7–8 dB.

The smallest device could not be measured due to high bend losses of the 1 cm radius bends caused by the low index contrast of the chip (see figure 6.14). This device did, however, operate in the $1.3 \mu\text{m}$ wavelength region (as well as the others), because bending losses are much lower there. (The light ‘sees’ a 20% larger waveguide core, relative to its own 20% smaller wavelength; this reduces the calculated bending loss of 1 cm bends from 40 to 0.6 dB/cm.) The insertion losses of the devices are slightly smaller than at $1.55 \mu\text{m}$, and the channel spacing is

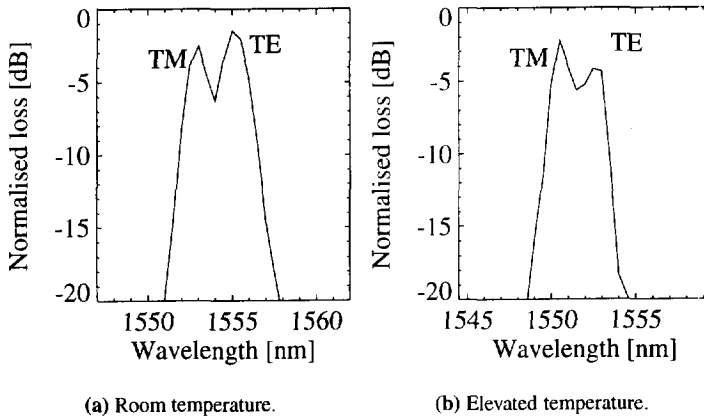


Figure 6.15: TE-TM splitting with linearly polarised light coupled in at an angle of 45° . Left maximum is for TM and right maximum is for TE. The peaks move closer together at elevated temperatures.

obviously different (2.7 nm), because the geometry of the devices was designed for operation at $1.55\mu\text{m}$.

6.4.2 Polarisation dependence

The response peaks of both devices are slightly wider than aimed for in the design, in part because of the small shoulders on the right flanks of the pass-bands. These are caused by residual TE polarised light coupled in. The device was not polarisation independent, as can be seen in figure 6.15(a). The figure shows the TE-TM splitting occurring when linearly polarised light is coupled into the device at an angle of approximately 45° . At room temperature, 2.5 nm of TE-TM shift was observed. When the device was operated at an elevated temperature, the splitting decreased (see figure 6.15(b)), and eventually the two peaks could no longer be discerned separately. It is believed that the splitting is caused by stress-induced birefringence originating from thermal processing steps in combination with the different thermal expansion coefficients of the polymer and the silicon substrate.

6.5 Conclusions

In this chapter, the first Phased Array wavelength demultiplexers in polymeric material have been presented that are suitable for use in the EDFA window (around $1.55\mu\text{m}$). The devices are 8×8 routers with a channel spacing of 3.2 nm. The fibre-to-fibre insertion losses are 8 and 10 dB and the crosstalks are lower than -20dB . A TE-TM shift of 2.5 nm was observed at room temperature due to stress effects.

Chapter 7

Switching by exploiting the wavelength domain

As an example of the application possibilities of phased arrays, space switching experiments of 2.5 Gb/s optical signals by λ -conversion in a DBR laser and subsequent routing through a phased array wavelength multiplexer have been done. Integration of 3 dB couplers and a Phased Array forms the complete passive part of such a space switch.

7.1 Introduction

The ability to spatially switch optical signals is important for efficient, high speed optical networks. An $N \times N$ optical switch can be built from a matrix of 2×2 switches (e.g., Mach-Zehnder or DOS type), but these circuits tend to be complex because the number of switches needed is of order N^2 (e.g., [104]).

In a different concept [105], input signals are fed into a star coupler via tunable wavelength converters, and are selected at the outputs by an array of fixed wavelength filters. Obviously, the complexity of a switch of this type increases only linearly with N . A major drawback of this approach, however, is that most of the available signal power is wasted in the filters.

In this chapter first experiments are presented with a modified version of this concept [106, 107]. The star coupler and filters have been replaced by an $N \times N$ phased array wavelength multiplexer for routing, and wavelength conversion is accomplished by means of DBR lasers. These are kept separately, while the passive components of the switch are integrated on an InGaAsP/InP chip (see figure 7.4).

7.2 Experimental

For the experimental demonstration, first the setup drawn schematically in figure 7.1 has been used to test the concept. Here the chip contains a phased array only. One signal source and

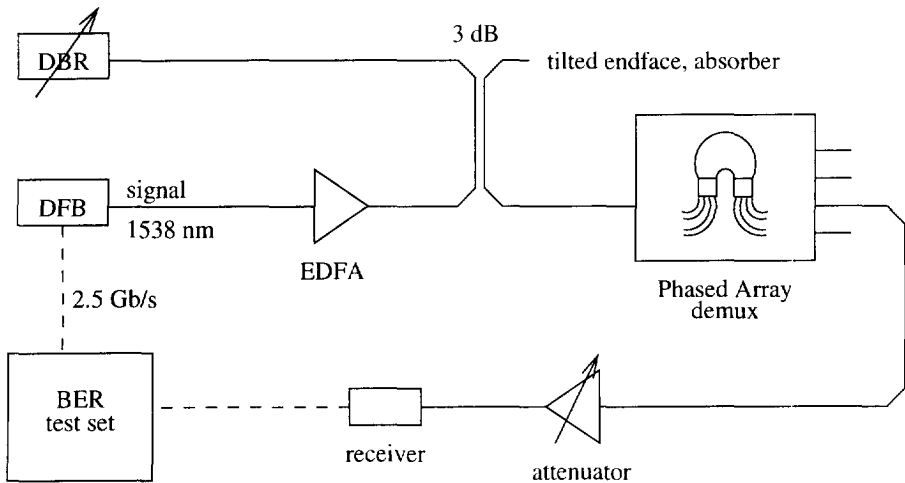


Figure 7.1: Space switching with phased array and external 3 dB coupler. 11.5 dBm of modulated power is supplied to the DBR for wavelength conversion. The DBR is tuned electronically to each of the four phased array channels in turn (figure 7.2), and BER measurements are made (figure 7.3).

one wavelength converter have been used for the demonstration. The source is a DFB laser emitting at 1538 nm, modulated at a rate of 2.5 Gb/s with a 40 mA peak-to-peak drive current. The laser signal power is amplified by an EDFA with adjustable gain (maximum output power +18 dBm).

For the wavelength converter, a current-injection tunable DBR laser with a tuning range of 1546–1554 nm is used [108]. A 3 dB coupler is needed to connect both the signal source and the remainder of the circuit. The light is injected by means of a tapered fibre tip, and about +4 dBm of DBR output power is picked up at a gain current of 65 mA. (Coupling loss \approx 5 dB.)

Using two additional tapered fibre tips, the converted signal is subsequently routed through an InGaAsP/InP chip containing a phased array fabricated in ridge waveguides with zero polarisation dispersion [89]. After an adjustable attenuator, the light from the output of choice is detected by a 2.5 Gb/s receiver.

The phased array has eight outputs with a channel spacing of 2 nm. The transmission characteristics of the four channels covered by the DBR tuning range are plotted in figure 7.2. The fibre-to-fibre loss is 13 dB, and crosstalk between channels is better than -25 dB.

Figure 7.3(a) shows the results of Bit Error Rate measurements. The measurements for the different outputs have been performed by electronically tuning the DBR to the desired wavelength for each of the four phased array channels (figure 7.2), and adjusting the outcoupling fibre tip position. All data have been taken with a pseudo-random bit sequence (PRBS) of length $2^{23} - 1$. For direct detection of the DFB signal, the sensitivity of the system is -23 dBm at a BER of 10^{-9} . The penalty for wavelength conversion and routing through the phased array in the current setup is 3.5 to 4.5 dB.

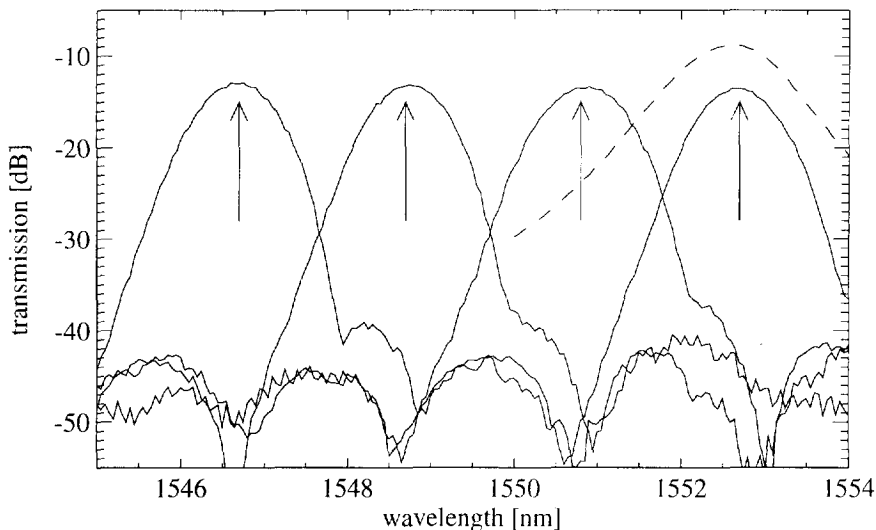


Figure 7.2: Four channels of the phased array covered by the wavelength converter. Fibre-to-fibre loss is 13 dB. Also shown is the transmission of a bulk-optic tunable filter used for reference measurements (dashed curve). Arrows indicate the wavelength of the four outputs of the switch.

For comparison, measurements have been made at two DBR wavelengths also used in the switch, but without routing through the phased array. In this case it is necessary to use a bulk-optic tunable bandpass filter in order to remove the DFB signal at 1538 nm, which is reflected from the uncoated front facet of the DBR laser, and only detect the DBR signal at the converted wavelength. The filter has a transmission characteristic similar to a phased array channel, but its insertion loss is 4 dB less (figure 7.2). The sensitivities are equal to those obtained with the phased array, so it can be concluded that routing of the signal through the phased array introduces no additional penalty.

The second part of the experiments has been performed with the integrated version of the switch (see figure 7.4). The chip is fabricated in the same technology as the phased array discussed above, with the passive components of the circuit in figure 7.1 integrated on it: only connection of DBR wavelength converters is necessary to yield a complete 4×4 switch.

The phased array is similar to the one discussed earlier, but now has a channel spacing of 1 nm to relax the requirements on the DBR tuning range. The chip again is fabricated in a polarisation independent waveguide structure, so no polarisation control is necessary.

Connected to the inputs of the phased array are four power splitters based on the multi-mode interference effect [73]. For coupling with arrays of tapered fibre tips, the connecting waveguides for input signals and wavelength converters, as well as the outputs of the phased array, have been given a pitch of $250 \mu\text{m}$ using waveguide bends with a minimum radius of curvature of $200 \mu\text{m}$. Total size of the chip is $3 \times 5 \text{ mm}^2$; its layout is schematically given in

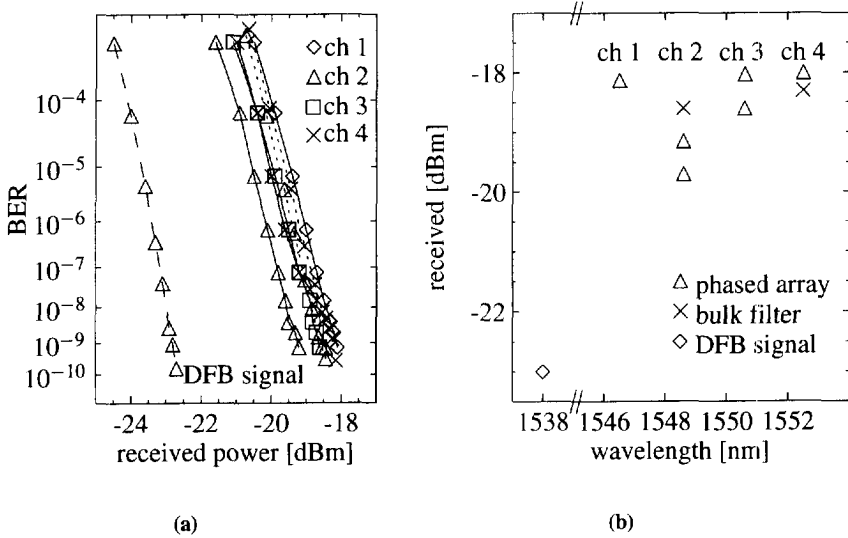


Figure 7.3: BER measurements (a) and sensitivities (b) of the directly detected signal ($\lambda = 1538\text{nm}$, dashed), the routed signal in each of the four states of the switch ($\lambda = 1546.6, 1548.6, 1550.6,$ and 1552.6nm , solid), and wavelength conversion without routing (using a bulk-optic filter, dotted). Some measurements have been repeated to indicate stability, which is better than 0.5dB.

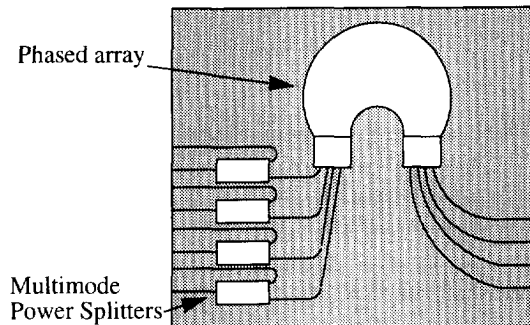


Figure 7.4: Schematic lay-out of InGaAsP chip containing the completely integrated passive part of the wavelength switch: the inputs of a polarisation independent 4×4 phased array with 1 nm channel spacing are connected to multi-mode power splitters.

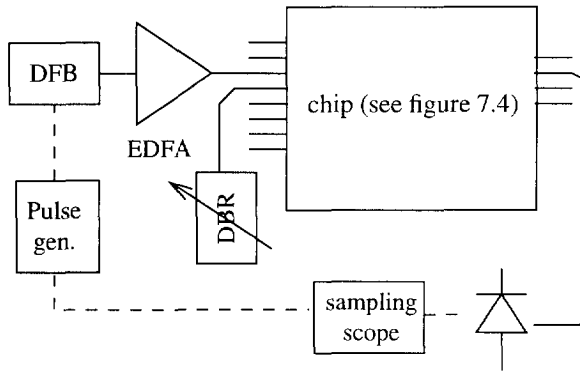


Figure 7.5: The configuration in which the chip of figure 7.4 is used. Signal input and wavelength converter are coupled using an array of tapered fibre tips with a pitch of $250\mu\text{m}$.

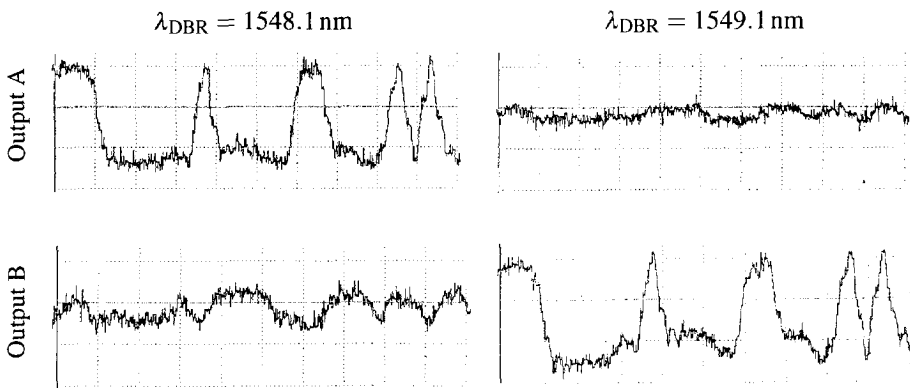


Figure 7.6: Part of a PRBS signal that was detected at two of the outputs of the phased array in the configuration of figure 7.5 (averaged 256 times). When the DBR wavelength is electronically switched between two values, space-switching behaviour is clearly visible. $\lambda_{\text{input}} = 1538\text{ nm}$.

figure 7.4.

Measurements have been made on a setup as shown in figure 7.5. Because the input signal from the EDFA now has to cross two additional fibre-chip couplings (and due to a slightly higher on-chip propagation loss than for the separate phased array), the signal power input to the DBR laser is only $+2.5\text{ dBm}$, as compared to $+11.5\text{ dBm}$ in the first experiment.

Figure 7.6 shows a part of the bit pattern detected by a photodetector and averaged 256 times by a sampling oscilloscope. The figure clearly shows the switching behaviour by observing two switch outputs at two DBR wavelengths. The structure observed in the lower left trace is due to the high power ($+18\text{ dBm}$) input signal at 1538 nm , part of which is transmitted

via the substrate to the outcoupling fibre, which is in this case located in line with the high power input fibre.

7.3 Discussion

Figure 7.3(b) shows the received power level in the system of figure 7.1 in order to achieve a BER of 10^{-9} . The sensitivities of the four channels of the switch, as well as that for transmission through the bulk-optic filter, are within 1 dB from each other. A BER penalty of 4 dB is observed as a result of extinction ratio degradation in the DBR wavelength converter, despite the large signal input power. This is because an off-the-shelf DBR laser with an uncoated front facet has been used for the experiments. (It is known that AR-coating this facet can reduce input power requirements considerably [109].) This is mainly a problem in the experiment with the integrated switch, where a signal power of only 2.5 dBm is available. Operating the DBR laser at a lower gain current lowers the required signal power, but also reduces the available output power. At very low gain, relaxation oscillations appear in the converted signals, degrading the pulse shape.

While large improvements can be made by optimising the DBR laser, the main disadvantage of this approach are the two additional fibre-chip couplings necessary for the signal to reach the wavelength converters. This can, in principle, be solved by integrating the DBR laser on the chip. However, because of easier integration with the phased array, wavelength conversion by means of an asymmetric MZI configuration with SOAs [110] might be a more viable approach. The configuration of figure 7.5 can still be used, but the difference is that now the DBR lasers are used as tunable CW sources instead of converters, and that the signal has to traverse only one instead of three fibre-chip couplings to reach the on-chip converters.

Chapter 8

A multi-wavelength laser

As an example of the application possibilities of Phased Arrays, a compact Phased Array based multi-wavelength laser with 9 channels spaced by 400GHz around a central wavelength of $1.55\mu\text{m}$ has been produced. The component size is $3.5 \times 2.5\text{mm}^2$. Simultaneous operation of four channels is demonstrated.

8.1 Introduction

Wavelength Division Multiplexing (WDM) is widely regarded as a promising option to increase the bandwidth and flexibility of broadband optical communication systems. In such systems, multi-wavelength laser sources, both for selectable single wavelength and simultaneous multiple wavelength operation, will be important components.

Several monolithically integrated solutions have been demonstrated for launching multiple wavelengths into a single fibre, e.g., integration of DFB lasers with a star coupler [111] and including an etched grating [112] or a Phased Array wavelength multiplexer [113, 114] in the laser cavity. The latter two devices have been fabricated using Quantum Well-loaded [113] or Selective Area Epitaxy-grown [114] embedded waveguides. Due to the relatively small index contrast of such waveguides, a rather large device size ($10 \times 4\text{mm}^2$) results. A smaller device size can only be obtained by increasing the index contrast. This chapter presents a device fabricated according to the same principle of including a Phased Array in the laser cavity, but in a ridge waveguide structure that enables use of bending radii down to $500\mu\text{m}$ [115, 116].

8.2 Design and fabrication

As shown schematically in figure 8.1, the passive part of the device consists of an 11×1 Phased Array wavelength multiplexer having a channel spacing of 400GHz (3.2nm), and a free spectral range (FSR) of 38.75nm. Polarisation dependence does not pose a problem,

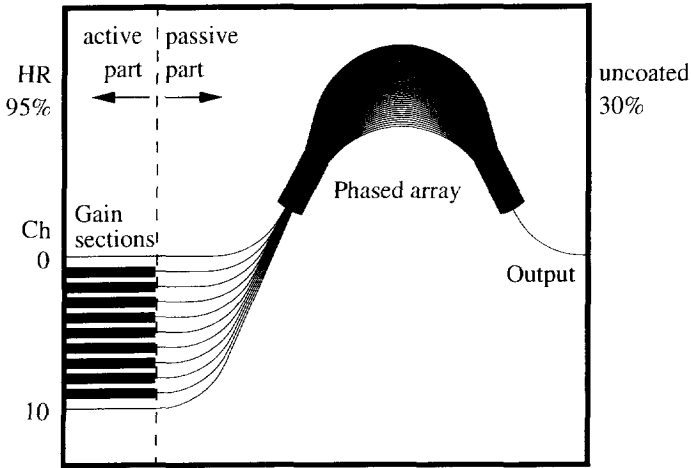


Figure 8.1: Schematic diagram of ridge waveguide multi-wavelength laser chip. The left facet is coated for high reflectivity. The right facet is an uncoated semiconductor-air transition with approximately 30% reflectivity. The waveguide structure used is shown in figure 8.2.

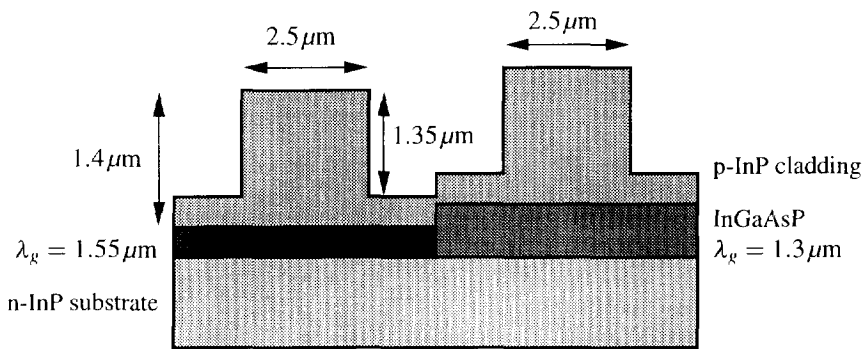


Figure 8.2: Active and passive waveguide structures used for the multi-wavelength laser. The thickness of the active waveguide core on the left is 120nm, while the passive waveguide core on the right is 230nm thick for confinement reasons.

because only TE polarised light will be generated in the device. The large FSR is necessary to avoid having two array orders competing for gain in the bandwidth of the gain sections.

The ridge waveguide structure of the device (shown in figure 8.2) has been chosen for stable TE operation of the gain sections, in combination with the use of small bending radii. The phased array has been optimised for compactness. It comprises 50 array waveguides with a minimum bending radius of $500\mu\text{m}$. The two outer input waveguides are used for testing purposes, while the 9 inner input arms are equipped with $500\mu\text{m}$ long gain sections. Total device size is $3.5 \times 2.5\text{mm}^2$.

In addition to a small device size, the ridge waveguide structure in both the active and passive parts of the device leads to a reasonably simple fabrication scheme. The complete structure (active + passive) is grown in 3 epitaxy steps. A 120 nm thick InGaAsP laser active layer with $\lambda_g = 1.55\mu\text{m}$ is grown onto an n-type InP substrate by means of low-pressure MOVPE. After defining the active regions using wet chemical etching, 230 nm InGaAsP with $\lambda_g = 1.30\mu\text{m}$ is grown, butt-jointed to the active layer, and the entire structure is overgrown with a $1.4\mu\text{m}$ thick 10^{18}cm^{-3} p-doped InP cladding layer.

Stable TE mode operation is obtained using ridges of $2.5\mu\text{m}$ in width and $1.35\mu\text{m}$ in height, which are etched by means of reactive ion etching. Finally, the laser contact metallisation is fabricated, and the back facet is coated for high reflection (95%) using a dielectric coating. For characterisation, the chips are soldered onto copper carriers providing 8 leads for electrical contacts.

8.3 Experimental results

Figure 8.3 shows the response of a discrete, passive Phased Array. The 11 channels have a spacing of 400 GHz around the central wavelength of 1547 nm, with a crosstalk better than -20dB . Fibre-to-fibre insertion loss (using two lensed fibres) is 24.7 dB for the best channel, and increases with channel number due to the increasing path length (see figure 8.1). From this, a waveguide loss of 20 dB/cm is estimated, which is in agreement with the results of Fabry-Pérot contrast measurements on straight waveguides. This relatively high loss is attributed to the p-doped InP cladding layer, which was grown over the entire structure for simplicity of processing in this first run.

The lasing operation of the complete device is shown in figure 8.4. Single-mode operation with a side mode suppression of approximately 20 dB is obtained for 6 out of 8 addressable channels. The width of the individual peaks results from the 0.1 nm resolution of the optical spectrum analyser used for the measurements. Using a self-homodyne technique, the 3 dB linewidth was measured to be 21 MHz. At the rear facet of the device, a ripple of 1.3 dB was measured in the amplified spontaneous emission spectrum of the laser, with a period consistent with the length of the gain sections. This ripple height is reasonably small, and indicative of good quality butt couplings with low reflectance.

The maximum power that was coupled in the fibre is 0.36 mW for channel 4, driven at 200 mA (see figure 8.5). Threshold current for the device, operated at 16°C , is 101 mA for channel 4 and increases to 122 mA for the outer channels (see inset in figure 8.5), due to the

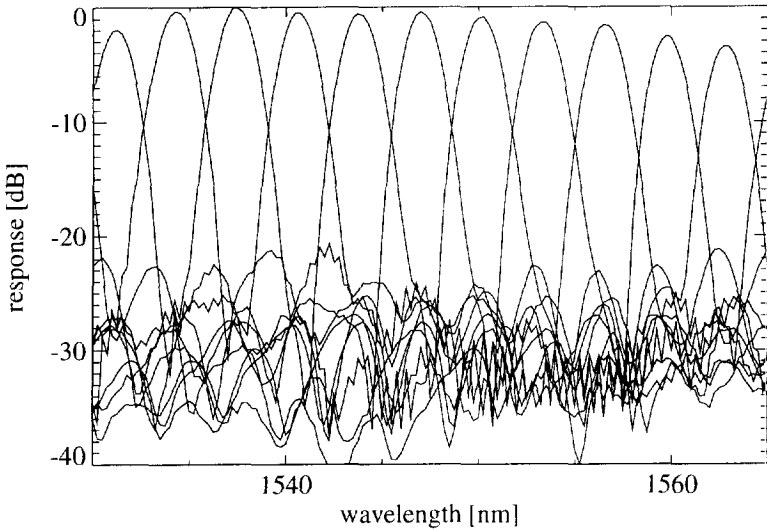


Figure 8.3: Transmission response of a discrete, passive phased array.

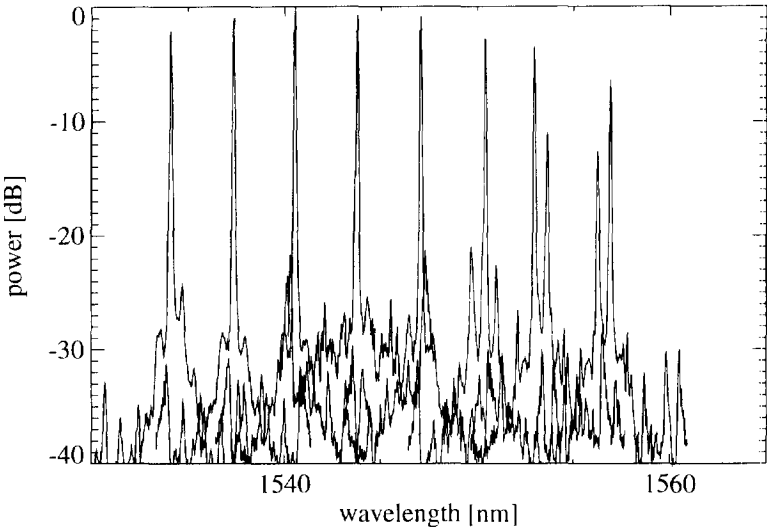


Figure 8.4: Lasing spectra of the individual channels at 10mA above threshold. Six out of eight addressed channels are single mode, with a side mode suppression ratio of 20dB. The channels are spaced 400 ± 10 GHz. The gain blocks laser in the maxima of the transmission peaks of the phased array, shown in figure 8.3.

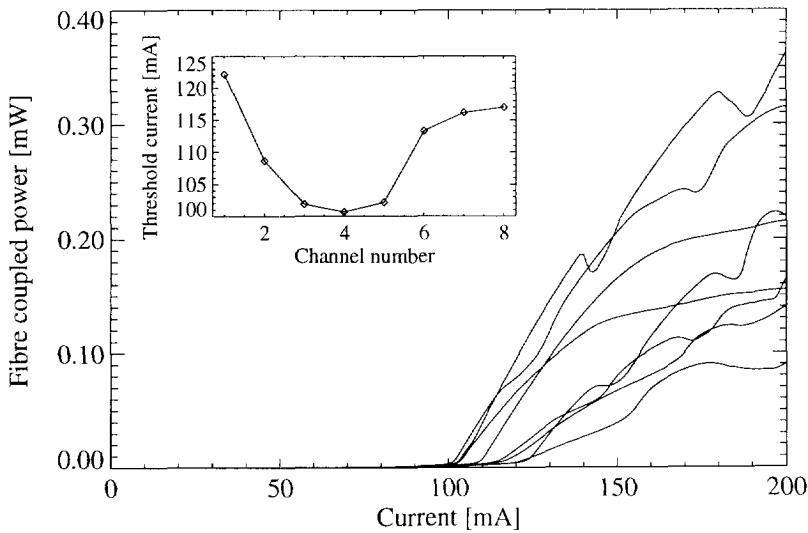


Figure 8.5: L-I curves of the eight channels of the multi-wavelength laser. The middle channel, that experiences the least loss in the phased array, performs best. The inset shows the threshold currents of all channels.

angular loss (see page 91) of the phased array. The increase is not symmetric because of the increasing length of the passive part of the cavity for higher channel numbers.

Discrete laser arrays (i.e., without passive waveguides; length $500\mu\text{m}$) uniformly exhibit threshold currents of 35 mA. This threshold is not higher for discrete lasers with a short length ($500\mu\text{m}$) of passive straight waveguide coupled to them, which is another indication of good quality butt coupling.

The kinks in figure 8.5 are caused by mode hopping (see figure 8.6). Between the four modes of stable operation shown, the coherence of the generated light collapses, and the device hops to the next mode. The mode spacing of approximately 0.06 nm that can be inferred from figure 8.6 is consistent with the cavity length of 6 mm.

The temperature dependence of the device performance is shown in figure 8.7. (Measured with a different device than the other figures, hence the difference in absolute power.) At 16°C , only dual channel lasing could be observed. Stable four channel operation could be obtained at a device temperature of 11°C , as shown in figure 8.8. Device heating resulting from the high operating currents prevented lasing at more wavelengths.

8.4 Discussion

A 9 channel multi-wavelength laser has been fabricated with reasonably good performance, considering this is the first processing run. The most important problem is the high return loss of the wavelength dependent feedback mirror, i.e., the phased array and output facet.

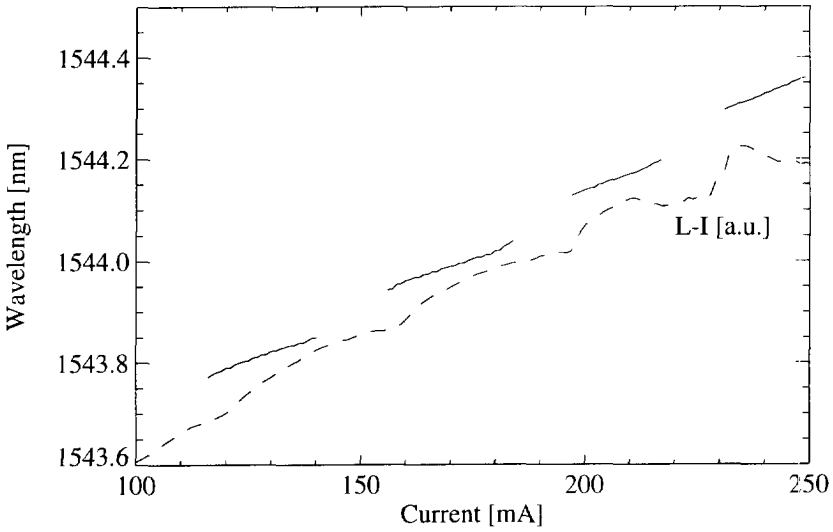


Figure 8.6: Emitted wavelength as a function of pump current for channel 4 of the laser. The curve shows four regions of stable operation between which mode hops of ≈ 0.06 nm occur. These hops can be correlated with kinks in the L-I curve (shown dashed).

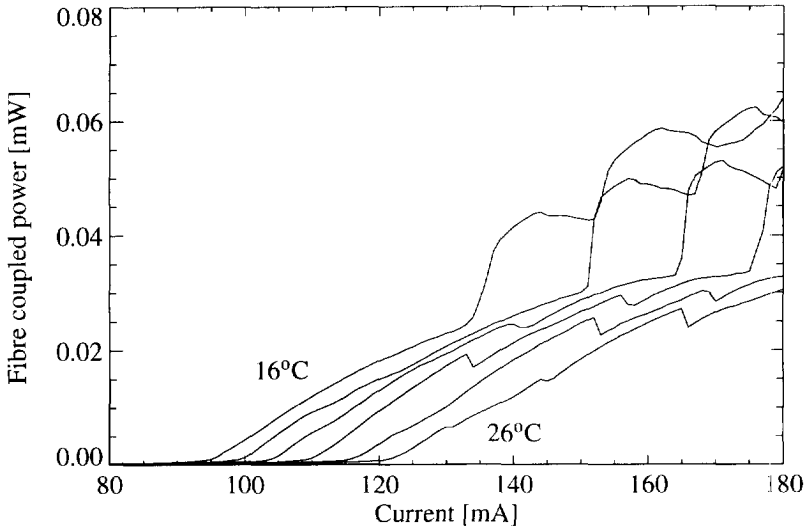


Figure 8.7: Temperature dependence of L-I characteristics (channel 1).

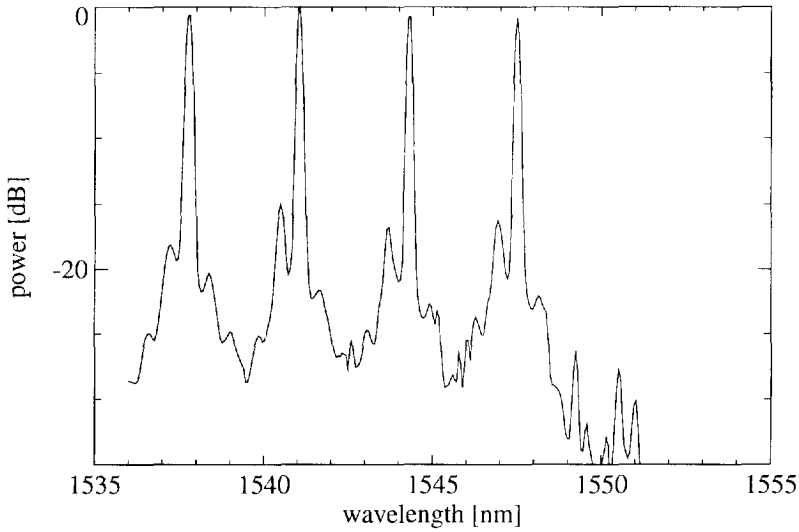


Figure 8.8: Simultaneous four channel operation at 11°C. Total bias current through the chip is 0.5 A.

This is mainly caused by the high waveguide loss, which is probably due to the p-doped InP layer on top of the waveguides. Further development of the fabrication process may alleviate this problem. The easiest method to counteract this high return loss, however, is to add an amplifier in the output waveguide, a method which is also used by Zirngibl [117]. The cross gain modulation in this common amplifier can be suppressed by using a feed-forward drive scheme [118].

References

- [1] T. H. Maiman, "Stimulated optical radiation in ruby," *Nature*, vol. 187, pp. 493–494, Aug. 6 1960.
- [2] I. Hayashi, M. B. Panish, and P. W. Foy, "A low-threshold room-temperature injection laser," *IEEE J. Quantum Electron.*, vol. 5, pp. 211–212, Apr. 1969.
- [3] K. C. Kao and G. A. Hockham, "Dielectric fibre surface waveguides for optical frequencies," *IEE Proc.*, vol. 113, pp. 1151–1158, July 1966.
- [4] F. P. Kapron, D. B. Keck, and R. D. Maurer, "Radiation losses in glass optical waveguides," *Appl. Phys. Lett.*, vol. 17, pp. 423–425, Nov. 15 1970.
- [5] N. Edagawa, I. Morita, M. Suzuki, S. Yamamoto, H. Taga, and S. Akiba, "20Gbit/s, 8100km straight-line single-channel soliton-based RZ transmission experiment using periodic dispersion compensation," in *Proc. 21st Eur. Conf. on Opt. Comm. (ECOC '95), Vol. 3, Post-deadline papers*, (Brussels, Belgium), pp. 983–986, Sept. 17–21 1995.
- [6] H. Onaka, H. Miyata, G. Ishikawa, K. Otsuka, H. Ooi, Y. Kai, S. Kinoshita, M. Seino, H. Nishimoto, and T. Chikama, "1.1 Tb/s WDM transmission over a 150 km 1.3 μ m zero-dispersion single-mode fiber," in *OFC '96 Technical Digest, Post-deadline papers*, (San José, California), Feb. 25–Mar. 1 1996.
- [7] C. A. Brackett, "Dense wavelength division multiplexing networks: Principles and applications," *IEEE J. Select. Areas Commun.*, vol. 8, pp. 948–964, Aug. 1990.
- [8] S. E. Miller, "Integrated optics: An introduction," *Bell Syst. Tech. J.*, vol. 48, pp. 2059–2069, Sept. 1969.
- [9] T. L. Koch and U. Koren, "Photonics integrated circuits: Research curiosity or packaging common sense?," *IEEE Lightwave Comm. Syst.*, vol. 1, pp. 50–56, Nov. 1990.
- [10] E. C. M. Pennings, M. K. Smit, A. A. M. Staring, and G.-D. Khoe, "Integrated-optics versus micro-optics — a comparison," in *Integrated Photonics Research (IPR '96), invited paper*, (Boston, Massachusetts), pp. 460–463, Apr. 29–May 2 1996.
- [11] T. Tamir, ed., *Integrated Optics*. Topics in Applied Physics, Berlin: Springer-Verlag, second ed., 1979.
- [12] R. G. Hunsperger, *Integrated Optics: Theory and Technology*. Springer Series in Optical Sciences, Berlin: Springer-Verlag, second ed., 1984.
- [13] J. Clerk Maxwell, "A dynamical theory of the electromagnetic field," *Philosophical transactions of the Royal Society of London*, vol. 155, pp. 459–512, 1865. London, Taylor and Francis.

- [14] R. P. Feynman, *The Feynman Lectures on Physics*, vol. II, ch. 32. Reading, Massachusetts: Addison-Wesley, 1964.
- [15] J. Chilwell and I. Hodgkinson, "Thin-films field-transfer matrix theory of planar multilayer waveguides and reflection from prism-loaded waveguides," *J. Opt. Soc. Am. A*, vol. 1, pp. 742–753, July 1984.
- [16] B. M. A. Rahman, F. A. Fernandez, and J. B. Davies. "Review of finite element methods for microwave and optical waveguides," *Proc. IEEE*, vol. 79, pp. 1442–1448, Oct. 1991.
- [17] J.-S. Gu, *Numerical Analysis of Directionally Varying Optical Waveguides*. PhD thesis, Swiss Federal Institute of Technology, Zürich, Switzerland, 1991.
- [18] R. M. Knox and P. P. Toullos, "Integrated circuits for the millimeter through optical frequency range," in *Proc. Symp. on Submillimeter Waves* (J. Fox, ed.), vol. XX of *Microwave Research Institute symposia series*, (New York), pp. 497–516, Polytechnic press, Mar. 31–Apr. 2 1970.
- [19] Working Group I, COST 216, "Comparison of different modelling techniques for longitudinally invariant integrated optical waveguides," *IEE Proc., Pt. J*, vol. 136, pp. 273–280, Oct. 1989.
- [20] M. Heiblum and J. H. Harris, "Analysis of curved optical waveguides by conformal transformation," *IEEE J. Quantum Electron.*, vol. 11, pp. 75–83, Feb. 1975. with correction vol. 12 p. 313.
- [21] H. Kogelnik, "Theory of dielectric waveguides," in Tamir [11], ch. 2.
- [22] R. E. Nahory, M. A. Pollack, W. D. Johnston, Jr., and R. L. Barns, "Band gap versus composition and demonstration of Vegard's law for $\text{In}_{1-x}\text{Ga}_x\text{As}_y\text{P}_{1-y}$ lattice matched to InP," *Appl. Phys. Lett.*, vol. 33, pp. 659–661, Oct. 1978.
- [23] F. Fiedler and A. Schlachetzki, "Optical parameters of InP-based waveguides," *Solid State Electron.*, vol. 30, no. 1, pp. 73–83, 1987.
- [24] I. Moerman, *Reaktoroptimalizatie en Procesontwikkeling voor Metaalorganische Gasfase Epitaxie van InGaAsP/InP-Structuren*. PhD thesis, University of Gent, Gent, Belgium, 1992.
- [25] R. G. Walker, "Simple and accurate loss measurement technique for semiconductor optical waveguides," *Electron. Lett.*, vol. 21, pp. 581–583, June 1985.
- [26] L. S. Yu, Q. Z. Liu, S. A. Pappert, P. K. L. Yu, and S. S. Lau. "Laser spectral linewidth dependence on waveguide loss measurements using the Fabry-Pérot method," *Appl. Phys. Lett.*, vol. 64, pp. 536–538, Jan. 1994.
- [27] J. Buus, "Analytical approximation for the reflectivity of DH lasers," *IEEE J. Quantum Electron.*, vol. QE-17, pp. 2256–2257, Dec. 1981.
- [28] L. H. Spiekman, "Optimization of the Fabry-Pérot setup." Internal report, Integrated Optics group, TU Delft, 1992.
- [29] R. J. Deri and E. Kapon, "Low-loss III-V semiconductor optical waveguides," *IEEE J. Quantum Electron.*, vol. 27, pp. 626–640, Mar. 1991.
- [30] R. Braunstein and E. O. Kane, "The valence band structure of the III-V compounds," *J. Phys. Chem. Solids*, vol. 23, pp. 1423–1431, 1962.
- [31] G. W. Iseler, "Properties of InP doped with Fe, Cr or Co," in *Proc. 7th Int. Symp. GaAs and Related Compounds* (C. M. Wolfe, ed.), (London), pp. 144–153, The Institute of Physics, 1978. Inst. Phys. Conf. Ser. No. 45.

- [32] C. Bornholdt, W. Döldissen, D. Franke, N. Grote, J. Krauser, U. Niggebrügge, H. P. Nolting, M. Schlak, and I. Tiedke, "Passive optical GaInAsP/InP waveguides," *Electron. Lett.*, vol. 19, pp. 81–82, Feb. 1983.
- [33] H.-G. Unger, *Planar optical waveguides and fibres*. Oxford: Clarendon Press, 1977.
- [34] P. K. Tien, "Light waves in thin films and integrated optics," *Appl. Opt.*, vol. 10, pp. 2395–2413, Nov. 1971.
- [35] P. Beckmann and A. Spizzichino, *The Scattering of Electromagnetic Waves from Rough Surfaces*. Oxford: Pergamon Press, 1963.
- [36] F. Ladouceur, J. D. Love, and T. J. Senden, "Measurement of surface roughness in buried channel waveguides," *Electron. Lett.*, vol. 28, pp. 1321–1322, July 1992.
- [37] R. C. Hewson-Browne, P. C. Kendall, and D. A. Quinney, "Roughness scattering into substrate radiation modes of rib waveguides," *IEE Proc., Pt. J*, vol. 136, pp. 281–286, Oct. 1989.
- [38] A. Yariv and P. Yeh, *Optical Waves in Crystals*. New York: John Wiley & Sons, 1984.
- [39] R. J. Deri, R. J. Hawkins, and E. Kapon, "Rib profile effects on scattering in semiconductor optical waveguides," *Appl. Phys. Lett.*, vol. 53, pp. 1483–1485, Oct. 1988.
- [40] Y. S. Oei, L. H. Spiekman, F. H. Groen, I. Moerman, E. G. Metaal, and J. W. Pedersen, "Novel RIE-process for high quality InP-based waveguide structures," in *Proc. 7th Eur. Conf. on Integr. Opt. (ECIO '95)*, (Delft, The Netherlands), pp. 205–208, Apr. 3–6 1995.
- [41] I. Adesida, K. Nummala, E. Andideh, J. Hughes, C. Caneau, R. Bhat, and R. Holmstrom, "Nano-structure fabrication in InP and related compounds," *J. Vac. Sci. Technol. B*, vol. 8, pp. 1357–1360, Nov./Dec. 1990.
- [42] S. E. Hicks, C. D. W. Wilkinson, G. F. Doughty, A. L. Burness, I. Henning, M. Asghari, and I. White, "Reactive ion etching of low-loss mirrors in InP/InGaAsP/InP heterostructure mirrors using CH₄/H₂/O₂ chemistry," in *Proc. 6th Eur. Conf. on Integr. Opt. (ECIO '93)*, (Neuchâtel, Switzerland), Apr. 18–22 1993.
- [43] Y. S. Oei, C. van Dam, F. P. van Ham, L. H. Spiekman, B. H. Verbeek, F. H. Groen, E. G. Metaal, and J. W. Pedersen, "Improved RIE technique for controlled roughness and anisotropy in InP based devices," in *Proc. SOTAPOCS XVIII*, (Honolulu, Hawaii), pp. 134–141, May 16–21 1993.
- [44] L. H. Spiekman, F. P. G. M. van Ham, M. Kroonwijk, Y. S. Oei, J. J. G. M. van der Tol, F. H. Groen, and G. Coudenys, "A new fabrication process for very low-loss narrow-width InGaAsP/InP waveguides," in *Proc. 6th Eur. Conf. on Integr. Opt. (ECIO '93)*, (Neuchâtel, Switzerland), pp. 2.30–2.31, Apr. 18–22 1993.
- [45] T. M. Benson, "Etched-wall bent-guide structure for integrated optics in the III-V semiconductors," *J. Lightwave Technol.*, vol. 2, no. 1, pp. 31–34, 1984.
- [46] E. A. J. Marcetili, "Bends in optical dielectric guides," *Bell Syst. Tech. J.*, vol. 48, pp. 2103–2132, Sept. 1969.
- [47] L. H. Spiekman, Y. S. Oei, E. G. Metaal, F. H. Groen, P. Demeester, and M. K. Smit, "Ultrasmall waveguide bends: the corner mirrors of the future?," *IEE Proc.,-Optoelectron., special issue on Semiconductor Optoelectronics*, vol. 142, pp. 61–65, Feb. 1995. Also presented at Semiconductor and Integrated Opto-electronics (SIOE '94), Cardiff, UK, March 28–30, 1994.

- [48] A. L. Burness, P. H. Loosemore, S. N. Judge, I. D. Henning, S. E. Hicks, G. F. Doughty, M. Asghari, and I. White, "Low loss mirrors for InP/InGaAsP waveguides," *Electron. Lett.*, vol. 29, pp. 520–521, Mar. 1993.
- [49] E. Gini, G. Guekos, and H. Melchior, "Low loss corner mirrors with 45° deflection angle for integrated optics," *Electron. Lett.*, vol. 28, pp. 499–501, Feb. 1992.
- [50] R. van Roijen, G. L. A. van der Hofstad, M. Groten, J. M. M. van der Heyden, P. J. A. Thijs, and B. H. Verbeek, "Fabrication of low-loss integrated optical corner mirrors," *Appl. Opt.*, vol. 32, pp. 3246–3248, June 1993.
- [51] B. H. Verbeek, E. C. M. Pennings, J. W. M. van Uffelen, and P. J. A. Thijs, "Fabrication and analysis of low-loss InGaAsP/InP optical waveguides with extremely small bends," in *Proc. 15th Eur. Conf. on Opt. Comm. (ECOC '89), Post-deadline papers*, (Göteborg), pp. 78–81, Sept. 10–14 1989.
- [52] E.-G. Neumann, "Curved dielectric optical waveguides with reduced transition losses," *IEE Proc., Pt. H*, vol. 129, no. 5, pp. 278–280, 1982.
- [53] E. C. M. Pennings, R. J. Deri, and R. J. Hawkins, "Simple method for estimating usable bend radii of deeply etched optical rib waveguides," *Electron. Lett.*, vol. 27, pp. 1532–1533, Aug. 1991.
- [54] Lord Rayleigh, "The problem of the whispering gallery," *The London, Edinburgh, and Dublin philosophical magazine and journal of science, Series 6*, vol. 20, pp. 1001–1004. 1910.
- [55] C. van Dam, L. H. Spiekman, F. P. G. M. van Ham, F. H. Groen, J. J. G. M. van der Tol, I. Moerman, W. W. Pascher, M. Hamacher, H. Heidrich, C. M. Weinert, and M. K. Smit, "Novel compact InP-based polarisation converters using ultra short bends," in *Integrated Photonics Research (IPR '96)*, (Boston, Massachusetts), pp. 468–471, Apr. 29–May 2 1996.
- [56] C. van Dam, *InP-based polarisation independent wavelength demultiplexers*. PhD thesis, Delft University of Technology, Delft, The Netherlands, to appear in 1997.
- [57] L. B. Soldano, F. B. Veerman, M. K. Smit, B. H. Verbeek, A. H. Dubost, and E. C. M. Pennings, "Planar monomode optical couplers based on multimode interference effects," *J. Lightwave Technol.*, vol. 10, pp. 1843–1850. Dec. 1992.
- [58] L. B. Soldano and E. C. M. Pennings, "Optical multi-mode interference devices based on self-imaging: Principles and applications," *J. Lightwave Technol.*, vol. 13, pp. 615–627, Apr. 1995.
- [59] J. E. Zucker, K. L. Jones, T. H. Chiu, B. Tell, and K. Brown-Goebeler, "Polarization-independent electro-optic waveguide switch using strained InGaAs/InP quantum wells," in *Integrated Photonics Research (IPR '92), Post-deadline papers*, (New Orleans, Louisiana), pp. 21–24, Apr. 13–16 1992.
- [60] M. Bachmann, M. K. Smit, P. A. Besse, E. Gini, H. Melchior, and L. B. Soldano, "Polarization-insensitive low-voltage optical waveguide switch using InGaAsP/InP four-port Mach-Zehnder interferometer," in *OFC/IOOC '93 Technical Digest, Volume 4*, (San José, California), pp. 32–33, Feb. 21–26 1993.
- [61] R. M. Jenkins, J. M. Heaton, D. R. Wight, J. T. Parker, J. C. H. Birbeck, G. W. Smith, and K. P. Hilton, "Novel $1 \times N$ and $N \times N$ integrated optical switches using self-imaging multimode GaAs/AlGaAs waveguides," *Appl. Phys. Lett.*, vol. 64, pp. 684–686, Feb. 1994.

- [62] X. Leijtens, G. W. Yoffe, J. E. M. Haverkort, F. Karouta, J. Brubach, T. Eijkemans, L. M. F. Kaufmann, M. K. Smit, J. A. A. Stegemann, Y. C. Zhu, and J. H. Wolter, " 2×2 Mach-Zehnder interferometric switch based on hetero-*n-i-p-i* quantum wells," *Appl. Phys. Lett.*, vol. 66, pp. 2736–2738, May 1995.
- [63] C. Rolland, R. S. Moore, F. Shepherd, and G. Hillier, "10 Gbit/s, $1.56\mu\text{m}$ multi-quantum well InP/InGaAsP Mach-Zehnder optical modulator," *Electron. Lett.*, vol. 29, pp. 471–472, Mar. 1993.
- [64] R. van Roijen, E. C. M. Pennings, M. J. N. van Stralen, T. van Dongen, B. H. Verbeek, and J. M. M. van der Heijden, "Compact InP-based ring lasers employing multimode interference couplers and combiners," *Appl. Phys. Lett.*, vol. 64, pp. 1753–1755, Apr. 1994.
- [65] T. Krauss, R. M. DeLaRue, I. Gontijo, P. J. R. Laybourn, and J. S. Roberts, "Strip-loaded semiconductor ring lasers employing multimode interference output couplers," *Appl. Phys. Lett.*, vol. 64, pp. 2788–2790, May 1994.
- [66] E. C. M. Pennings, R. van Roijen, M. J. N. van Stralen, P. J. de Waard, R. G. M. P. Koumans, and B. H. Verbeek, "Reflection properties of multimode interference devices," *IEEE Photon. Technol. Lett.*, vol. 6, pp. 715–718, June 1994.
- [67] R. J. Deri, E. C. M. Pennings, A. Scherer, A. S. Gozdz, C. Caneau, N. C. Andreadakis, V. Shah, L. Curtis, R. J. Hawkins, J. B. D. Soole, and J.-I. Song, "Ultracompact monolithic integration of balanced, polarization diversity photodetectors for coherent lightwave receivers," *IEEE Photon. Technol. Lett.*, vol. 4, pp. 1238–1240, Nov. 1992.
- [68] E. C. M. Pennings, R. J. Deri, R. Bhat, T. R. Hayes, and N. C. Andreadakis, "Ultracompact, all-passive optical 90° -hybrid on InP using self-imaging," *IEEE Photon. Technol. Lett.*, vol. 5, pp. 701–703, June 1993.
- [69] M. Bachmann, P. A. Besse, and H. Melchior, "General self-imaging properties in $N \times N$ multimode interference couplers including phase relations," *Appl. Opt.*, vol. 33, pp. 3905–3911, June 1994.
- [70] P. A. Besse, M. Bachmann, H. Melchior, L. B. Soldano, and M. K. Smit, "Optical bandwidth and fabrication tolerances of multimode interference couplers," *J. Lightwave Technol.*, vol. 12, pp. 1004–1009, June 1994.
- [71] M. K. Smit, C. G. M. Vreeburg, and L. H. Spiekman, "Compact components for semiconductor photonic switches," in *Photonics in Switching (PS '96), Invited papers*, (Sendai, Japan), pp. 74–75, Apr. 21–25 1996.
- [72] E. C. M. Pennings, R. J. Deri, A. Scherer, R. Bhat, T. R. Hayes, N. Andreadakis, M. K. Smit, and R. J. Hawkins, "Ultra-compact, low-loss directional coupler structures on InP for monolithic integration," in *Proc. 17th Eur. Conf. on Opt. Comm. (ECOC '91)*, (Paris), pp. 405–408, Sept. 9–12 1991.
- [73] L. B. Soldano, M. Bouda, M. K. Smit, and B. H. Verbeek, "New small-size single-mode optical power splitter based on multi-mode interference," in *Proc. 18th Eur. Conf. on Opt. Comm. (ECOC '92)*, (Berlin), pp. 465–468, Sept. 27–Oct. 1 1992.
- [74] C. F. Janz, B. P. Keyworth, W. Allegretto, R. I. MacDonald, M. Fallahi, G. Hillier, and C. Rolland, "Mach-Zehnder switch using an ultra-compact directional coupler in a strongly-confining rib structure," *IEEE Photon. Technol. Lett.*, vol. 6, pp. 981–983, Aug. 1994.
- [75] L. H. Spiekman, Y. S. Oei, E. G. Metaal, F. H. Groen, I. Moerman, and M. K. Smit, "Extremely small multimode interference couplers and ultrashort bends on InP by deep etching," *IEEE Photon. Technol. Lett.*, vol. 6, pp. 1008–1010, Aug. 1994.

- [76] L. H. Spiekman, Y. S. Oei, E. G. Metaal, F. H. Groen, I. Moerman, M. K. Smit, and B. H. Verbeek, "Extremely small fabrication tolerant InP-based power-splitting and combining structures by deep etching," in *Proc. 20th Eur. Conf. on Opt. Comm. (ECOC '94)*, Vol. 2, (Firenze, Italy), pp. 665–668, Sept. 25–29 1994.
- [77] O. Bryngdahl, "Image formation using self-imaging techniques," *J. Opt. Soc. Am.*, vol. 63, pp. 416–419, Apr. 1973.
- [78] R. Ulrich and G. Ankele, "Self-imaging in homogeneous planar optical waveguides," *Appl. Phys. Lett.*, vol. 27, pp. 337–339, Sept. 1975.
- [79] L. B. Soldano, *Multimode Interference Couplers, Design and Applications*. PhD thesis, Delft University of Technology, Delft, The Netherlands, 1994. ISBN 90-407-1044-9.
- [80] R. Ulrich and T. Kamiya, "Resolution of self-images in planar optical waveguides," *J. Opt. Soc. Am.*, vol. 68, pp. 583–592, May 1978.
- [81] M. K. Smit, "Branching, radiative and self-imaging elements for use in $M \times N$ couplers," in *Proc. 6th Eur. Conf. on Integr. Opt. (ECIO '93)*, (Neuchâtel, Switzerland), pp. 14.1–14.3, Apr. 18–22 1993.
- [82] P. A. Besse, E. Gini, M. Bachmann, and H. Melchior, "New 1×2 multi-mode interference couplers with free selection of power splitting ratios," in *Proc. 20th Eur. Conf. on Opt. Comm. (ECOC '94)*, (Firenze, Italy), pp. 669–672, Sept. 25–29 1994.
- [83] E. C. M. Pennings, R. van Roijen B. H. Verbeek, R. J. Deri, and L. B. Soldano, "Ultracompact multimode interference waveguide devices," in *Annual Meeting of the IEEE Lasers and Electro-Optics Society*, (San José, California), Nov. 1993. Invited paper IO2.1.
- [84] E. C. M. Pennings, *Bends in Optical Ridge Waveguides, Modeling and Experiments*. PhD thesis, Delft University of Technology, Delft, The Netherlands, 1990. ISBN 90-9003413-7.
- [85] M. Smit, "New focusing and dispersive planar component based on an optical phased array," *Electron. Lett.*, vol. 24, no. 7, pp. 385–386, 1988.
- [86] M. R. Amersfoort, *Phased-array wavelength demultiplexers and their integration with photo-detectors*. PhD thesis, Delft University of Technology, Delft, The Netherlands, 1994. ISBN 90-407-1041-4.
- [87] E. Gini and H. Melchior, "Polarization independent InP grating spectrograph for fiber optical links," in *Proc. 7th Eur. Conf. on Integr. Opt. (ECIO '95)*, (Delft, The Netherlands), pp. 279–282, Apr. 3–6 1995.
- [88] H. Takahashi, Y. Hibino, and I. Nishi, "Polarization-insensitive arrayed-waveguide grating wavelength multiplexer on silicon," *Opt. Lett.*, vol. 17, pp. 499–501, Apr. 1992.
- [89] B. H. Verbeek, A. A. M. Staring, E. J. Jansen, R. van Roijen, J. J. M. Binsma, T. van Dongen, M. R. Amersfoort, C. van Dam, and M. K. Smit, "Large bandwidth polarisation independent and compact 8 channel PHASAR demultiplexer/filter," in *OFC/IOOC '94 Technical Digest, Post-deadline papers*, (San Jose, California), pp. 63–66, Feb. 20–25 1994.
- [90] M. R. Amersfoort, J. B. D. Soole, H. P. LeBlanc, N. C. Andreadakis, A. Rajhel, C. Caneau, M. A. Koza, R. Bhat, C. Youtsey, and I. Adesida, "Polarization-independent InP-arrayed waveguide filter using square cross-section waveguides," in *OFC '96 Technical Digest, Volume 2*, (San José, California), pp. 101–102, Feb. 25–Mar. 1 1996.

- [91] A. R. Vellekoop and M. K. Smit, "Four-channel integrated-optic wavelength demultiplexer with weak polarization dependence," *J. Lightwave Technol.*, vol. 9, pp. 310–314, Mar. 1991.
- [92] M. K. Smit, *Integrated Optics in silicon-based aluminum oxide*. PhD thesis, Delft University of Technology, Delft, The Netherlands, 1991. ISBN 90-9004261-X.
- [93] M. Zirngibl, C. H. Joyner, L. W. Stulz, T. Gaiffe, and C. Dragone, "Polarization independent 8×8 waveguide grating multiplexer on InP," *Electron. Lett.*, vol. 29, pp. 201–202, Jan. 1993.
- [94] L. H. Spiekman, F. P. G. M. van Ham, A. Kuntze, J. W. Pedersen, P. Demeester, and M. K. Smit, "Polarization-independent InP-based phased-array wavelength demultiplexer with flattened wavelength response," in *Proc. 20th Eur. Conf. on Opt. Comm. (ECOC '94)*, Vol. 2, (Firenze, Italy), pp. 759–762, Sept. 25–29 1994.
- [95] L. H. Spiekman, A. H. de Vreede, F. P. G. M. van Ham, A. Kuntze, J. J. G. M. van der Tol, P. Demeester, and M. K. Smit, "Flattened response ensures polarization independence of InGaAsP/InP phased array wavelength demultiplexer," in *Proc. 7th Eur. Conf. on Integr. Opt. (ECIO '95)*, (Delft, The Netherlands), pp. 517–520, Apr. 3–6 1995.
- [96] L. H. Spiekman, M. R. Amersfoort, A. H. de Vreede, F. P. G. M. van Ham, A. Kuntze, J. W. Pedersen, P. Demeester, and M. K. Smit, "Design and realization of polarization independent phased array wavelength demultiplexers using different array orders for TE and TM," *J. Lightwave Technol., Special Issue on Multiwavelength Optical Technology and Networks*, vol. 14, pp. 991–995, June 1996.
- [97] M. R. Amersfoort, C. R. de Boer, F. P. G. M. van Ham, M. K. Smit, P. Demeester, J. J. G. M. van der Tol, and A. Kuntze, "Phased-array wavelength demultiplexer with flattened wavelength response," *Electron. Lett.*, vol. 30, pp. 300–302, Feb. 1994.
- [98] K. Okamoto and H. Yamada, "Arrayed-waveguide grating multiplexer with flat spectral response," *Opt. Lett.*, vol. 20, pp. 43–45, Jan. 1995.
- [99] Y. Hida, Y. Inoue, and S. Imamura, "Polymeric arrayed-waveguide grating multiplexer operating around $1.3 \mu\text{m}$," *Electron. Lett.*, vol. 30, pp. 959–960, June 1994.
- [100] L. H. Spiekman, M. B. J. Diemeer, T. H. Hoekstra, and M. K. Smit, "First polymeric phased array wavelength demultiplexer operating at 1550nm ," in *Integrated Photonics Research (IPR '96)*, (Boston, Massachusetts), pp. 36–39, Apr. 29–May 2 1996.
- [101] M. B. J. Diemeer, L. H. Spiekman, R. Ramsamoedj, and M. K. Smit, "Polymeric phased array wavelength multiplexer operating around 1550nm ," *Electron. Lett.*, 1996. Accepted for publication.
- [102] H. M. M. Klein Koerkamp, M. C. Donckers, B. H. M. Hams, and W. H. G. Horsthuis, "Design and fabrication of a pigtailed thermo-optic 1×2 switch," in *Integrated Photonics Research (IPR '94)*, (San Francisco, California), pp. 274–276, 1994.
- [103] W. Pascher and R. Pregla, "Vectorial analysis of bends in optical strip waveguides by the method of lines," *Radio Science*, vol. 28, no. 6, pp. 1229–1233, 1993.
- [104] M. Okuno, K. Katoh, S. Suzuki, Y. Ohmori, and A. Himeno, "Strictly nonblocking 16×16 matrix switch using silica-based planar lightwave circuits," in *Proc. 20th Eur. Conf. on Opt. Comm. (ECOC '94)*, *Post-deadline papers*, (Firenze, Italy), pp. 83–87, Sept. 25–29 1994.
- [105] J. M. Gabriagues and J. B. Jacob, "Exploitation of the wavelength domain for photonic switching in the IBCN," in *Proc. 17th Eur. Conf. on Opt. Comm. (ECOC '91)*, *Invited papers*, (Paris), pp. 59–66, Sept. 9–12 1991.

- [106] L. H. Spiekman, A. A. M. Staring, C. van Dam, E. J. Jansen, J. J. M. Binsma, M. K. Smit, and B. H. Verbeek, "Space-switching using wavelength conversion at 2.5 Gb/s and integrated phased array routing," in *Proc. 21st Eur. Conf. on Opt. Comm. (ECOC '95)*, Vol. 3, Post-deadline papers, (Brussels, Belgium), pp. 1055–1058, Sept. 17–21 1995.
- [107] A. A. M. Staring, L. H. Spiekman, C. van Dam, E. J. Jansen, J. J. M. Binsma, M. K. Smit, and B. H. Verbeek, "Space-switching 2.5 Gbit/s signals using wavelength conversion and phased array routing," *Electron. Lett.*, vol. 32, pp. 377–379, 15th Feb. 1996.
- [108] A. A. M. Staring, J. J. M. Binsma, P. I. Kuindersma, E. J. Jansen, P. J. A. Thijs, T. van Dongen, and G. F. G. Depovere, "Wavelength-independent output power from an injection-tunable DBR laser," *IEEE Photon. Technol. Lett.*, vol. 6, pp. 147–149, Feb. 1994.
- [109] C. Braagaard, B. Mikkelsen, T. Durhuus, and K. E. Stubkjaer, "Modeling the DBR laser used as wavelength conversion device," *J. Lightwave Technol.*, vol. 12, pp. 943–951, June 1994.
- [110] N. Vodjdani, F. Ratovelomanana, A. Enard, G. Glastre, D. Rondi, R. Blondeau, T. Durhuus, C. Jørgensen, B. Mikkelsen, K. E. Stubkjaer, P. Pagnod, and R. Baets, "All optical wavelength conversion at 5 Gbit/s with monolithic integration of semiconductor optical amplifiers in a passive asymmetric Mach-Zehnder interferometer," in *Proc. 20th Eur. Conf. on Opt. Comm. (ECOC '94)*, Post-deadline papers, (Firenze, Italy), pp. 95–99, Sept. 25–29 1994.
- [111] M. G. Young, U. Koren, B. I. Miller, M. A. Newkirk, M. Chien, M. Zirngibl, C. Dragone, B. Tell, H. M. Presby, and G. Raybon, "A 16×1 wavelength division multiplexer with integrated distributed Bragg reflector lasers and electroabsorption modulators," *IEEE Photon. Technol. Lett.*, vol. 5, pp. 908–910, Aug. 1993.
- [112] K. R. Poguntke, J. B. D. Soole, A. Scherer, H. P. LeBlanc, C. Caneau, R. Bhat, and M. A. Koza, "Simultaneous multiple wavelength operation of a multistripe array grating integrated cavity laser," *Appl. Phys. Lett.*, vol. 62, pp. 2024–2026, Apr. 1993.
- [113] M. Zirngibl and C. N. Joyner, "12 frequency WDM laser based on a transmissive waveguide grating router," *Electron. Lett.*, vol. 30, pp. 701–702, Apr. 1994.
- [114] C. H. Joyner, M. Zirngibl, and J. C. Centanni, "An 8-channel digitally tunable transmitter with electroabsorption modulated output by selective-area epitaxy," *IEEE Photon. Technol. Lett.*, vol. 7, pp. 1013–1015, Sept. 1995.
- [115] L. H. Spiekman, A. A. M. Staring, J. J. M. Binsma, E. J. Jansen, T. van Dongen, P. J. A. Thijs, M. K. Smit, and B. H. Verbeek, "A compact phased array based multi-wavelength laser," in *Integrated Photonics Research (IPR '96)*, (Boston, Massachusetts), pp. 136–138, Apr. 29–May 2 1996.
- [116] A. A. M. Staring, L. H. Spiekman, J. J. M. Binsma, E. J. Jansen, T. van Dongen, P. J. A. Thijs, M. K. Smit, and B. H. Verbeek, "A compact 9 channel multi-wavelength laser," *IEEE Photon. Technol. Lett.*, 1996. To appear in the September issue.
- [117] M. Zirngibl, C. H. Joyner, C. R. Doerr, L. W. Stulz, and H. M. Presby, "A 18 channel multi frequency laser," in *Integrated Photonics Research (IPR '96)*, (Boston, Massachusetts), pp. 128–131, Apr. 29–May 2 1996.
- [118] C. R. Doerr, C. H. Joyner, M. Zirngibl, L. W. Stulz, and H. M. Presby, "Elimination of signal crosstalk from carrier density changes in the shared semiconductor amplifier of multifrequency signal sources," *IEEE Photon. Technol. Lett.*, vol. 7, pp. 1131–1133, Sept. 1995.

Summary

The growing demand for telecommunication increases the need for bandwidth in telecommunication networks. For the time being, the use of glass fibre has met this demand, but in order to use the enormous transmission capacity of the fibre efficiently in the future, the equipment used to launch and detect bit streams in the fibre, and to switch and route the signals, should be modernised as well. A large part of the network will be optical, to avoid many cumbersome conversions between the optical and the (slower) electrical domain.

Integrated optics offers interesting possibilities for the realization of this optical equipment. By using fabrication technology comparable to that of traditional electronic ICs, planar optical components can be made in the form of photonic integrated circuits (PICs). Provided that a reasonable scale of integration can be achieved, this offers many of the advantages of electronic ICs, i.e., reduced equipment size and reduced cost.

Prerequisite for increasing the scale of integration is the ability to produce very compact optical components. This is not as trivial as it is for electronic components, because often it is the dimensions of an optical component that determine its operation. This thesis describes a numerical and experimental investigation into the limits of miniaturisation of integrated optical components like couplers and wavelength demultiplexers. The emphasis is on the tolerance of these components for the unavoidable variations in the fabrication process.

Optical waveguides, being the basic elements of all optical circuitry, are discussed first. It is shown that ridge waveguide losses are not only caused by rough waveguide sidewalls, as is often assumed, but, and more importantly, by the rough etched surface *beside* the waveguide. Furthermore, deep-etched waveguides with low losses are demonstrated, that have been realized using a newly developed high quality fabrication process. The same deep-etching process enabled the fabrication of waveguide bends with a record sharp bending radius of only $30\mu\text{m}$.

Couplers that distribute and combine optical power are also very important components. We made ultra-small multi-mode interference couplers ($90\mu\text{m}$, less than half as long as previously published components). We also show, however, that the price to pay for this miniaturisation is strongly reduced tolerances in the fabrication.

Subsequently, a compact wavelength demultiplexer working according to the "phased array" principle is presented. The polarisation dependence of this component has been compensated for by using different array orders for the two polarisation directions. To avoid fabrication variations spoiling the performance of the component, wide, multi-mode exit waveguides have been used to improve tolerance.

The above-mentioned components have all been made in the indium phosphide semiconductor material system. This material has the advantage that lasers and detectors can be monolithically integrated. A disadvantage is the small waveguide dimensions, which complicate the coupling to optical fibres. We also realized a number of demultiplexers in polymer waveguides. The fibre-like geometry of these waveguides makes coupling very easy, but is disadvantageous for obtaining small device dimensions. Typical minimum bending radii are 30mm, as compared to $300\mu\text{m}$ in semiconductor waveguides. A study has been made into the reduction of these radii, resulting in a smallest demultiplexer of $19 \times 6\text{mm}^2$, as compared to a size of $52 \times 9\text{mm}^2$ that was obtained without this reduction.

Finally, this thesis describes two applications of the phased array wavelength multiplexer in some more complicated devices. A demultiplexer integrated with multi-mode interference couplers forms the core of a 2.4Gb/s optical switch, and a multiplexer monolithically integrated with optical amplifiers forms the most compact multi wavelength laser reported so far.

The results presented in this thesis warrant the assumption that fundamental limits of the scale of opto-electronic integration have not yet been reached, and can be pushed forward by technological improvements.

Samenvatting

Onze steeds groter wordende behoefte om op afstand te communiceren heeft geresulteerd in een sterke groei van de vraag naar bandbreedte in telecommunicatienetten. Dankzij het gebruik van glasvezel als transportmedium kan deze behoefte vooralsnog bevredigd worden. Maar om ook in de toekomst aan deze vraag te voldoen moet zo optimaal mogelijk gebruik gemaakt worden van de capaciteit van de vezel. Golfengtemultiplextechnieken en optisch schakelen kunnen hiervoor zorgen. Zoveel mogelijk functies van het net moeten optisch uitgevoerd worden, om omslachtig heen- en terugconverteren naar het (tragere) elektrische domein te voorkomen.

Voor de realisatie van deze nieuwe optische apparatuur biedt het vakgebied van de *geïntegreerde optica* aantrekkelijke perspectieven. Met technieken vergelijkbaar met die uit de traditionele IC-productie kunnen optische componenten gemaakt worden op een vlak substraat, in de vorm van optische geïntegreerde circuits (PICs, photonic integrated circuits). Mits een hoge integratieschaal gehaald kan worden bieden deze PICs vergelijkbare voordelen als de bekende elektronische ICs, namelijk reductie van de omvang van apparatuur, en een gereduceerde kostprijs.

Voor het vergroten van de integratieschaal is het essentieel dat zeer kleine optische componenten gemaakt kunnen worden. Dit is minder triviaal dan bij elektronische componenten, omdat het bij licht vaak juist de dimensies van de componenten zijn die bepalen hoe ze zich gedragen. Dit proefschrift beschrijft een onderzoek naar de grenzen van de miniaturisatie van geïntegreerd-optische componenten als koppelaars en golfengte-demultiplexers, waarbij de nadruk gelegd wordt op de tolerantie die deze componenten aan de dag leggen voor de onvermijdelijke variaties in het fabricageproces.

Omdat optische golfgeleiders de basisbouwstenen zijn voor optische circuits, worden deze als eerste behandeld. In het proefschrift wordt aangetoond dat de verliezen die in dijk golfgeleiders optreden niet alleen veroorzaakt worden door ruwe golfgeleiderwanden, zoals vaak aangenomen wordt, maar veeleer door het ruwe geëtste oppervlak *naast* de golfgeleider. Verder passeren diep geëtste golfgeleiders de revue die dankzij een nieuw ontwikkeld etsproces weinig verlies vertonen. Ditzelfde diepe-etsprocedé zorgt ervoor dat golfgeleiderbochten gemaakt konden worden met laag verlies en bochtstralen van slechts $30\mu\text{m}$, de scherpste golfgeleiderbochten tot nu toe.

Optische koppelaars, die vermogen distribueren of combineren, zijn ook zeer belangrijke componenten. We hebben uiterst compacte multimode-interferentiekoppelaars gemaakt (met slechts $90\mu\text{m}$ lengte meer dan de helft korter dan eerder gepubliceerde componenten), maar

laten tevens zien dat de prijs die voor deze verkleining betaald moet worden een sterk gereduceerde tolerantie voor fabricagevariaties is.

Vervolgens wordt een compacte golflengtedemultiplexer gepresenteerd die werkt volgens het "phased array" principe. De polarisatie-afhankelijkheid van deze component wordt gecompenseerd door verschillende array-orde te gebruiken voor de twee polarisatierichtingen. Om de invloed van fabricagevariaties te verminderen, worden brede, multimode uitgangsgolfgeluiders gebruikt.

Bovenstaande componenten zijn alle in het indiumfosfide halfgeleidermateriaalsysteem gemaakt. Dat heeft het voordeel dat lasers en detectoren monolithisch meegeïntegreerd kunnen worden. Andere materiaalsystemen hebben andere voordelen. Polymeer componenten zijn bijvoorbeeld zeer makkelijk aan een glasvezel te koppelen, omdat de golfgeluidersdoorsnede bijna identiek is aan die van de vezel. Daarom is ook een aantal golflengtedemultiplexers gemaakt in dit materiaal. Omdat de kleinste haalbare bochtstraal hierbij het grootste probleem is ($30\mu\text{m}$ wordt bij lange na niet gehaald; eerder moet gedacht worden aan 30mm), heb ik uitgebreide berekeningen gedaan aan de invloed van het brekingsindex-contrast van het materiaal op deze bochtstralen. De kleinste demultiplexer die hieruit voortvloeide mat nog altijd $19 \times 6\text{mm}^2$, maar dit is een stuk kleiner dan de $52 \times 9\text{mm}^2$ die verkregen wordt als men geen speciale aandacht aan de bochten schenkt.

Tot slot wordt nog een tweetal toepassingen van de phased array golflengtedemultiplexer gepresenteerd, waarbij deze component, geïntegreerd met multimode interferentiekoppelaars, het hart vormt van een optische schakelaar, en het, monolithisch geïntegreerd met optische versterkers, een negenkanaals multi-golflengte laser vormt.

Dankwoord

Het is een bekend feit dat de meeste mensen die een proefschrift in handen krijgen meteen doorbladeren naar het dankwoord. Gelijk hebben ze natuurlijk, want wetenschap bedrijven is een sociaal gebeuren, en daarom is behalve wat een promovendus inhoudelijk heeft gedaan ook zeer interessant met wie hij heeft samengewerkt. Het zou echter jammer zijn als u, lezer, het bij het lezen van dit dankwoord zou laten. Ik wil u de rest van dit proefschrift dan ook van harte aanbevelen.

Verreweg de meeste dank ben ik verschuldigd aan Bart Verbeek en Meint Smit. Bart, jij was als promotor de drijvende kracht achter dit werk; ik kon altijd bij je terecht voor opbouwend commentaar, en je zorgde er voor dat ik de grote lijnen niet uit het oog verloor. Meint, je hebt met je creativiteit en kritische instelling een belangrijke bijdrage geleverd aan dit werk. Ik heb veel van je geleerd, vooral op het gebied van het schrijven van artikelen met een hoge informatiedichtheid.

Siang Oei en Liang Shi hebben essentiële nieuwe procestechnieken ontwikkeld, zonder welke veel van de beschreven componenten niet gemaakt hadden kunnen worden. Aad de Vreede en Koos van Uffelen, jullie lithografie was niet te overtreffen; zelfs de meest stringente maatvoerings-eisen die ik specificeerde, werden door jullie gehaald. Frans van Ham en Ed Metaal, jullie etswerk heeft mooie devices opgeleverd. Vooral de diep-geëtste componenten in de hoofdstukken 3 en 4 getuigen van sterke staaltjes van etskunst. Fokke Groen, bedankt voor het maken van de maskers, die ik zo vol met structuren had gezet dat de computer zich er nog wel eens in verslikte; jij was hem toch steeds weer te slim af. Ook Charles de Boer, Ab Kuntze en Adrie Looyen hebben belangrijke bijdragen geleverd aan de fabricage van de devices. En we waren natuurlijk nergens geweest zonder de mooie epitaxiale lagen uit Gent, gegroeid door Piet Demeester en Ingrid Moerman.

Lucas Soldano, Martin Amersfoort en Cor van Dam hebben mij aan het begin alles geleerd dat ik moest weten over MMIs en Phased Arrays. Bovendien zijn zij als collega's allen ook nog bijzonder goed te pruimen. Dit geldt ook voor Xaveer Leijtens, die bovendien onze lokale UNIX en L^AT_EX guru is, zodat hij hoog scoort op de lijst van meest bezochte ganggenoten. Kees Steenbergen is van het begin af mijn kamergenoot geweest. We hebben vaak lange discussies gehad over de meest wilde ideeën voor componenten, die niet allemaal even realistisch waren, maar het was in ieder geval gezellig. Toen Kees Vreeburg er later bijkwam op de kamer, bleven de discussies en de gezelligheid, maar met twee Kezen werd het er niet eenvoudiger op.

Ik dank Toine Staring, Hans Binsma, Edwin Jansen en Peter Thijs van het Philips Optoe-

lectronics Centre voor de prettige samenwerking die leidde tot de hoofdstukken 7 en 8. Mart Diemeer en Danny Ramsamoedj van Akzo Nobel worden bedankt voor de samenwerking en hun inzet, die resulteerde in hoofdstuk 6. Jos van der Tol en Jørgen Pedersen van PTT Research dank ik voor de vruchtbare discussies, evenals Maurus Bachmann en Pierre-André Besse, die mij tevens in staat stelden de transmissie-meetopstelling van de ETH Zürich te gebruiken.

Ik heb een aantal studenten mogen begeleiden, die mij vaak aardig wat werk uit handen namen, en zorgden voor een frisse kijk op de dingen: Marco Kroonwijk, Henrik Yngvesson, Patrick Bouso, Dadi Song en Willem Bertels.

Bij Bart Zorn en Paul Snoeij kon ik altijd terecht als er weer wat mis was met de VAX. (Meestal kwam dat omdat ik er zelf niets van begreep.) Mia van der Voort en Wendy van Schagen dank ik voor de secretariële ondersteuning en de gezelligheid. Henk Scholten hartelijk bedankt voor het controleren van delen van de tekst op fouten in het gebruik van het Engels. Prof. dr G.J. Hooyman dank ik voor het beschikbaar stellen van de foto die de kافت van dit proefschrift siert.

Tot slot bedank ik al mijn vrienden die de afgelopen vier jaar voor de broodnodige ontspanning hebben gezorgd. Wetenschap mag dan een sociaal gebeuren zijn, er gaat toch niets boven een biertje. Mijn ouders dank ik voor het feit dat ze mij in staat hebben gesteld te leren en te studeren. Dat heeft niet alleen met geld te maken; opvoeding is een véél belangrijker factor. Hun stimuleren van mijn nieuwsgierigheid heeft me gemaakt tot wat ik nu ben. En Kirsten, die weet wel wat haar nabijheid de afgelopen jaren voor mij heeft betekend. Hààr bedanken doe ik wel als jullie niet kijken.

Leo

Curriculum Vitæ

Ik ben op 22 juni 1968 geboren in Utrecht. Na verhuizing naar Soest en het doorlopen van het Gymnasium te Amersfoort ben ik in 1986 naar Utrecht teruggekeerd om experimentele natuurkunde te studeren. Op 29 april 1992 ben ik afgestudeerd bij de vakgroep Atoom- en Grenslaagfysica, met een onderzoeksverslag getiteld "Kinetiek en structuur van de oxidatie van Fe(110) en het Pt/Fe(110) systeem". Het onderzoek betrof de initiële oxidatie van een ijzer-éénkristal en de oppervlaktestructuur van het gevormde oxidelaagje. Dit onderzoek heb ik uitgevoerd met een variëteit aan oppervlakte-gevoelige meettechnieken onder ultrahog-vacuum condities.

Op 1 mei 1992 ben ik in dienst getreden bij de vakgroep Telecommunicatie- en Tele-observatietechnologie van de faculteit Elektrotechniek in Delft, om het onderzoek te doen waarvan het resultaat nu voor u ligt. Sinds juli 1996 ben ik als postdoc werkzaam bij Bell Labs in Holmdel, NJ (USA), waar ik werk aan geïntegreerd-optische multi-golflengte lasers en golflengte-converters.

